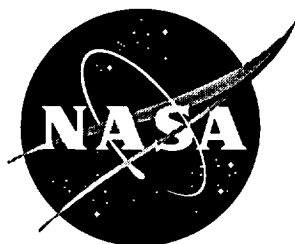


NASA Contractor Report 198202



# An Investigation of Cavity Vortex Generators in Supersonic Flow

Richard Hazlewood  
*Center for Research Inc., Flight Research Laboratory*  
*Department of Aerospace Engineering*  
*University of Kansas*  
*Lawrence, Kansas*

Cooperative Agreement NCC1-172

**February 1996**

National Aeronautics and  
Space Administration  
Langley Research Center  
Hampton, Virginia 23681-0001



## **ABSTRACT**

The purpose of this report is to document the results of experiments performed at the University of Kansas and at the NASA Langley Research Center into the use of shaped cavities to generate vortices in supersonic flow, as well as the progress made in simulating the observed flow using the PAB3D flow solver. The investigation was performed on eighteen different cavity configurations installed in a convergent-divergent nozzle at the Jet Exit Facility at NASA Langley. Pressure sensitive paint, static pressure ports, focusing Schlieren and water tunnel flow visualization techniques were used to study the nature of the flow created by these cavities. The results of these investigations revealed that a shaped cavity can generate a pair of counter-rotating streamwise vortices in supersonic flow by creating weak compression Mach waves and weak shocks. The ability of pressure sensitive paint to measure high pressure flows was also confirmed. The PAB3D computer program, developed at NASA Langley, was used to attempt to reproduce the experimental results. Unfortunately, due to problems with matching the grid blocks, no converged results were obtained. However, intermediate results as well as a complete definition of the grid matching problem and suggested courses of action are presented.

## **ACKNOWLEDGEMENTS**

I would like to thank my advisor, Dr. Saeed Farokhi for all of his help and guidance. Dr. Ray Taghavi also provided a lot of help, especially in the final stages of writing this report. Thanks also to the other members of my committee, Dr. Dave Downing and Dr. Eddie Lan.

The engineers at NASA Langley were critical to the completion of this report. Dan Cler, the lead engineer on the project, allowed me to observe some of the testing performed at NASA Langley, answered all of my questions and provided me with everything that I needed in the way of technical information and materials. Milton Lamb, the second engineer was also a great help. Dr. S. Paul Pao and John Carlson were of invaluable help in working with the PAB3D program, dedicating many hours to helping me try to solve the grid problems. Amir Jagharghi lead the team from the Aerodynamic Measurement Branch. There were many other engineers and technicians at NASA Langley who worked on this project; who designed, built, modified and performed all of the testing. Thank you all.

**TABLE OF CONTENTS**

ABSTRACT ..... i

ACKNOWLEDGEMENTS ..... ii

NOMENCLATURE ..... vi

LIST OF FIGURES ..... viii

LIST OF TABLES ..... xi

1.0 INTRODUCTION ..... 1

3.0 THEORETICAL CONSIDERATIONS ..... 2

    3.1 Development of Supersonic Vortices ..... 2

    3.2 Supersonic Vortex Generator Operation ..... 4

    3.3 Computational Fluid Dynamics ..... 5

        3.3.1 Grid Generation ..... 6

        3.3.2 Flow Solver ..... 6

4.0 EXPERIMENTAL FACILITIES AND PROCEDURES ..... 11

    4.1 University of Kansas Experiments ..... 11

        4.1.1 University of Kansas Supersonic Wind tunnel ..... 11

        4.1.2 Schlieren Investigation ..... 12

        4.1.3 Surface Flow Visualization ..... 13

    4.2 NASA Langley Experiments ..... 14

        4.2.1 Propulsion Simulation System ..... 14

        4.2.2 Test Nozzle Geometry ..... 15

        4.2.3 Instrumentation ..... 17

4.2.4	Data Acquisition . . . . .	18
4.2.5	Force Balance Calibration . . . . .	19
4.2.6	Pressure Sensitive Paint and Static Pressure . . . . .	19
4.2.7	Focusing Schlieren Flow Visualization . . . . .	24
4.2.8	Laser Light Sheet Flow Visualization . . . . .	25
4.2.9	Water Tunnel Flow Visualization . . . . .	26
5.0	RESULTS AND DISCUSSION . . . . .	50
5.1	University of Kansas Flow Visualization . . . . .	50
5.1.1	Schlieren Flow Visualization . . . . .	50
5.1.2	Surface Flow Visualization . . . . .	50
5.2	NASA Langley Flow Visualization and Static Pressure Tests . . . . .	52
5.2.1	Thrust and Performance Determination . . . . .	53
5.2.2	Pressure Sensitive Paint and Static Pressure Tap Measurements . . . . .	54
5.2.3	PSP Error Analysis . . . . .	56
5.2.4	Focusing Schlieren Flow Visualization . . . . .	58
5.2.5	Laser Light Sheet Flow Visualization . . . . .	59
5.2.6	Water Tunnel Flow Visualization . . . . .	60
5.3	Computational Fluid Dynamics Results . . . . .	61
5.3.1	Flat Plate Modelling . . . . .	61
5.3.2	Expanding Flow Modelling . . . . .	62
5.3.3	Grid Resolution Problems . . . . .	62
6.0	CONCLUSIONS AND RECOMMENDATIONS . . . . .	85
6.1	Conclusions . . . . .	85
6.2	Recommendations . . . . .	86
7.0	REFERENCES . . . . .	88
APPENDIX A	University of Kansas Flow Visualization Pictures . . . . .	A1

<b>APPENDIX B</b>	<b>NASA Langley Experimental Results .....</b>	<b>B1</b>
<b>APPENDIX C.</b>	<b>Sample input files for AXB .....</b>	<b>C1</b>
<b>APPENDIX D.</b>	<b>Sample control files for PAB3D.V12 .....</b>	<b>D1</b>

## NOMENCLATURE

<u>Symbol</u>	<u>Meaning</u>	<u>Units</u>
b	Cavity Base Length	in.
d	Cavity Depth	in.
$F/F_i$	Net Thrust Ratio	-
$F_r/F_i$	Net Thrust Ratio	-
h	Cavity Height	in.
h	Enthalpy	J/kg
I	Luminescence	-
$K_q$	Sturm-Volmer Constant	-
M	Mach Number	-
NPR	Nozzle Pressure Ratio, $p_{tj}/p_a$	-
p	Local Static Pressure	psi, Pa
P	Pressure	psi, Pa
$p_a$	Atmospheric Pressure	psi, Pa
$P_{O_2}$	Partial Pressure of Oxygen	psi, Pa
$p_{tj}$	Jet Total Pressure	psi, Pa
s	Entropy	J/kg
t	Time	sec
T	Temperature	K, °F
V	Velocity	fps, mps
$w_p/w_i$	Weight Flow Ratio	-
<u>Greek Symbols</u>	<u>Meaning</u>	<u>Units</u>
$\gamma$	Ratio of Specific Heats	-
$\delta$	Cavity Ramp Angle	Degrees
$\epsilon$	Error	-
$\theta$	Cavity Vertex Half-Angle	Degrees

$\lambda$	Scalar Multiplier	-
$\mu$	Total Viscosity	lbm/ft-s
$\rho$	Density	lbm/ft <sup>3</sup>
$\sigma$	Standard Deviation	psi
$\Omega$	Vorticity	

### Subscripts

o	Without Quenching
t	Total
th	Throat

### Meaning

### Acronyms

AIAA	American Institute of Aeronautics and Astronautics
AR	Aspect Ratio
CCD	Charged Coupling Device
CD	Convergent-Divergent
CFD	Computational Fluid Dynamics
ESP	Electronically Scanning Pressure
HP	High Pressure
KU	University of Kansas
LaRC	Langley Research Center
LP	Low Pressure
MCV	Multiple Critical Venturi
MDRL	McDonnell-Douglas Research Laboratory
NASA	National Aeronautics and Space Administration
PSP	Pressure Sensitive Paint
SSVG	Smart Supersonic Vortex Generator
VG	Vortex Generator

## **LIST OF FIGURES**

<b><u>Figure Title</u></b>	<b><u>Page</u></b>
2.1.1      Supersonic Vortex Generator Operation .....	8
3.3.1      Generated Grid for Investigation of Divergent Supersonic Flow with Cavity Installed. Configuration 6 .....	9
3.3.2      Three Dimensional Grid for Investigation of Cavity Flow in a Divergent Supersonic Nozzle. Configuration 6 .....	10
4.1.1      The University of Kansas Supersonic Wind Tunnel .....	27
4.1.2      Schematic of the Supersonic Wind tunnel at the University of Kansas .....	27
4.1.3      Supersonic Vortex Generator Tested at KU .....	28
4.1.4      Schlieren Flow Visualization System Used at the University of Kansas .....	29
4.1.5      Schematic of the Configurations Tested at the University of Kansas Supersonic Wind Tunnel .....	30
4.2.1      Photograph of Dual Flow Propulsion Simulation System .....	31
4.2.2      Dual Flow Propulsion Simulation System Schematic .....	32
4.2.3      Test Nozzle Channel Contour .....	33
4.2.4      Active Control Nozzle with Installed Divergent Flap and Cavity .....	34
4.2.5      The Active Control Nozzle and the Eighteen Divergent Flap Configurations ..	35
4.2.6      Photograph of Configuration 6 .....	36
4.2.7      Photograph of Configuration 11 .....	37
4.2.8      Photograph of Configuration 21 .....	38
4.2.9      Photograph of Configuration 22 .....	39
4.2.10     Schematic of Flap Geometry with ESP Port Locations .....	40
4.2.11     Photograph of Installed Pressure Instrumentation and PSP Data Acquisition Equipment on the Active Control Nozzle .....	41
4.2.12     Molecular Photoluminescence Transition Processes .....	42
4.2.13     Molecular Energy Transition to the Ground State .....	42
4.2.14     Sturm-Volmer Relationship for Air .....	43

4.2.15	General PSP Instrumentation System . . . . .	43
4.2.16	MDRL Paint Process . . . . .	44
4.2.17	Optical Description of the Focusing Schlieren System . . . . .	45
4.2.18	Layout of the Focusing Schlieren System . . . . .	46
4.2.19	Photograph of the Focusing Schlieren System . . . . .	47
4.2.20	Isometric View of the Langley 16- by 24- inch Water Tunnel . . . . .	48
4.2.21	Flow Diagram for the Langley 16- by 24- inch Water Tunnel . . . . .	49
5.1.1	Schlieren Photograph of Configuration A, No Flow . . . . .	64
5.1.2	Schlieren Photograph of Configuration A, Mach=2.0 . . . . .	64
5.1.3	Surface Flow Pattern with Dye Injected for Surface Flow Visualization, Configuration B, Indented Walls . . . . .	65
5.1.4	Surface Flow Pattern with Dye Injected for Surface Flow Visualization, Configuration C, Straight Walls . . . . .	65
5.1.5	Surface Flow Pattern with Dye Injected for Surface Flow Visualization, Configuration D, Shallow Ramp . . . . .	66
5.1.6	Surface Flow Pattern with Dye Injected for Surface Flow Visualization, Configuration E, Straight Vertex . . . . .	66
5.2.1	Performance Data for Configuration 6 . . . . .	67
5.2.2	Performance Data for Configuration 11 . . . . .	67
5.2.3	Performance Data for Configuration 21 . . . . .	68
5.2.4	Performance Data for Configuration 22 . . . . .	68
5.2.5	ESP Pressure Contour for NPR=2.0, Configuration 6 . . . . .	69
5.2.6	PSP Pressure Contour for NPR=2.0, Configuration 6 . . . . .	69
5.2.7	ESP Pressure Contour for NPR=8.8, Configuration 6 . . . . .	70
5.2.8	PSP Pressure Contour for NPR=8.8, Configuration 6 . . . . .	70
5.2.9	ESP Pressure Contour for NPR=8.8, Configuration 13 . . . . .	71
5.2.10	PSP Pressure Contour for NPR=8.8, Configuration 13 . . . . .	71
5.2.11	PSP Pressure Contour for Various NPRs and Configurations . . . . .	72
5.2.12	Focusing Schlieren of Configuration 1 Installed on Lower Ramp, NPR=2.0 . .	73
5.2.13	Focusing Schlieren of Configuration 6 Installed on Lower Ramp, NPR=2.0 . .	73

5.2.14	Focusing Schlieren of Configuration 6 Installed on Lower Ramp, NPR=8.8 . .	74
5.2.15	Focusing Schlieren of Configuration 6 Installed on Both the Upper and Lower Surfaces, NPR=8.8 . . . . .	74
5.2.16	Focusing Schlieren of Configuration 22 Installed on Lower Surface, NPR=8.8	75
5.2.17	Laser Light Sheet Picture Showing the Development of Streamwise Vortices for Configuration 6, NPR=8.8 . . . . .	76
5.2.18	Laser Light Sheet Picture Showing the Interaction of Four Vortices for Configuration 13, NPR=8.8 . . . . .	76
5.2.19	Water Tunnel Dye Injection Showing the Development of Vortices for Configuration 5 . . . . .	77
5.2.20	Laser Light Sheet Visualization of Vortices Developed in Water Tunnel, Configuration 5 . . . . .	78
5.2.21	Laser Light Sheet Picture of the Streamwise Development of Vortex for Configuration 5 in the Water Tunnel . . . . .	78
5.2.22	Laser Light Sheet of Streamwise Development of the Shear Layer Produced by Installing the Cavity Backwards in Water Tunnel Flow . . . . .	79
5.2.23	Laser Light Sheet of Crossflow Development of the Shear Layer Produced by Installing the Cavity Backwards in Water Tunnel Flow . . . . .	79
5.3.1	Static Pressure Within the Cavity, Flat Plate Flow Conditions, Mach 2.0, Configuration 1 . . . . .	80
5.3.2	Static Pressure Within the Cavity, Flat Plate Conditions, Mach 2.0, Configuration 6 . . . . .	81
5.3.3	Oblique View of Nozzle Grid with Matching Problems Highlighted . . . . .	82
5.3.4	Top View of Nozzle Grid with Matching Problems Highlighted, Configuration 6 . . . . .	83
5.3.5	Schematic of Suggested Grid/Block Definitions for Nozzle Flow Solver . . . .	84

## **LIST OF TABLES**

<b><u>Table</u></b>	<b><u>Title</u></b>	<b><u>Page</u></b>
4.1.1	Geometry of Vortex Generators Investigated at the University of Kansas . . . . .	12
4.2.1	Configuration Geometry for a Supersonic Vortex Generator Studied at NASA Langley. . . . .	16
4.2.2	Configuration Specifications for Multi-Cavity Configurations of a Supersonic Vortex Generator Tested at NASA Langley . . . . .	17
5.2.1.	Summary of PSP Analysis Results for Configuration 6 of the C-D Nozzle . . . . .	57



## **1.0 INTRODUCTION**

The purpose of this report is to document the results of flow control studies in the supersonic regime. A shaped cavity (ref. 1) was used to generate a pair of counter-rotating streamwise vortices in supersonic flow.

Vortex generation traces its roots back to the start of aircraft development. These subsonic vortex generators were primarily of two types, vane-type and ramp-type vortex generators such as those developed by Wheeler (ref. 2). In both cases, the devices were protrusions into the flow. These protrusions caused turning of the flow over the device and streamwise vortices were generated.

Due to the presence of waves in supersonic flow, i.e. compression Mach waves and expansion Mach waves, and related shock formation, such protrusions would be "lossy." Therefore, cavities turning flow with weak supersonic waves (expansion and compression) have been investigated. Five different cavity configurations were studied at the University of Kansas and eighteen single and multiple cavity configurations were investigated at NASA Langley. The PAB3D computer code developed by engineers of the Propulsion Aerodynamics Branch of NASA Langley was used to attempt to augment the experimental results.

There are many potential applications for a supersonic vortex generator:

- Transonic drag reduction
- Control of flow separation on propulsion system installations such as boattails
- Base drag reduction
- Flow attachment in divergent supersonic ramps in convergent-divergent nozzles and thrust vectoring applications
- Flow turning enhancement in turbomachinery blading in transonic and supersonic throughflow compressors and turbines
- Supersonic jet noise reduction through enhanced mixing in the free shear layer
- Shock cell restructuring in underexpanded nozzles
- Supersonic shock noise reduction
- Mixing enhancement in backward-facing-step SCRAMjet combustors
- Flow control in supersonic inlets

### **3.0 THEORETICAL CONSIDERATIONS**

The development of streamwise vortices in supersonic flow will be discussed as well as the theoretical operation of the supersonic vortex generator developed at the University of Kansas.

#### **3.1 Development of Supersonic Vortices**

The understanding of the generation of streamwise vortices in supersonic flow is derived from the differential form of inviscid linear momentum, Euler's equation without body forces,

$$\rho \frac{D\mathbf{v}}{Dt} = -\nabla P \quad (1)$$

Writing out the substantial derivative, Eqn (1) is

$$\rho \frac{\partial \mathbf{v}}{\partial t} + \rho (\mathbf{v} \cdot \nabla) \mathbf{v} = -\nabla P \quad (2)$$

Now, the combined first and second law of thermodynamics in three-dimensional space form is needed,

$$T \nabla_s = \nabla h - \frac{\nabla P}{\rho} \quad (3)$$

Combining Eqns (2) and (3) results in:

$$T \nabla_s = \nabla h + \frac{\partial \mathbf{v}}{\partial t} + (\mathbf{v} \cdot \nabla) \mathbf{v} \quad (4)$$

However, from the definition of total enthalpy,

$$h = h_o - \frac{V^2}{2}$$

Hence,

Substituting Eqn (5) into (4):

$$\nabla h = \nabla h_o - \nabla \left( \frac{V^2}{2} \right) \quad (5)$$

$$T \nabla s = \nabla h_o - \nabla \left( \frac{V^2}{2} \right) + \frac{\partial \mathbf{v}}{\partial t} + (\mathbf{v} \cdot \nabla) \mathbf{v} \quad (6)$$

Using the vector identity

$$\nabla \left( \frac{V^2}{2} \right) - (\mathbf{v} \cdot \nabla) \mathbf{v} = \mathbf{v} \times (\nabla \times \mathbf{v})$$

Eqn. (6) becomes

$$T \nabla s = \nabla h_o - \mathbf{v} \times (\nabla \times \mathbf{v}) + \frac{\partial \mathbf{v}}{\partial t} \quad (7)$$

Equation (7) is known as *Crocco's theorem*, because it was first obtained by L. Crocco in 1937 (ref. 3).

For steady, adiabatic flow, Crocco's theorem becomes

$$T \nabla s = -\mathbf{v} \times (\nabla \times \mathbf{v}) \quad (8)$$

Equation (8) is the basis for developing streamwise vortices in supersonic flow. If the assumption is made that the waves involved in the creation of these vortices are weak waves, in other words Mach waves, then the flow can be reasonably assumed to be isentropic. For this condition, equation (8) becomes

$$\mathbf{v} \times (\nabla \times \mathbf{v}) = 0 \quad (9)$$

Equation (9) has two solutions. The most common interpretation of this equation is that the flow is *irrotational* or

$$\nabla \times \mathbf{v} = 0$$

However, another solution is also physically valid. If the vorticity vector is *parallel* to the flow direction, then

$$\mathbf{v} \times \boldsymbol{\Omega} = 0 \quad (10)$$

Therefore, the solution for the vorticity vector becomes

$$\boldsymbol{\Omega} = \lambda * \mathbf{v} \quad (11)$$

In other words, the resulting vorticity vector is aligned with the velocity vector. The result this development is that through weak supersonic waves, streamwise flow rotation may be generated in the limit of inviscid flow. However, the effects of viscosity cannot be neglected in the development of these vortices.

### **3.2 Supersonic Vortex Generator Operation**

To accomplish this task of generating vortices in supersonic flow isentropically, the idea of using a wedge shaped cavity with a ramp was developed, see figure 2.1.1.

The supersonic freestream flow encounters the vertex of the shaped cavity. Since the edge of the cavity is not perpendicular to the flow, the resulting expansion fan is "smeared" along the lip of the cavity. As the flow encounters the ramp, the flow turns into itself, creating compression waves. Since the expansion is smeared, so will be the compression. As a result, the compression waves do not coalesce into a shock wave as quickly. The relative strength of the shock wave that does coalesce will depend greatly on the depth of the cavity. Essentially, there is a small region within the cavity where the compression waves are relatively weak. These expansion and compression waves coalesce into a pair of counter-rotating, streamwise vortices. As the vortices travel up the ramp, more and more flow is encountered, creating stronger vortical structures. When the flow finally emerges from the ramp at the base of the cavity, the vortices are fully developed and travelling parallel to the upstream flow. The vortices have a higher flow

energy than the boundary layer on the plate. As a result, the vortices can energize the boundary layer, delaying separation. Also, since the vortices have a lower static pressure than the surrounding flow, shocks in an overexpanded nozzle should be delayed longer. The presence of the vortices should allow the supersonic flow to expand farther down the divergent portion of the duct, as a result, the shock-induced separation downstream of the cavity will be delayed. This would result in a stronger shock. However, there are cases where delaying the separation would be desirable even with the increased losses due to the stronger shock.

The angle that the cavity walls made with the freestream flow was considered important. It was believed, and later confirmed experimentally, that stronger vortices would be formed if the vertex half-angle was less than the freestream Mach angle. If the vertex half-angle was less than the Mach angle, then the normal component of the flow to the lip would be subsonic. Conversely, if the vertex half-angle was greater than the Mach angle, then the lip would be exposed to supersonic normal flow and would essentially act like a backward facing step in supersonic flow, creating very weak vortices.

The shaped cavity investigated here was originally designed to act in an active manner. The SSVG would be deployable as necessary to aid in controlling flow separation in offdesign conditions or in thrust vectoring situations.

### **3.3 Computational Fluid Dynamics**

The experiments used to investigate the cavity vortex generator were primarily qualitative in nature. As a result, a computational fluid dynamics analysis was attempted to obtain quantitative data about the cavity vortex flow. It was believed that if the CFD code could adequately predict the observed flow phenomena, that the code could later be used for design of an "optimum" shape for the cavity in any desired flow field.

### 3.3.1 Grid Generation

The grid used to model the SSVG was generated using the AXB program, developed by Dr. S. Paul Pao at NASA Langley (ref. 4). This grid generator was designed for generating multi-patch, multi-block grids for 2-D and simple 3-D objects and flow. Since the cavity under investigation was a simple 3-D design, this code was originally considered ideal for grid generation. AXB has the additional advantage of automatically generating a standard output file used by the CFD flow solver used. Reference 4 gives a more detailed description of the AXB grid generation package. Appendix C contains a sample set of input files used by the AXB code to generate the grid for the nozzle design.

For the cavity flow investigation, four grid blocks were created. One upstream of the cavity, one inside the cavity, one for flow over the cavity and one for downstream flow. Boundary layer grid concentrations were made along the bottom surface, along the cavity walls and downstream along the expected vortex paths. The final grid contained 670,516 grid points. Figure 3.3.1 shows a sample grid, viewed from above, for the nozzle configuration investigated. Figure 3.3.2 shows the same grid in 3-D. Grids for the nozzle shape as well as a flat plate grid were generated. No orthogonality of the grid was assumed during the solution procedure.

### 3.3.2 Flow Solver

The CFD code used for this investigation was the PAB3D code, version 12, developed at the Propulsion Aerodynamics Branch at NASA Langley. This code is a multi-grid, multi-block code that has the capability to simulate chemical as well as aerodynamic flow characteristics. PAB3D has been extensively used by the engineers at NASA Langley to model and investigate a wide variety of flow conditions and phenomena (ref. 5-7). The PAB3D code has the advantage of allowing the user to custom design the solution method for a particular application.

A sample control file used with the PAB3D code is contained in Appendix D. The solution method chosen for this particular investigation is outlined below.

A thin-layer Navier-Stokes, with  $j$  and  $k$  directions uncoupled, formula was solved using a modified Roe solution scheme which used space marching. Ideal gas was assumed and no kinetic

energy dissipation was evaluated. A Roe flux splitting scheme was employed with a van Leer scheme used for the jacobean flux splitting. A third order spacial discretization with a third order minmod limiter was also used. A Jones-Lauder two equation turbulence model, where  $C_3 = \text{const} = 1.45$ , was used. No kinetic energy dissipation was evaluated. A constant time step was employed with a varying CFL number. Chuech's compressibility correction factor was used for the mixing length. Johnson-King and  $k-\epsilon$  models were used for the boundary layer turbulence models with a fully 3-D vorticity calculation. A Reimann invariant, constant pressure, was used for the far field boundary.

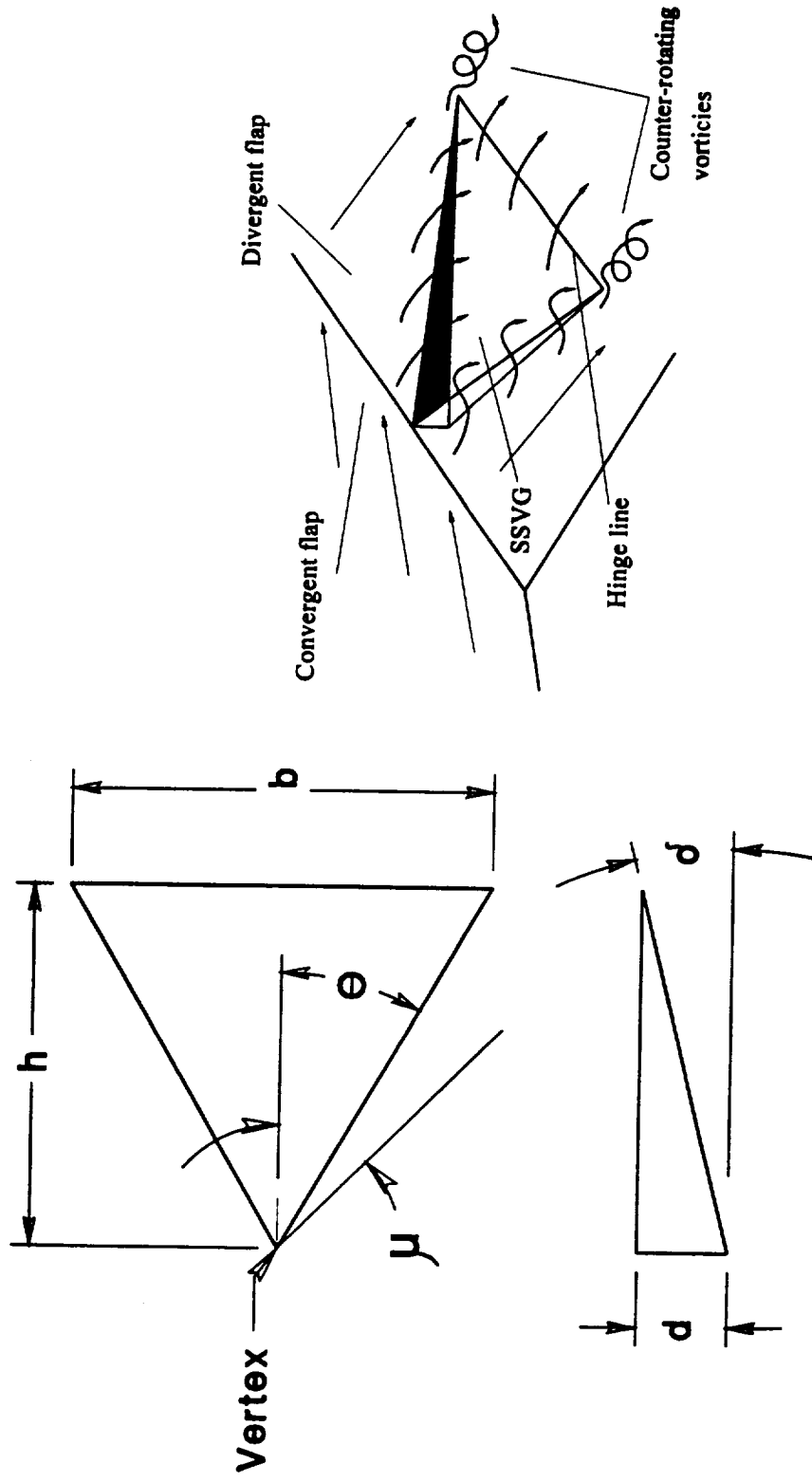


Figure 3.2.1 Supersonic Vortex Generator Operation

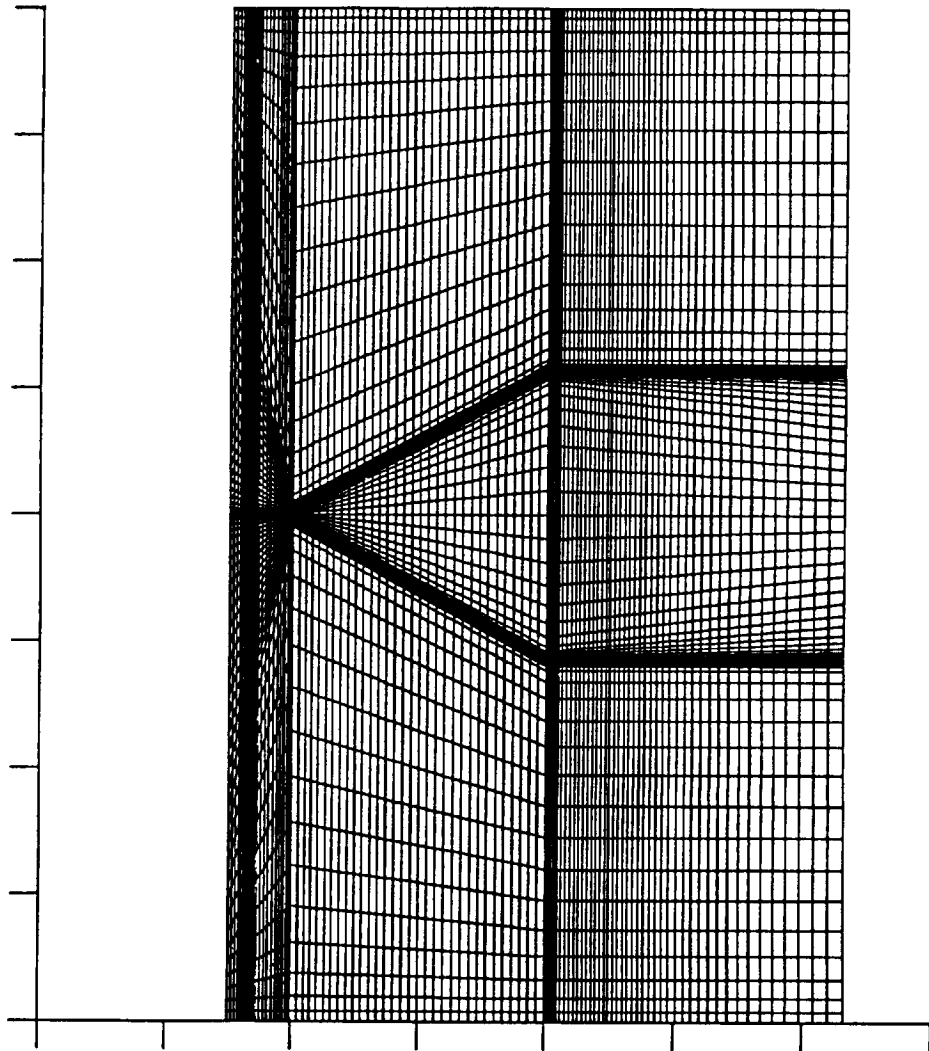


Figure 3.3.1 Generated Grid for Investigation of Divergent Supersonic Flow with Cavity Installed. Configuration 6 ( $\theta=30^\circ$ ,  $\delta=8^\circ$ )

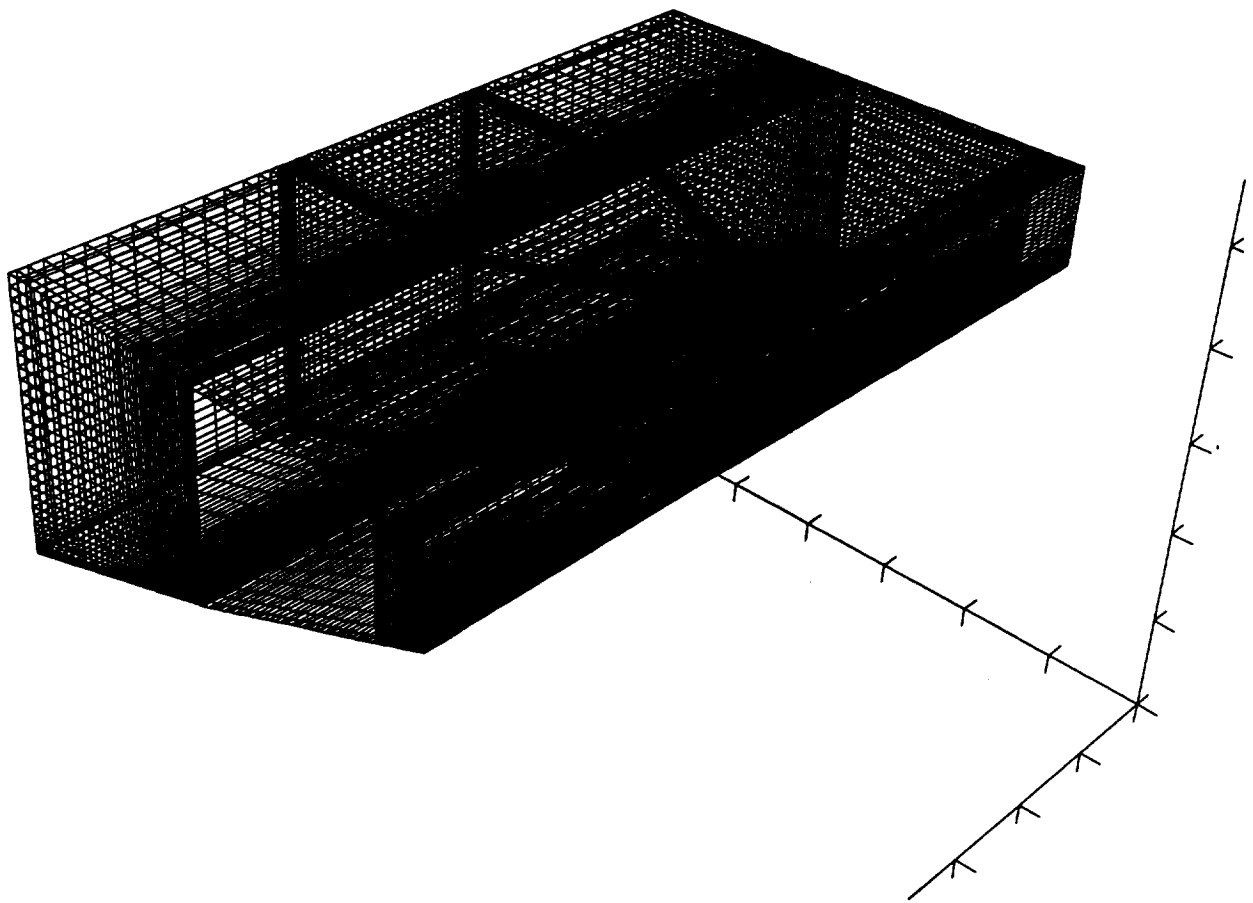


Figure 3.3.2 Three Dimensional Grid for Investigation of Cavity Flow in a Divergent Supersonic Nozzle. Configuration 6 ( $\theta=30^\circ$ ,  $\delta= 8^\circ$ )

## **4.0 EXPERIMENTAL FACILITIES AND PROCEDURES**

This section presents an overview of the various experimental facilities used to investigate the SSVG. The initial proof-of-concept investigation was performed at the University of Kansas supersonic wind tunnel. Additional experiments were performed at the NASA Langley Jet Exit Facility and at the Langley 16 by 24 inch Water Tunnel.

### **4.1 University of Kansas Experiments**

The initial investigation of the SSVG was performed at the University of Kansas using the supersonic wind tunnel. Two separate experiments were conducted: Schlieren flow visualization and surface flow investigations.

#### **4.1.1 University of Kansas Supersonic Wind tunnel**

The experimental investigation of the supersonic vortex generator began with Schlieren photographs taken in the 3 1/2" x 2" supersonic wind tunnel at the University of Kansas. These experiments were conducted as a first step in the investigation of the potential benefits of the SSVG. Figure 4.1.1 shows a photograph of the supersonic wind tunnel at the University of Kansas with a flow visualization cavity model installed.

The supersonic wind tunnel at the University of Kansas is a suction-type, open flow wind tunnel, see Figure 4.1.2. The test section sidewalls are made of optically pure glass to allow for Schlieren system operation. During the experiments performed at KU, the throat area of the tunnel was adjusted to provide a test section Mach number of 2.0, based on isentropic flow assumptions. The mass flow rate of the wind tunnel was calculated to be 0.020 slugs/sec [ 0.29 kg/sec] assuming isentropic flow of air as a calorically perfect gas. The Reynold's number for these experiments was approximately 1.5 million based on the height of the cavity.

#### 4.1.2 Schlieren Investigation

A wedge shaped model was made with the cavity engraved on the upper surface. Figure 4.1.3 shows the front and back of one of the VGs used for flow visualization. Table 4.1.1 gives the geometry of the SSVGs used for this first investigation.

Table 4.1.1 Geometry of Vortex Generators Investigated at the University of Kansas

Configuration	Vertex Half Angle (deg)	Ramp Angle (deg)	Special Feature
A	20	15	Schlieren Model
B	20	15	Sloped Walls
C	20	15	Straight Walls
D	20	8	Shallow Ramp
E	20	15	Flat Vertex

The initial proof-of-concept investigation was performed using the Schlieren system associated with the wind tunnel, see Figure 4.1.4. This system uses 5 inch mirrors to focus the light through the test section onto a knife edge and then into a focusing and alignment tube. A film screen was attached to the end of the tube and photographs of density gradient visualizations were taken of the test section using a Minolta Maxxum 7000, 35 mm camera with a 28-85 macro-zoom lens.

The model constructed for the Schlieren system investigation, designated configuration A, was used to verify the existence of streamwise vortices and to determine the influence of the cavity on the vortex development. Since the inflow was set at Mach 2.0, with an associated Mach wave angle of 30 degrees, this configuration allowed for the investigation of the effects of a subsonic cavity lip upon the vortex development.

### 4.1.3 Surface Flow Visualization

A relatively new flow visualization technique was used at the University of Kansas to investigate the surface flow patterns in and around the cavity. Using a variation of the technique described in reference 8, the technique at KU employed colored water released through small holes in the surface and observing the resulting streak-lines. The use of several different colors of water allows the mixing characteristics of the surface flow field to be observed.

This technique was attempted at KU using standard food coloring mixed with tap water. The water was fed to the model through tygon tubing to static pressure ports 1/16 th of an inch in diameter drilled into the model, shown in figure 4.1.2. Six ports were drilled into the model. Three holes were drilled upstream of the cavity in order to observe the flow through the VG and three holes were drilled in the ramp area of the VG to observe the development of stagnation regions. Three different colors of dye were used, red, yellow and blue. These colors allowed for easy observation of the mixing of the flow in various parts of the cavity. Figure 4.1.3 shows an installed VG in the wind tunnel for this investigation, including a view of the back of the model with the tygon tubing attached to the drilled holes.

Several aspects of the VG design were investigated using the surface flow patterns. Specifically, the effects of sidewall shape, vertex shape, and ramp angle were investigated. The sidewalls were initially inclined relative to the ramp by an angle of 15 degrees. Wind tunnel putty was used to vary the angle between 15 degrees and 0 degrees. The ramp angle was also varied using wind tunnel putty. The VG was built with a ramp angle of 15 degrees; using the putty, the angle was changed to approximately 8 degrees. Finally, the vertex shape was changed using the wind tunnel putty, changing the relatively sharp vertex to a flat vertex. All of the variations of the original design are shown graphically in Figure 4.1.5.

Although the accuracy of these experiments left much to be desired, it was believed that the gross effects of varying the above parameters could be investigated. The results of these investigations were then used to help tailor the design configurations constructed at NASA Langley.

## **4.2 NASA Langley Experiments**

The majority of the experimental investigation was performed at the Jet Exit Facility of the NASA Langley Research Center 16 Foot Transonic Tunnel Complex. Models were mounted on a dual flow propulsion simulation system in an acoustically treated ambient test chamber. A control room adjacent to the test area offers access through a sound-proof door.

The Jet Exit Facility has a stand alone data acquisition system but shares its air supply with the 16 Foot Tunnel propulsion simulation system. This system uses a series of reservoirs, valves, filters, and heat exchangers to provide clean, dry, stable airflow at a constant total temperature of 530°R for mass flow rates up to 15 lbm/sec. Opposite the jet flow is a 5'x5' exhaust duct through which test chamber airflow is vented to the atmosphere with noise suppression. Reference 9 provides further details of the test facility.

### **4.2.1 Propulsion Simulation System**

The test rig used for these investigations was originally designed for testing performed by Craig Hunter (ref. 10). To reduce costs, inserts were made with the VG installed that could fit into the nozzle designed by Mr. Hunter, as a result, most of the information concerning the actual test rig is taken directly from the above reference. Figure 4.2.1 shows the dual flow test rig used in this study, and Figure 4.2.2 diagrams the internal details of the dual flow propulsion simulation system. This system supplies high pressure air to a test nozzle such that forces and moments produced by the nozzle can be easily measured accurately. Choke points and backpressured plenums simulate a large air supply reservoir.

As shown in figure 4.2.2, air passes through two primary air supply lines into an annular high pressure plenum. From the HP plenum, air flows radially through a set of radially spaced sonic nozzles into a low pressure plenum. This radial flow delivery scheme minimizes the effects of fluid momentum forces on the balance, and the sonic nozzles provide a local choke point in the propulsion simulation system. The effects of fluid pressure forces on the force balance are minimized by S tubes that isolate and seal the metric and nonmetric portions of the propulsion simulation model.

Once in the LP plenum, air flows through a circular to rectangular transition section, through a choke plate for flow conditioning, and into an instrumentation duct. The choke plate used in this test provides 62% area blockage to backpressure and stabilize plenum airflow and simulate turbulent engine flow conditions going into the instrumentation duct and test nozzle. The instrumentation duct contains corner and center mounted total pressure rakes, comprising a total of seven pitot probes, and two iron-constantan thermocouples for total temperature measurement. Air passes through the instrumentation section and into the test nozzle where it exhausts to atmosphere.

#### 4.2.2 Test Nozzle Geometry

The nozzle used in this test is a sub-scale, non-axisymmetric, two-dimensional convergent-divergent (2D CD) nozzle with an expansion ratio of  $A_e/A_{th} = 1.797$ , a nominal throat area of  $A_{th} = 4.317 \text{ in}^2$  [ 0.110  $\text{m}^2$ ], and a width of 3.990 in.[0.1013 m]. Details of the nozzle channel contour are defined in Figure 4.2.3. The convergent region of the nozzle is composed of a 2.000 in. [0.0508 m] radius circular arc and tangent 27.29 degree ramp which blends into a smooth 0.625 in. [0.0159 m] radius throat. A relatively steep 11 degree divergence ramp encourages boundary layer separation at off-design conditions.

The test nozzle was designed with interchangeable divergent flaps such that the effects of divergent surface modification on shock-boundary layer interaction and off-design performance could be determined. Furthermore, the nozzle is equipped with full length, optical quality glass sidewalls for focusing Schlieren and laser vapor sheet flow visualization. The photograph in Figure 4.2.4 shows the nozzle installed on the propulsion simulation system with configuration 1 installed.

In addition to a baseline configuration, nine single VG divergent flap configurations and eight multiple VG divergent flap configurations were tested. Table 4.2.1 details the physical geometry of each cavity tested at NASA Langley, Table 4.2.2 gives greater details of the multi-cavity configurations. The various configurations are shown in Figure 4.2.5 with the pressure instrumented flap and an uninstrumented flap for each case.

Photographs of some of the VGs tested are given in Figures 4.2.6 through 4.2.9. Note that different flap configurations could be used on the test nozzle; for example, a single 60 degree vertex VG and two 90 degree VGs. Such combinations could be used to investigate asymmetric flow effects for thrust vectoring. However, all testing performed in the present study was conducted with matching flap pairs, except for some Schlieren results that show a comparison of the baseline flaps and vortex generator flaps inserted in opposite divergent surfaces.

Table 4.2.1 Configuration Geometry for a Supersonic Vortex Generator Studied at NASA Langley.

Configuration Number	Number of Cavities	Height (in)	Base (in)	Aspect Ratio <sup>(1)</sup>	Depth (in)	Area Ratio <sup>(2)</sup>
1	1	1.000	0.536	0.536	0.070	0.0328
2	1	1.000	0.536	0.536	0.141	0.0328
3	1	1.000	0.728	0.728	0.070	0.0446
4	1	1.000	0.728	0.728	0.141	0.0446
5	1	1.000	1.155	1.155	0.070	0.0707
6	1	1.000	1.155	1.155	0.141	0.0707
7	1	1.000	2.000	2.000	0.070	0.1224
8	1	1.000	2.000	2.000	0.141	0.1224
9	1	1.000	0.632	0.632	0.141	0.0707
10-15	2	0.500	0.364	0.728	0.070	0.0223
21	16	0.200	0.146	0.728	0.028	0.0286
22	31	0.200	0.146	0.728	0.028	0.0554
(1) Aspect Ratio is defined as the length of the base divided by the height of the cavity (b/h) See figure 3.2.1						
(2) Area Ratio is defined as the total planform area of all cavities divided by the area of the plate						

Table 4.2.2 Configuration Specifications for Multi-Cavity Configurations of a Supersonic Vortex Generator Tested at NASA Langley

Configuration Number	Relative Cavity Spacing	Desired Effect
10	Side-by-Side; Touching	Complementary Vortex Production
11	Side-by-Side; 1 Element Separation	Independent Vortex Production
12	Like Edges Touching	Vortex Interaction at Formation
13	Like Edges Aligned 1/2 Element Downstream	Vortex Interaction after Formation
14	Unlike Edges; Inline	Vortex Interaction at Formation
15	Unlike Edges, 1/2 Element Downstream	Vortex Interaction after Formation

#### 4.2.3 Instrumentation

Nozzle air flow rates were calculated based on pressure and temperature measurements in a calibrated multiple critical venturi (MCV) system located upstream of the propulsion simulation model. The MCV system is rated to be 99.9% accurate in weight flow measurements. Forces and moments generated by the nozzle were measured by a six-component strain-gauge balance mounted on the propulsion simulation model centerline.

In order to acquire detailed data concerning the off-design flow characteristics of the 2D CD nozzles, the test nozzle is equipped with high resolution pressure instrumentation. Six convergent

section static pressure orifices and a static pressure orifice at the throat, all located on the upper flap, were common to all configurations tested. Figure 4.2.10 shows the locations of the pressure ports and the geometry of the nozzle flap. All pressure orifices on the test nozzle (convergent and divergent flaps) were 0.020 in. [50.8  $\mu\text{m}$ ] in diameter.

Details of divergent flap pressure instrumentation are shown in Figures 4.2.12. The baseline configuration was equipped with a row of centerline and sideline (0.400 in. [1.02 cm] from the sidewall) pressure orifice, again on the upper flap.

Individual pressure transducers were used for measuring pressures in the air supply system, multiple critical venturi, instrumentation duct, and nozzle convergent section. Transducers were selected and sized to allow the highest accuracy over each required measurement range. Convergent and divergent flap pressures were measured by two electronically scanning pressure (ESP) modules, located next to the propulsion simulation system in the Jet Exit Facility. Each ESP module contained 32 individual pressure transducers capable of being recorded simultaneously.

#### 4.2.4 Data Acquisition

Voltage readings from the test nozzle, propulsion simulation model, and air supply system instrumentation were recorded simultaneously. Steady-state data were acquired by averaging 50 frames of instantaneous data taken at a sampling rate of ten frames per second. Calibration constants were applied to the steady-state voltage readings and corresponding forces, moments, pressures, and temperatures were calculated.

Jet total pressure was measured from four corner rake pitot tubes and the three center rake pitot tubes in the instrumentation section. The average total pressure was computed as the arithmetic mean of the seven measurements. Jet total temperature was computed in a similar fashion from two total temperature probes.

A detailed description of the data acquisition system and associated software can be found in References 9 and 11. At the design NPR of 8.8, the Reynold's number was approximately 1.9 million at the vertex of the cavity based on the cavity height.

#### 4.2.5 Force Balance Calibration

The force balance was calibrated under jet-on and jet-off conditions using standard weight elements. Balance loadings were made in each of the three force components (axial, normal, side) and about each of the three moment axes (yaw, pitch, roll). Calibrations were conducted and system tares calculated such that 95% of force data was correctable to within 0.5% of the balance full-scale load limits. See References 11 and 12 for additional information.

Jet-off calibrations were performed to correct for the effects of installing the balance in the propulsion simulation system. These calibrations determined the force-moment interactions existing between the flow transfer system (S tubes) and the balance. Similarly, jet-on calibrations were used to correct for interactions due to flow momentum transfer and S tube pressurization. Stratford choke nozzles with documented performance were used for jet-on calibrations. The ideal thrust and weight flow data was calculated assuming inviscid flow, see ref. 11 for details.

#### 4.2.6 Pressure Sensitive Paint and Static Pressure

The basic principles of pressure sensitive paint (PSP) were developed in the 1980s (ref. 13). Additional research has recently made this technique very practical (refs. 14-16). The governing theory behind pressure sensitive paint is based on molecular photoluminescence. Luminescence, which includes both fluorescence and phosphorescence, is a process which occurs when a molecule emits electromagnetic radiation after being excited from some ground state by an absorption of electromagnetic radiation.

Fluorescence occurs in a molecular transition of electrons from an excited singlet state to a ground singlet state. A molecule in a singlet state has equal numbers of electrons of opposing spins; i.e. it is in a state of zero electron spin. In contrast, phosphorescence occurs in a transition of electrons from a triplet excited state to a singlet ground state. A molecule in the triplet state has two unbalanced electrons of the same spin and hence has a non-zero state of spin.

In both fluorescence and phosphorescence, a molecule starts from the ground level in a singlet state and rises to the excited singlet state. An additional transition process may occur in which the molecule enters the triplet state. The final excited state is largely random; however, more

energy is required for a molecule to make the transition through the singlet state into the triplet state, and hence, this process occurs less frequently. Because of this additional energy expenditure, molecules in the excited triplet state have slightly less energy than the excited singlet state and are more resistant to transition to a lower energy singlet state. Figure 4.2.12 illustrates several details of the luminescence process, showing the transition to both the singlet and triplet excited states.

Fluorescence, the result of transition from the singlet excited state to the ground state, is a relatively short process, with a duration of approximately  $10^{-9}$  to  $10^{-7}$  seconds. Phosphorescence, on the other hand, is a longer process, taking from  $10^{-3}$  to 100 seconds (ref. 15). An important point to note is that the wavelength of light energy emitted in luminescence is longer than the wavelength of the excitation light, thus, the excitation light will not interfere with the measurement of the luminescence intensity.

Figure 4.2.13 shows a diagram of molecular energy transition to the ground state. In addition to emission in the form of fluorescence or phosphorescence, transition to the ground state can take place through a molecular collision. In particular, collision with an oxygen molecule will transfer energy from the excited molecule to the oxygen molecule. The end result is that the excited molecule will no longer emit electromagnetic radiation, and luminescence does not occur. This process is known as dynamic quenching (ref. 15).

On a larger scale, quenching reduces the overall luminescence of a given molecular composition. The number of excited molecules that quench, and conversely the number that luminesce, is a function of the number of oxygen molecules available for collision. In essence, quenching becomes a function of the density of oxygen molecules in a given region. The greater the density of oxygen molecules in the region, the more likely it is that quenching will occur, and therefore luminescence will be reduced.

The Sturm-Volmer relationship can be used to describe luminescence of a molecular composition being quenched. In the case where quenching is done by oxygen, where  $I$  is the luminescence,  $I_0$  is the luminescence with no quenching,  $K_q$  is the Sturm-Volmer constant, and  $P_{O_2}$  is the partial pressure of oxygen (ref 15);

$$I_0/I = 1 + K_q P_{O_2} \quad (12)$$

It is important to note that both the Sturm-Volmer constant and the unquenched luminescence are functions of temperature.

Equation 12 was used to study the relationship between luminescence intensity, partial pressure, and the Sturm-Volmer constant. Figure 4.2.14 presents luminescence intensity as a function of static pressure for several values of  $K_q$ . Calculations were made for dry air with 20.95% oxygen content.

Fig. 4.2.14 also shows that different values of  $K_q$  result in drastically different ranges of pressure in which luminescence can be effectively measured. For example, for  $K_q=0.1$ , the pressure range corresponding to roughly 90% of the luminescence scale is from 0 to 90 psia [0 - 621 kPa]. At  $K_q=1.0$ , that same percentage represents a pressure range of about 0 to 40 psia [0 - 276 kPa].

Besides illustrating various pressure and luminescence ranges, fig. 4.2.14 shows that important considerations must be made to use oxygen quenching of photoluminescence for any type of quantitative measurement. As  $K_q$  increases, the amount of change in luminescence intensity for a given pressure change also increases, meaning that higher values of  $K_q$  result in lower values of luminescence intensity at high pressures, inferring that signal to noise ratios will be greater in these cases (ref. 15). The overall conclusion is that compromises will have to be made to achieve the widest possible pressure range with available measurement technology.

Techniques based on photoluminescence with oxygen quenching have been in development for many years. Early applications were devoted almost entirely to flow visualization; no attempts were made at quantitative measurement (ref. 13). Current efforts involving quenched photoluminescence center around the use of a paint which contains a pressure sensitive fluorescent dye. The PSP can be applied to a surface and illuminated with the appropriate light to give virtually infinite spatial resolution in the measurement of pressure gradients across the surface. In fact, the sole limiting factor in measurement resolution lies in the optical/video system used to view and record data. The instrumentation system associated with the PSP technique is shown in Figure 4.2.15.

McDonnell Douglas Research Laboratories, a leading developer of PSP technology in the United States, has released a certain amount of information on their progress. Most of the

information that follows was discussed at an open meeting at NASA Langley Research Center. Other information is known to exist, but is of a proprietary nature.

MDRL's paint process consists of multiple airbrushed layers, each with a specific function, as shown in Figure 4.2.16. The first layer applied to a model is a coat of common white paint, used to maximize the luminescent intensity recorded by the measurement system. The second layer is a clear adhesive, used to securely bond the next layer, which contains the actual pressure sensitive paint, to the model. MDRL's pressure sensitive paint formulation consists of a transparent, oxygen permeable, chemical binder containing the luminescent "probe" molecules. The particular paint mixture used for these experiments was based on a University of Washington formula which was composed of 100 ppm platinum octaethylporphyrin dissolved in GP197, a proprietary mixture of polydimethylsiloxane in 1,1,1-trichloroethane.

The PSP used in this test is excited by ultra-violet light, and fluoresces in a wavelength corresponding to red. Because of excitation and fluorescence in the visible spectrum, ambient light must be minimized. The recording system used filtered out the ultra-violet excitation light, so the only light the system picked up was the red luminescent light and its reflection off of the white base layer. So, at a pressure corresponding to 100% quenching, and hence no luminescence, no image would be detected by the recording system. With zero quenching, or full scale luminescence, the surface in view would appear red to the recording system. Intermediate levels of quenching/luminescence can be measured in terms of the relative red level intensity emanating from the test surface.

The Sturm-Volmer model has unquenched luminescence ( $I_0$ ) as a parameter. Since measurement of  $I_0$  in a non-oxygen environment would be nearly impossible, light images are recorded under static and wind-on conditions. The resulting images are aligned and the intensities computationally ratioed to determine relative surface luminescence intensities, thus eliminating the need for  $I_0$ . Because of the temperature sensitivity of the Sturm-Volmer model, temperature was monitored using an infra-red camera. Little temperature variation occurred across the nozzle plate so no temperature calibration was made. In addition, pressure taps were used at selected locations for in situ calibration of the PSP measurement system.

The results of this experiment were obtained using a 14 bit digital camera with 512x512 pixel resolution. The images were mapped to a 256 level greyscale, and analyzed for luminescence

intensity. Combined with static pressure values obtained using the ESP modules, the luminescence intensity was used to determine the surface pressures.

There are several problems with the PSP technique that limit its effectiveness. Early versions of the paint caused increased model skin friction, resulting in errors in force and moment balance measurements. Subsequent efforts have produced a paint formulation and application process that produces surface finishes and thicknesses comparable to those on existing wind tunnel models.

The current paint formulation is quenched only by oxygen; as such test media is restricted to gas mixtures that contain oxygen and will not interfere with the quenching process. In addition, the paint is temperature sensitive, so the accuracy of pressure measurement is dependent on the accuracy of temperature measurement. Efforts are being devoted to develop paint formulations that could quench in different gasses and that are temperature independent. An obvious solution to the temperature problem would be to develop a paint that has measurable sensitivity to both temperature and pressure.

Current paint formulations have an upper pressure limit where fluorescence intensity decreases to a level that is below the measurement capability of the video system. That upper limit is about 46 psia [317 kPa] in air for current paint formulations and available video technology. That is based on the partial pressure of the oxygen in the air, so a gas mixture with a lower oxygen content would allow higher pressure measurements. As a result of this limitation, static pressure taps were installed on all models used to verify the PSP results.

In addition to pressure range limitations, there are limitations in the free stream Mach number range at which PSP will function. For a given wind tunnel model, low freestream Mach numbers result in small pressure changes, and hence small changes in fluorescent intensity; however, since all the experiments conducted for the VG were performed in the transonic and supersonic flow regimes, this problem was not a concern.

The durability of PSP is comparable to that of conventional model paints (ref. 13), but the PSP application process is much more critical. In addition to the complexity of the multi-layered paint coat, the thickness of the PSP layer must be strictly controlled; abnormal variations in PSP thickness can cause considerable variations in luminescence intensity and may directly affect the flow. Also, the PSP layer is vulnerable to oil, either in the form of droplets in the airflow, or from handling. Certain oils will interfere with the luminescence measurements, or even

luminesce on their own. The conclusion is that PSP models must be handled and tested carefully to avoid any sort of damage or contamination of the paint surface.

A final problem lies in data reduction, where model movement during a tunnel run can cause a misalignment between static and wind-on images. Uniform movement of the model through changes in position or rigid vibration can be compensated for, but any type of model deformation would require complex methods of alignment.

The paint's response time was on the order of 0.1 to 0.2 seconds. This is not quick enough to measure any type of turbulent phenomena, but would allow measurement of many of the pressure fluctuations present in aerodynamic testing. PSP measurements have been shown to be relatively accurate, details of the error analysis are discussed in reference 17.

A PC-based computer program has been developed for the processing of PSP data obtained from these experiments. The program uses a polynomial warping technique to perform geometric transformations on the wind-on images. An in-situ calibration technique was implemented to compute the PSP calibration coefficients. These coefficients were then used to ratio the wind off to the wind on images to obtain the surface pressure maps.

#### 4.2.7 Focusing Schlieren Flow Visualization

Due to the nature of this study, graphic information on shock-boundary layer interactions and vortex propagation was essential. Performance requirements and space limitations dictated the need for a compact flow visualization system that would provide high quality results. In addition, the harsh environment of a nozzle test stand necessitated a system that would be resistant to misalignment due to vibration and aeroacoustic loading. Recently, several low cost, large field focusing Schlieren systems have been demonstrated in various facilities at NASA Langley Research Center with a high degree of success (ref. 18). Such a system was a clear choice for this investigation.

Figure 4.2.17 shows the optical specifications of the focusing Schlieren system used in this test, and the layout of the optical system is shown in Figure 4.2.18. A photograph of the installed system is shown in Figure 4.2.19. The system was designed and built based on criterion developed by Weinstein (ref. 18). This particular system has a 133mm diameter field of view,

a sensitivity of 17 arcsec, a resolution of 0.25mm, a depth of sharp focus of 4.6mm, and a depth of unsharp focus of 36mm. Simply stated, this means that the system deflects light by 17 arcsec for a 10% change in brightness, it can resolve flow features down to 0.25mm, it can sharply focus on flow features within a 4.6mm "slice" of flow, and it effectively blurs 2mm flow features outside an analogous 36mm slice. Overall, the system is well configured for the present study.

The light source for the focusing Schlieren system is a xenon strobe flash tube. A driving circuit picks up synchronous pulses generated by the recording video camera and triggers the flash at a 30 Hz rate with pulses of 0.6 microsec. duration and 0.05 watt-sec. power. Along with a high resolution CCD camera, a 70mm Hasselblad still camera recorded the results.

The focusing Schlieren system was assembled on a 44 in. x 66 in. [1.12m x 1.68m] platform which was in turn mounted to rails attached to the dual flow test stand. The relative compactness of the system did not interfere with model changes.

Source and cut-off grids were oriented vertically such that the system was sensitive to streamwise density gradients. The laminar to turbulent transition of the shear layer is clearly visible along with the wave structure of the jet. The design of the optical system did not compensate for glass sidewalls of the actual test nozzle, since doing so would have decreased the capability of the system to focus on flows similar to those investigated here. In the configuration used, the focusing Schlieren system offered a good compromise of flow quality looking through the glass sidewalls and visualizing free jet flows where no glass sidewalls were present.

#### 4.2.8 Laser Light Sheet Flow Visualization

The vortex structure of the VG was also investigated using laser light sheets. Water mixed with a yellow Fluoracene dye mixture was injected through the upstream pressure ports. Laser light sheets were traversed through the flow field and allowed visualization of the 3-D vortex structure. For each of the configurations, ten standard positions were illuminated; additionally, each configuration's flow field was traversed to show the entire structure from the throat of the nozzle out past the end of the nozzle with the results recorded on standard videotape. The investigation of the vortices outside the nozzle allowed for an investigation of the interaction of the vortices with the ambient air.

#### 4.2.9 Water Tunnel Flow Visualization

Water tunnel flow visualization of the VG was performed at the 16 by 24 inch [0.41 by 0.61 m] water tunnel at NASA Langley. This facility is a closed return water tunnel capable of test section velocities from 0 - 0.75 ft/s [1.9 cm/s] with flow through the 16 in. by 24 in. [0.41 x .61 m] test section in the downward (vertical) direction. The velocity for this experiment was 0.25 ft/s [0.63 cm/s], where the most uniform flow occurs and it was slow enough to easily observe the vortex flow with the unaided eye, although, several tests were run at 0.67 fps [1.7 cm/s]. Details of the water tunnel facility are given in reference 19. Figure 4.2.20 shows the water tunnel and related components. Figure 4.2.21 shows the flow diagram for this system.

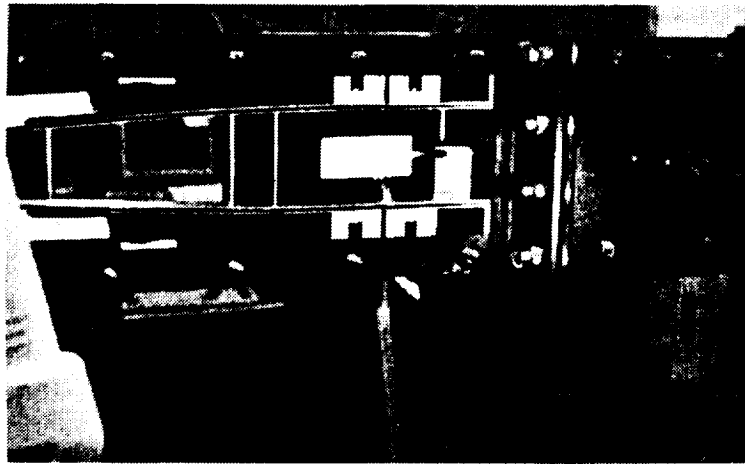


Figure 4.1.1 The University of Kansas Supersonic Wind Tunnel

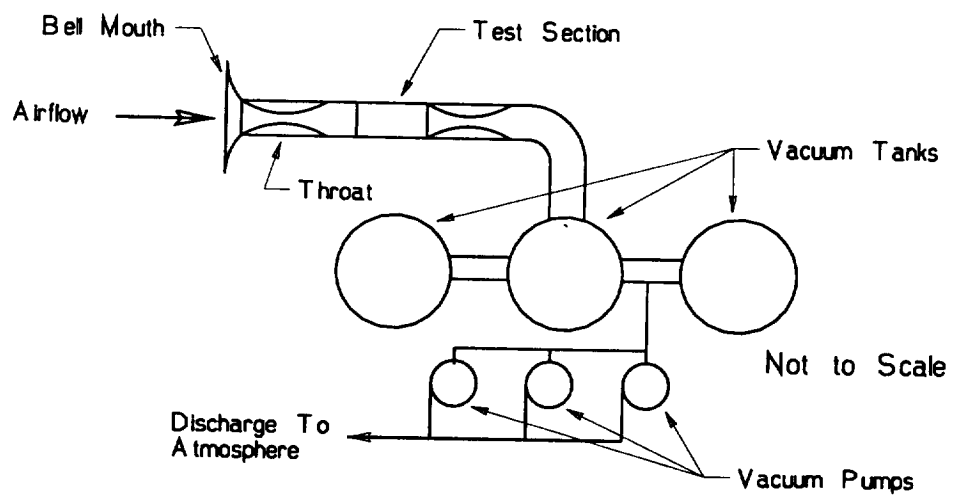


Figure 4.1.2 Schematic of the Supersonic Wind tunnel at the University of Kansas

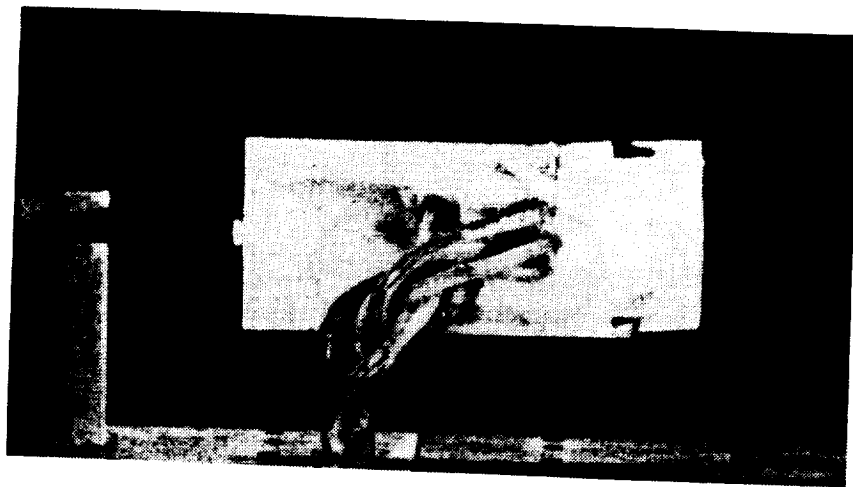
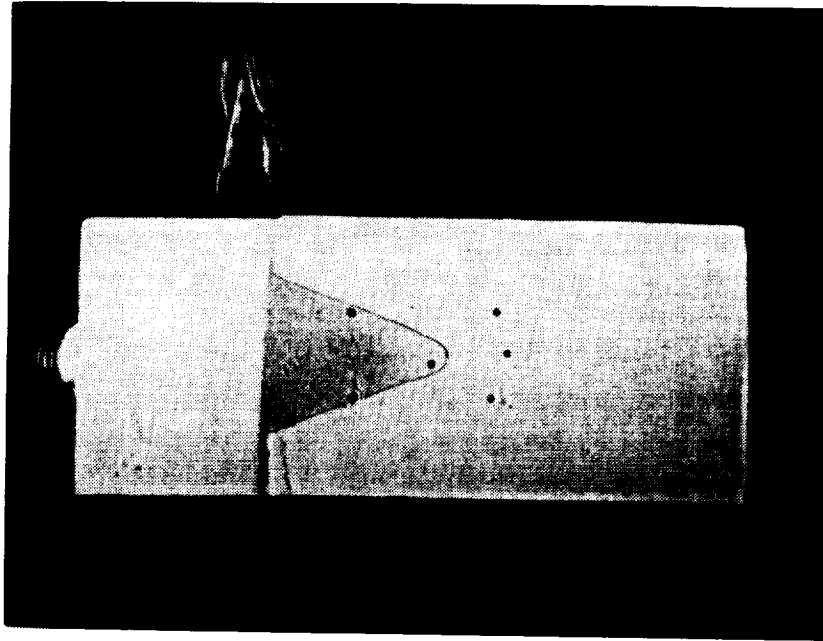


Figure 4.1.3 Supersonic Vortex Generator Tested at KU (Top: Front view, Bottom: Back view)

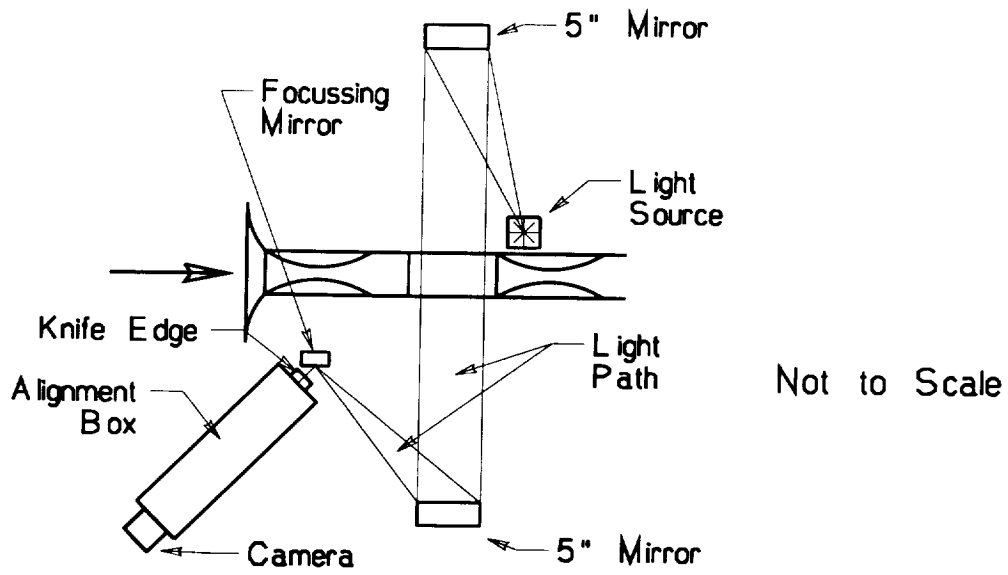


Figure 4.1.4 Schlieren Flow Visualization System Used at the University of Kansas

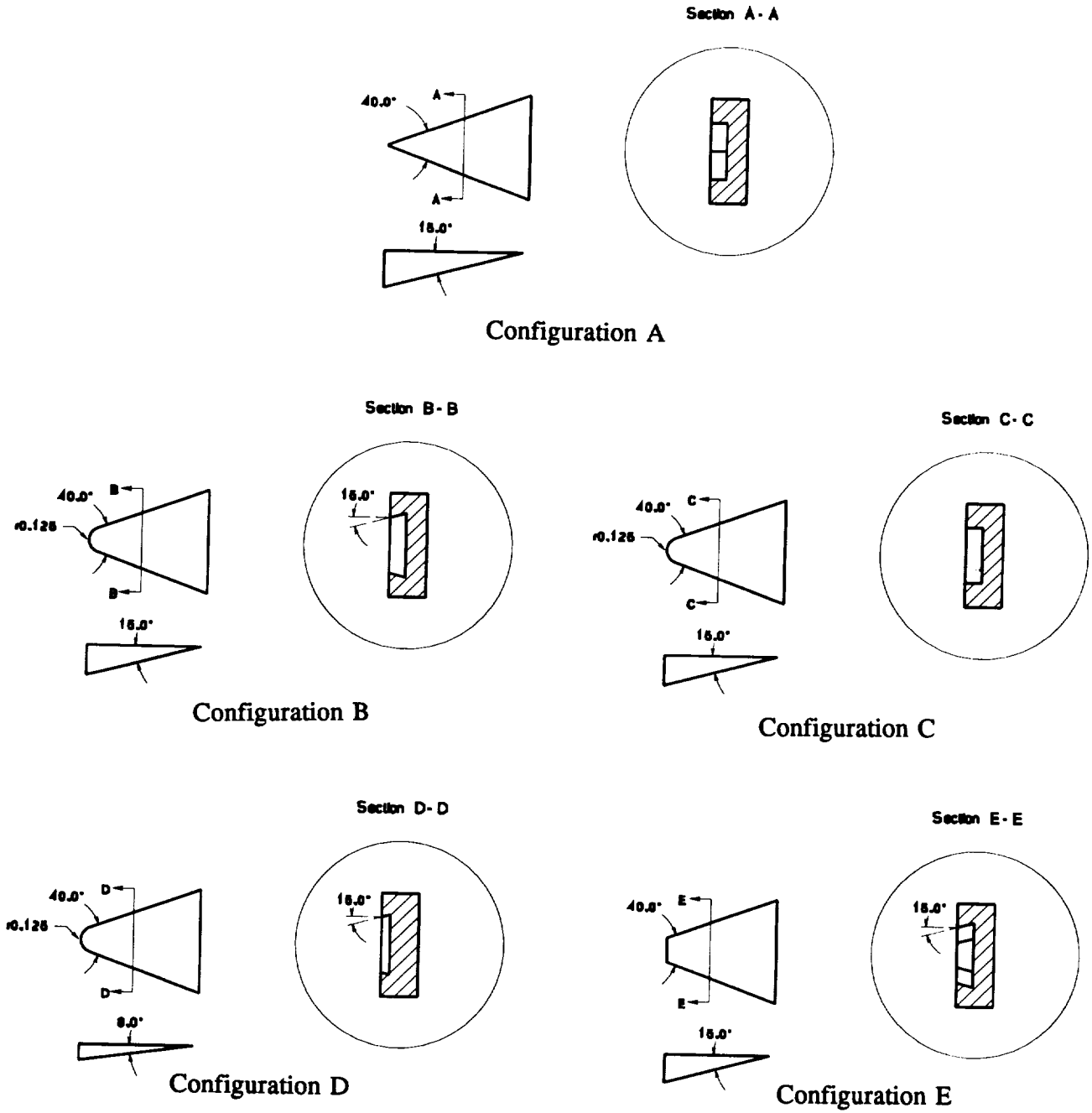


Figure 4.1.5 Schematic of the Configurations Tested at the University of Kansas  
Supersonic Windtunnel

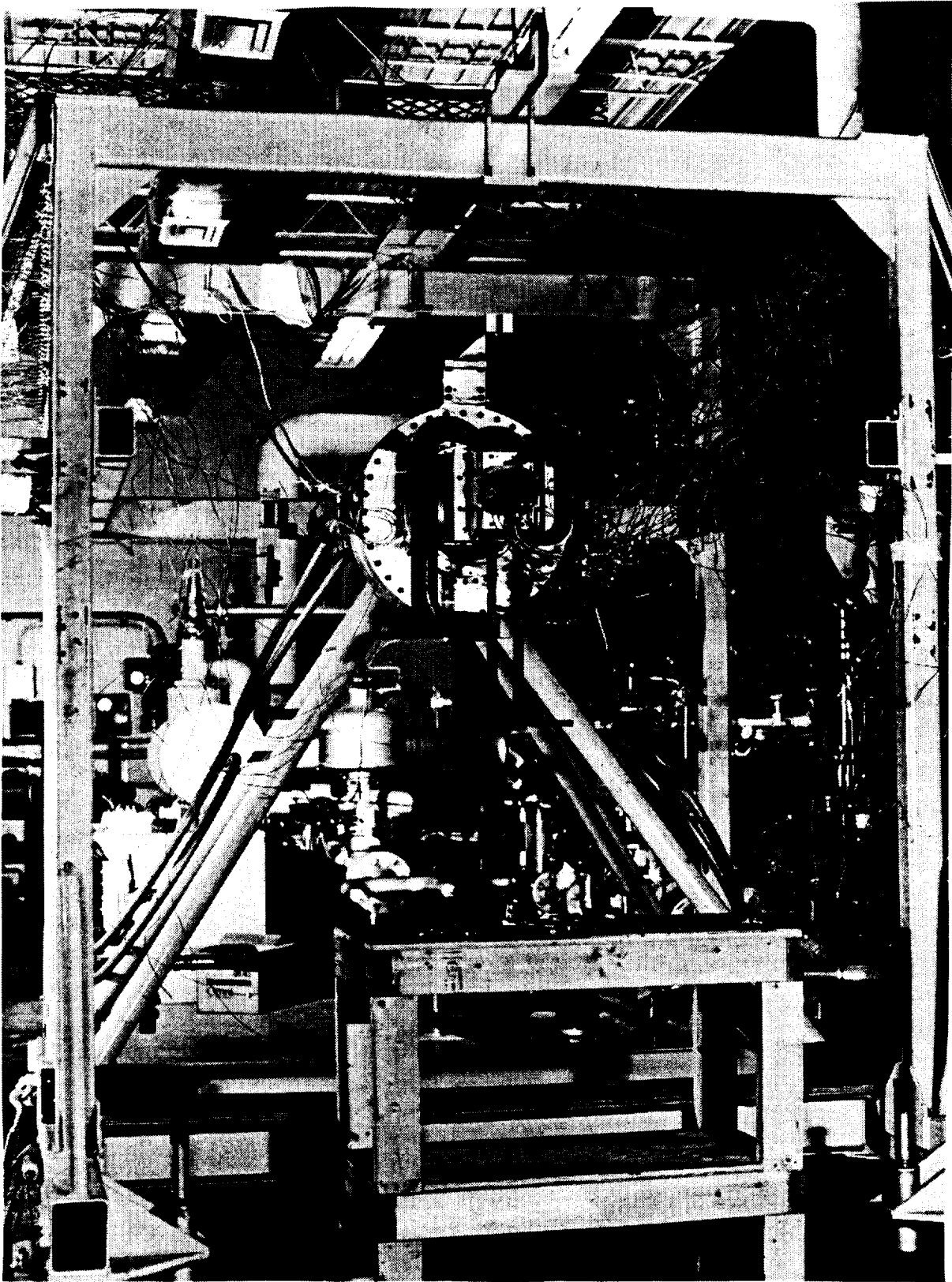


Figure 4.2.1 Photograph of Dual Flow Propulsion Simulation System  
(Langley Photo L93-11623).

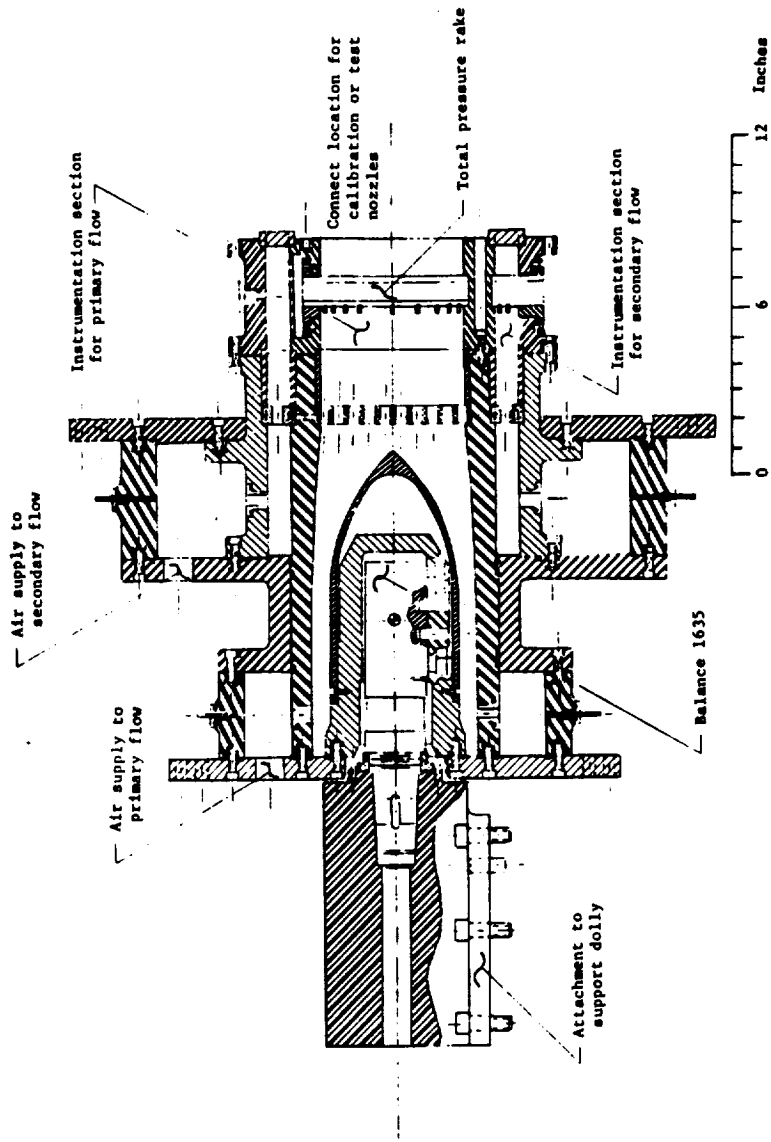


Figure 4.2.2 Dual Flow Propulsion Simulation System Schematic (from ref. 9)

POINT	COORDINATES (IN.)	
	X	Y
A	0.000	0.000
B	0.000	-0.614
C	0.000	1.386
D	0.917	1.163
E	1.988	0.611
F	2.394	0.553
G	2.430	0.559
H	2.275	1.166
I	4.550	0.972

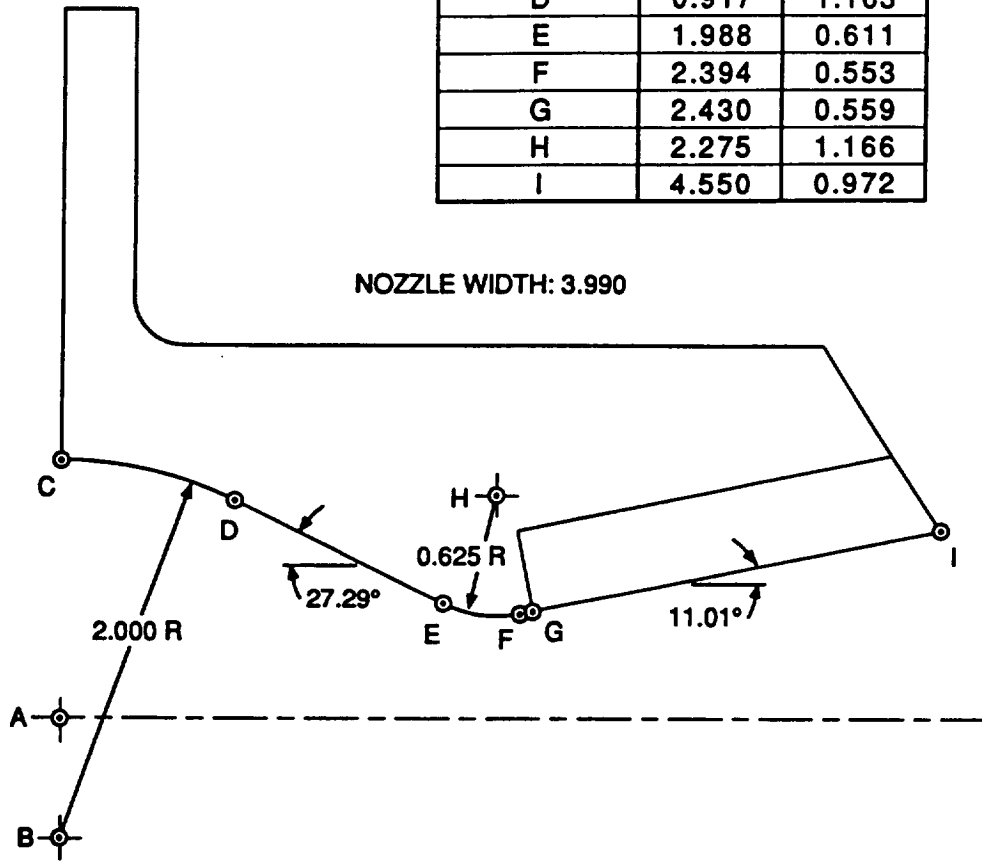


Figure 4.2.3 Test Nozzle Channel Contour (from ref. 10)

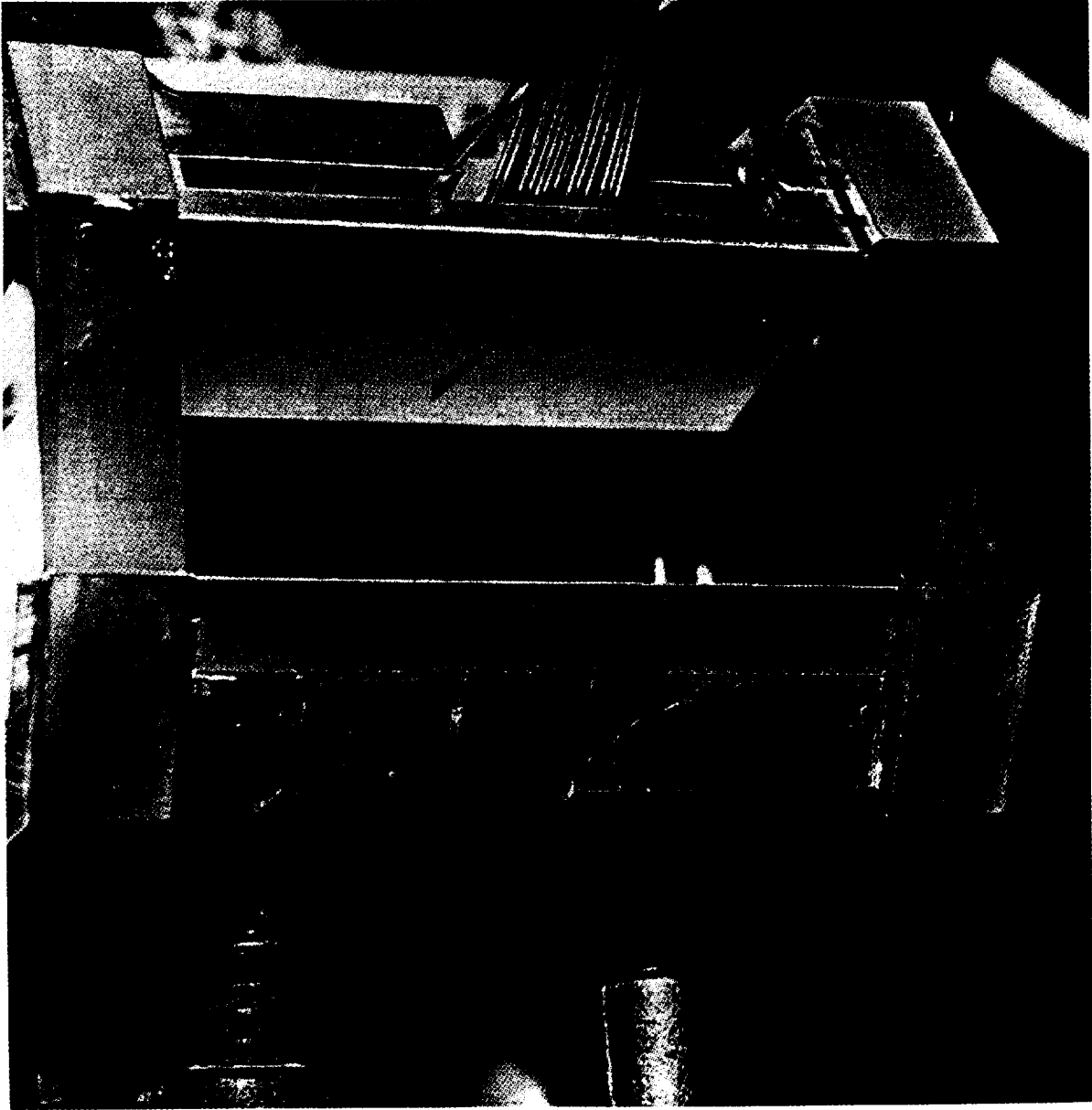


Figure 4.2.4 Active Control Nozzle with Installed Divergent Flap and Cavity



Figure 4.2.5 The Active Control Nozzle and the Eighteen Divergent Flap Configurations

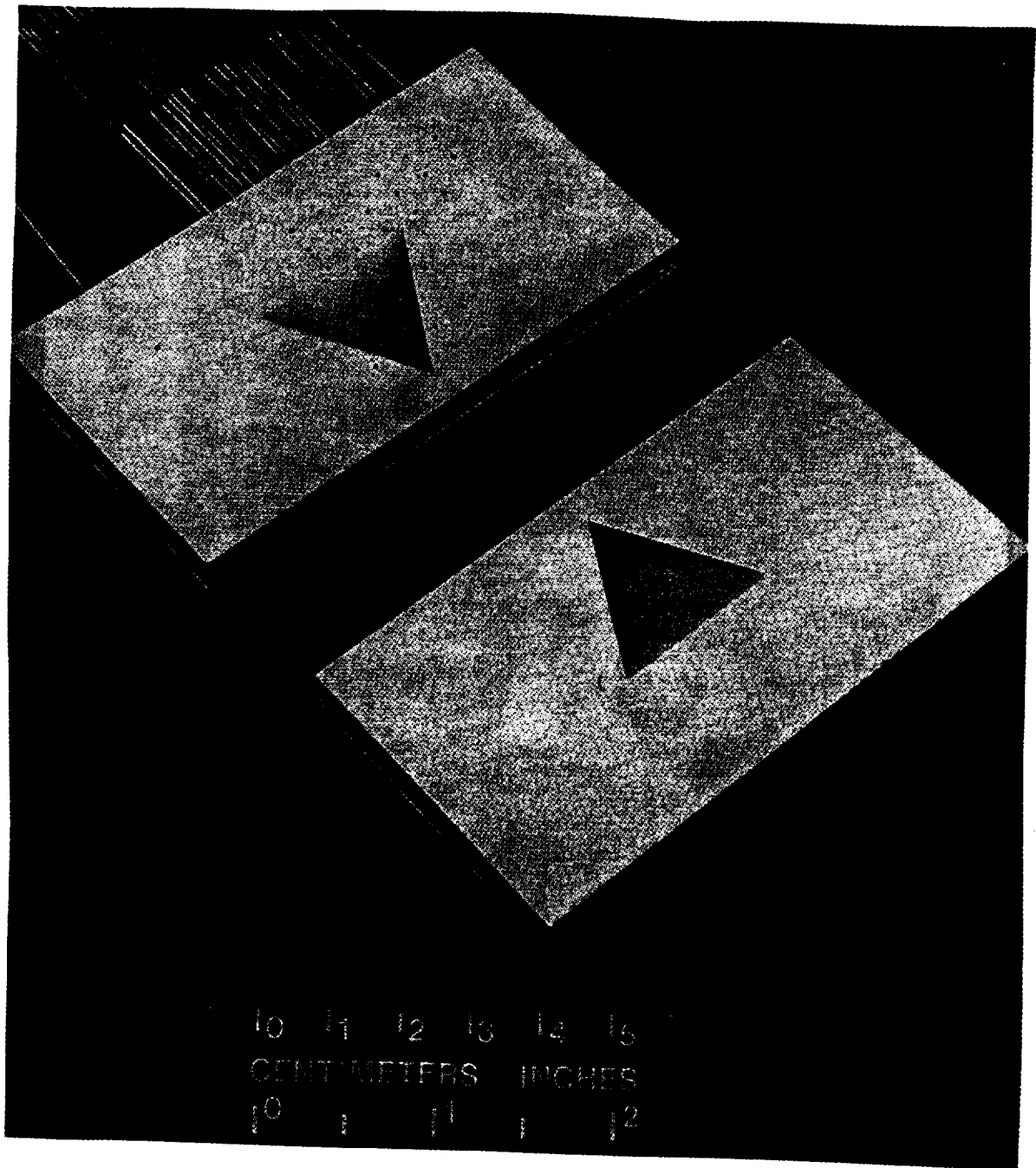


Figure 4.2.6 Photograph of Configuration 6 ( $\theta = 30^\circ$ ,  $\delta = 8^\circ$ )

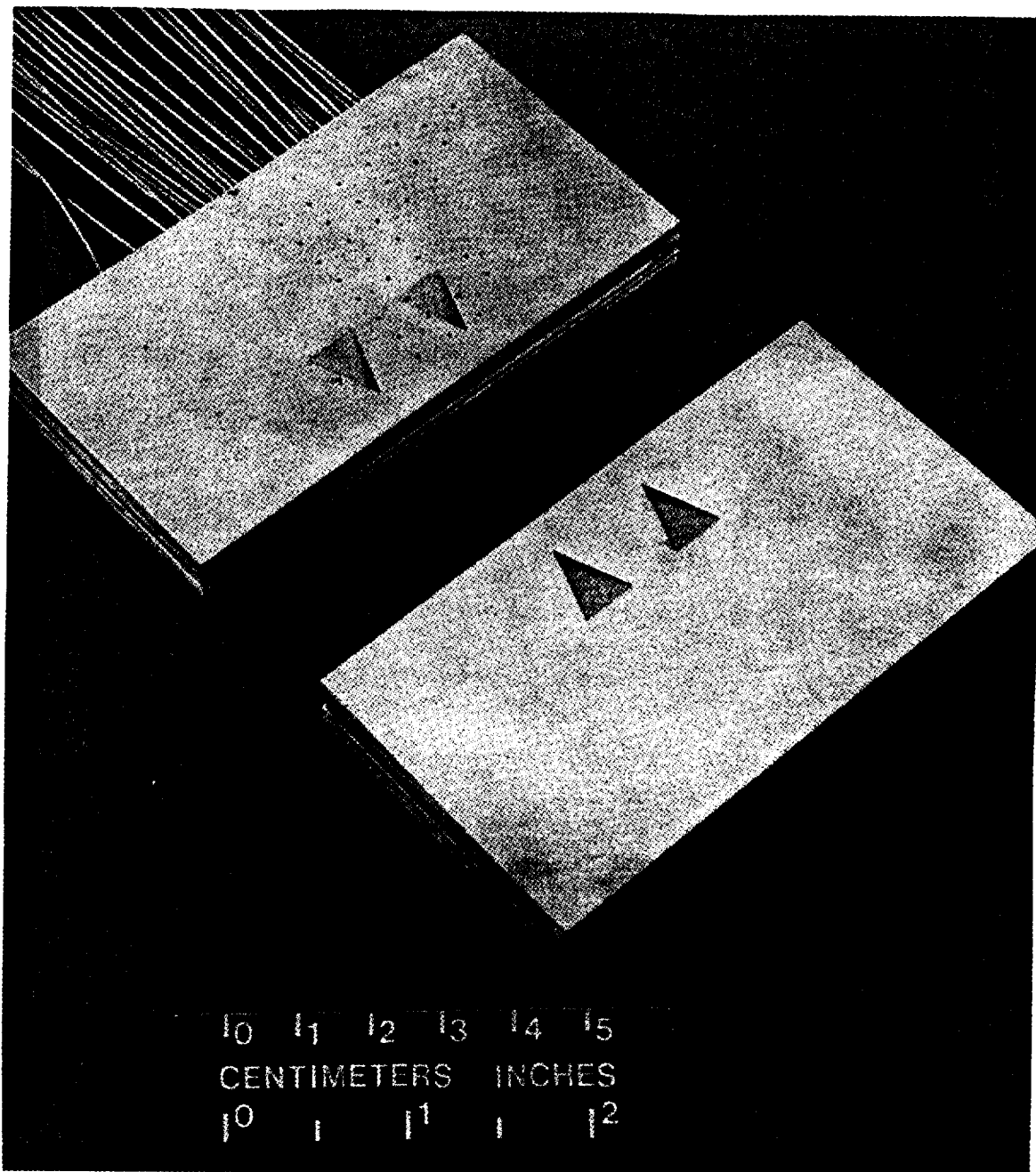


Figure 4.2.7 Photograph of Configuration 11 (2 cavities,  $\theta = 20^\circ$ ,  $\delta = 8^\circ$ )

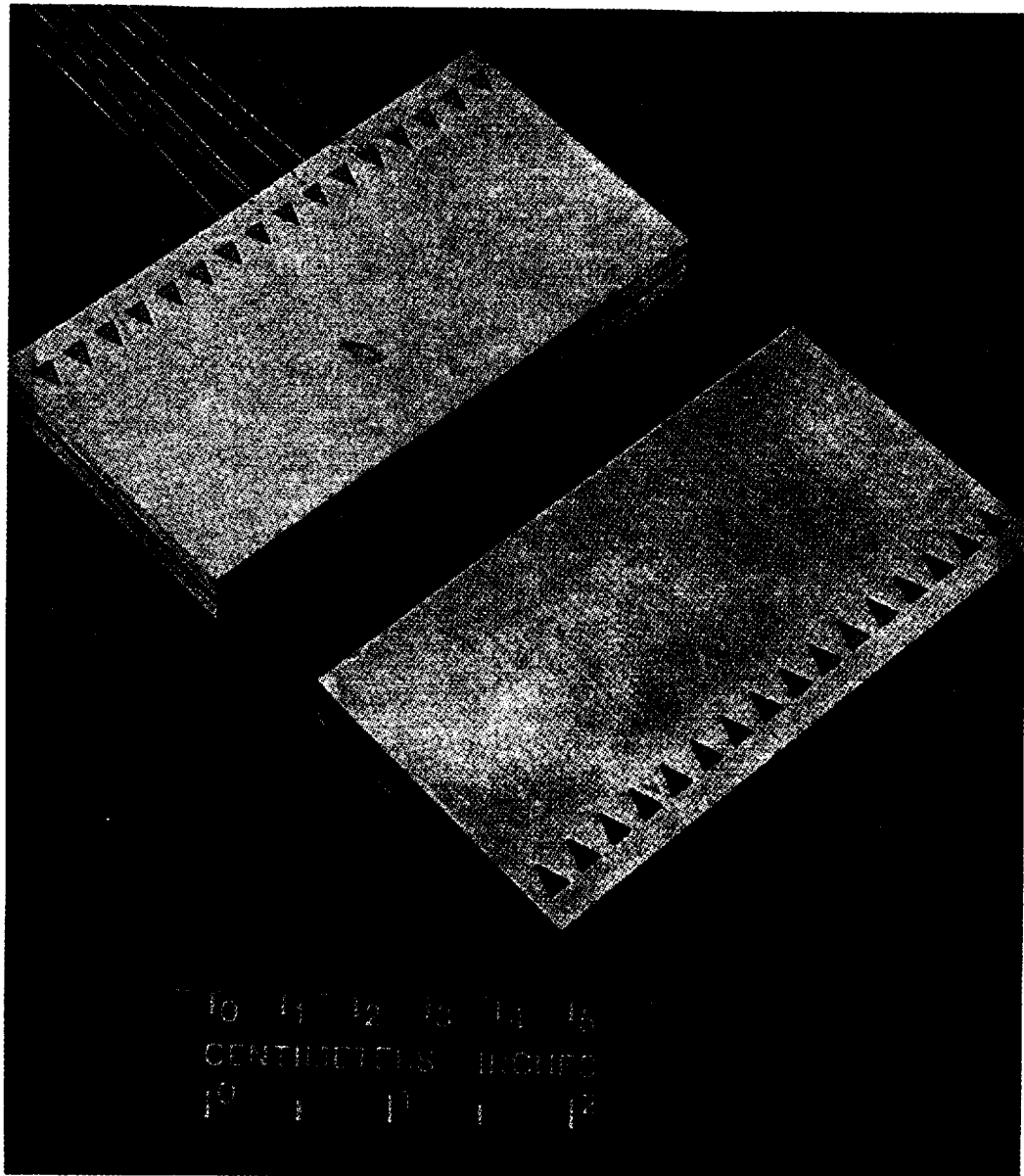


Figure 4.2.8 Photograph of Configuration 21 (16 cavities,  $\theta = 20^\circ$ ,  $\delta = 8^\circ$ )

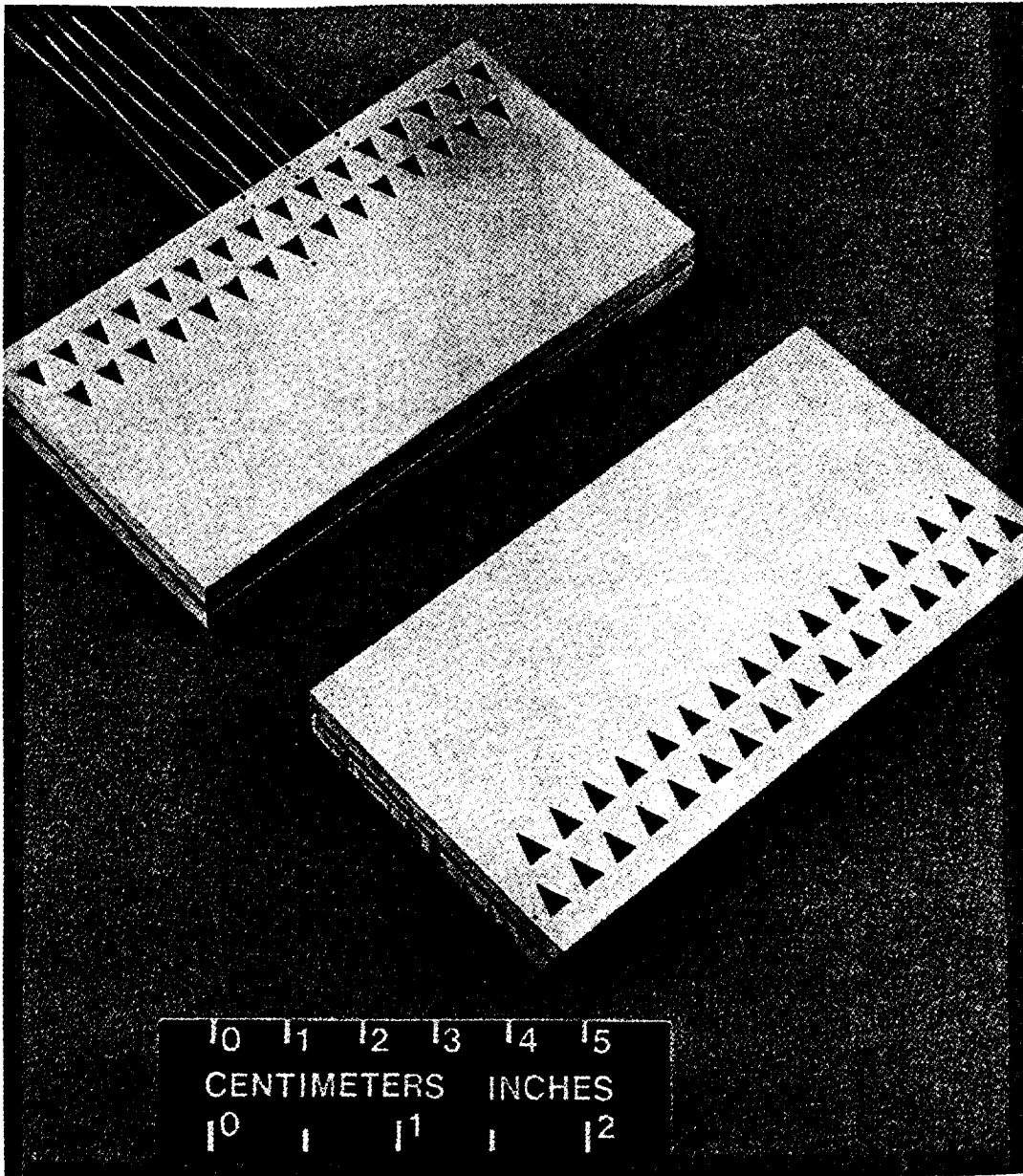


Figure 4.2.9 Photograph of Configuration 22 (31 cavities,  $\theta = 20^\circ$ ,  $\delta = 8^\circ$ )

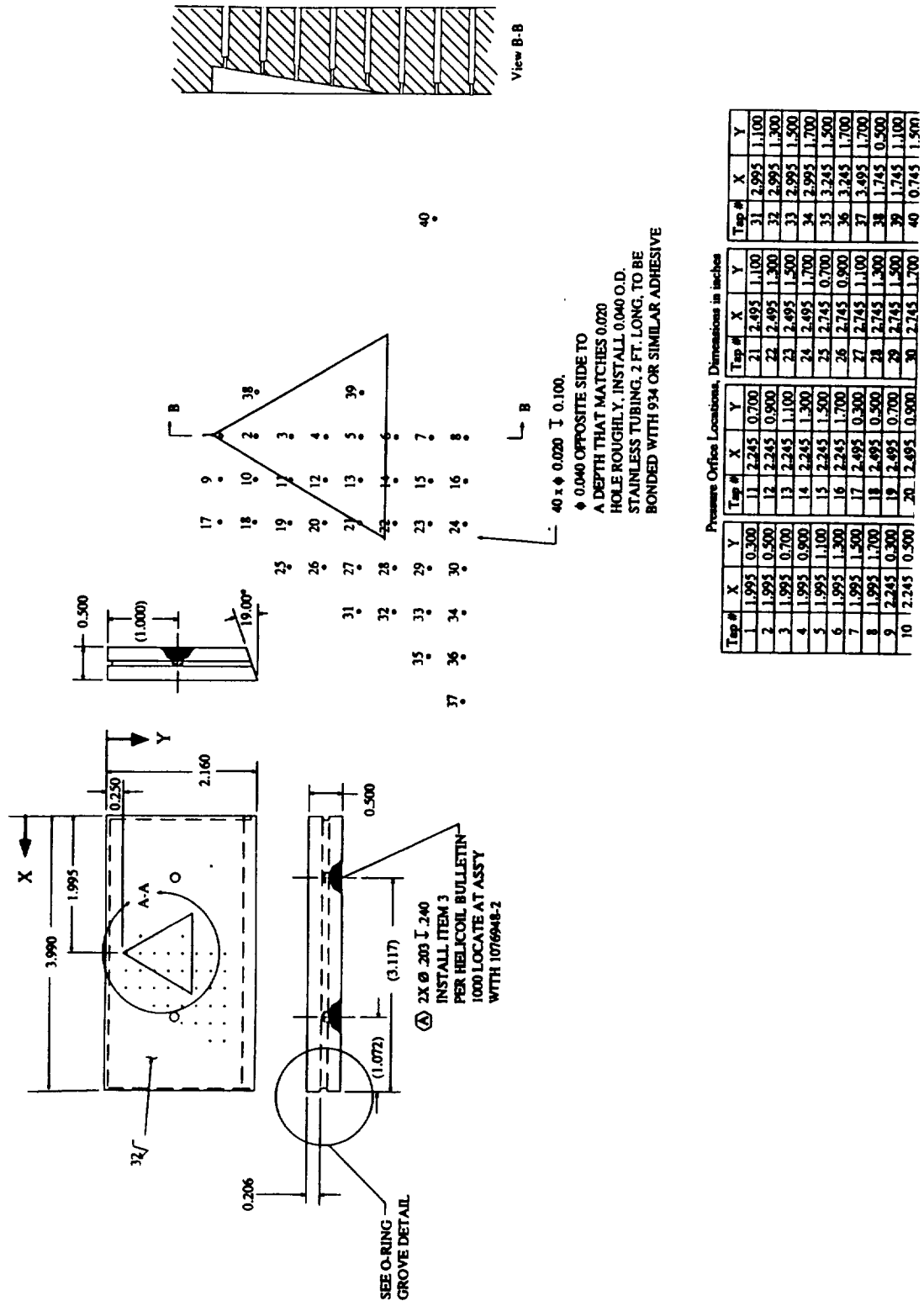


Figure 4.2.10 Schematic of Flap Geometry with ESP Port Locations

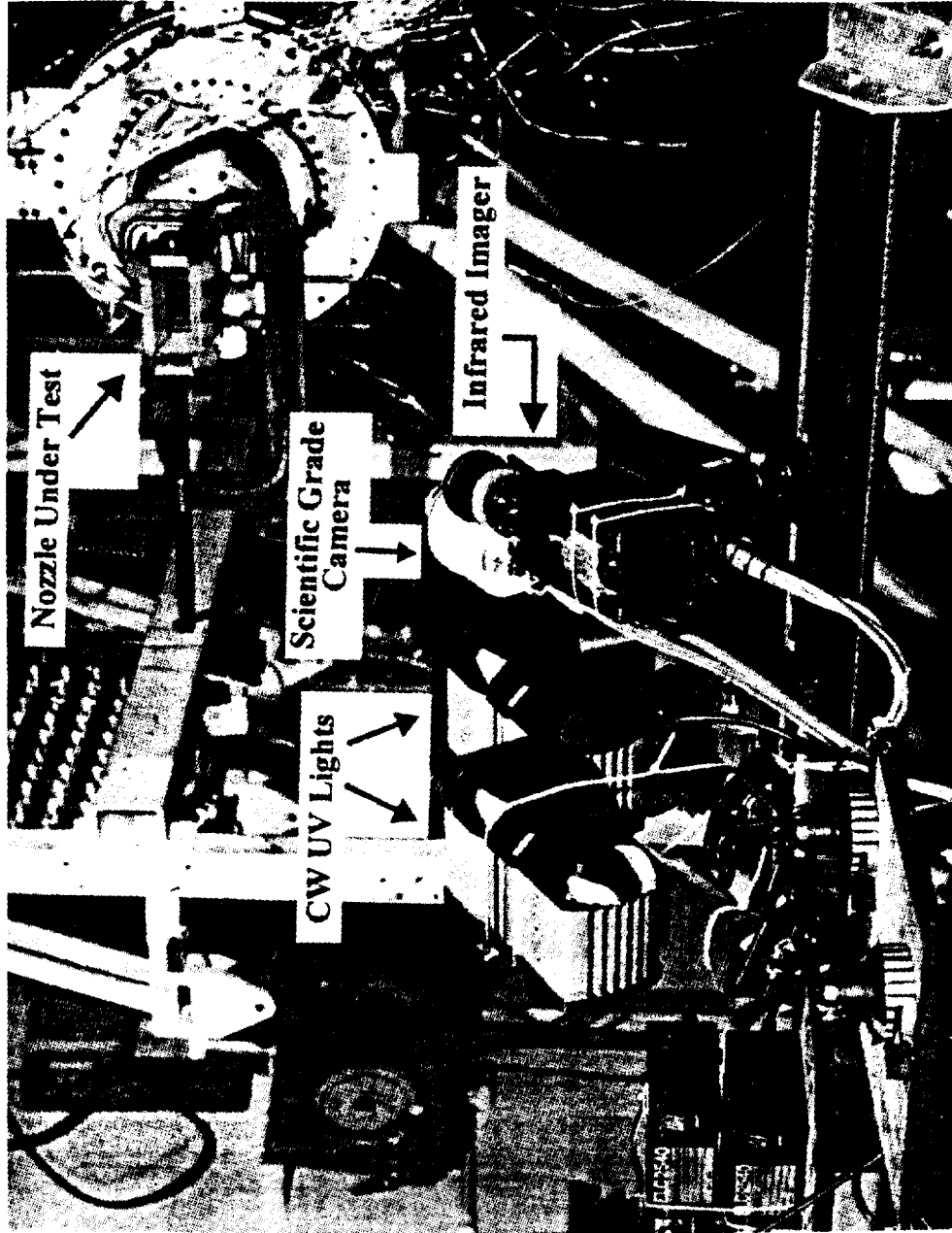


Figure 4.2.11 Photograph of Installed Pressure Instrumentation and PSP Data Acquisition Equipment and the Active Control Nozzle

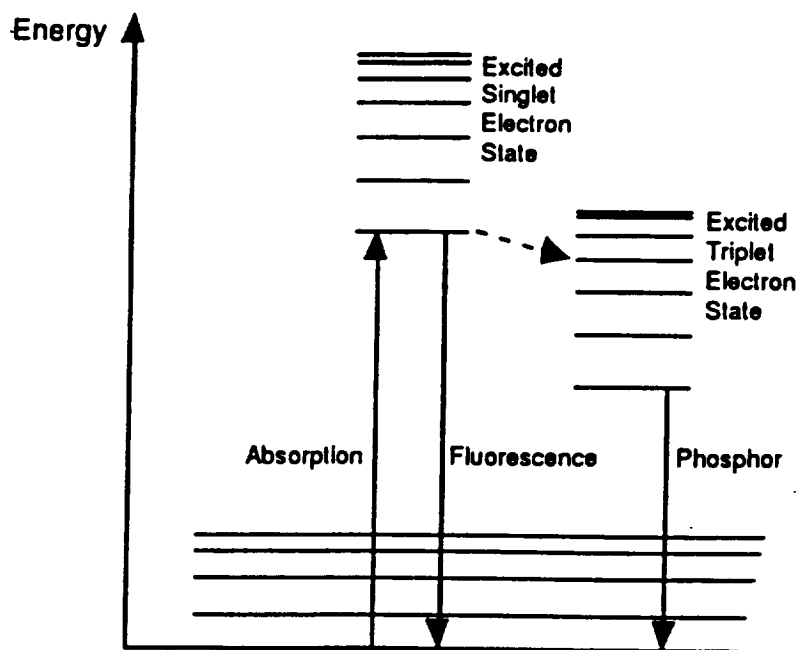


Figure 4.2.12 Molecular Photoluminescence Transition Processes (from ref. 15)

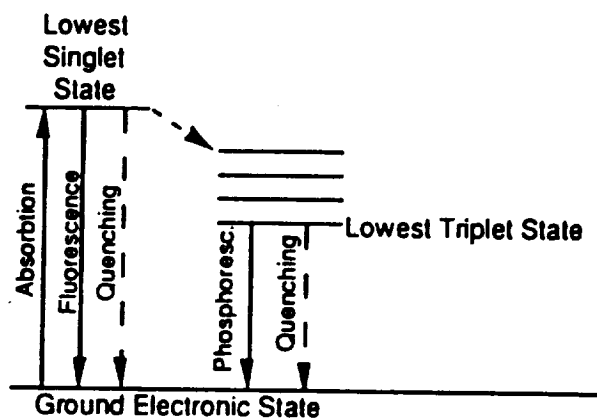


Figure 4.2.13 Molecular Energy Transition to the Ground State (from ref. 15)

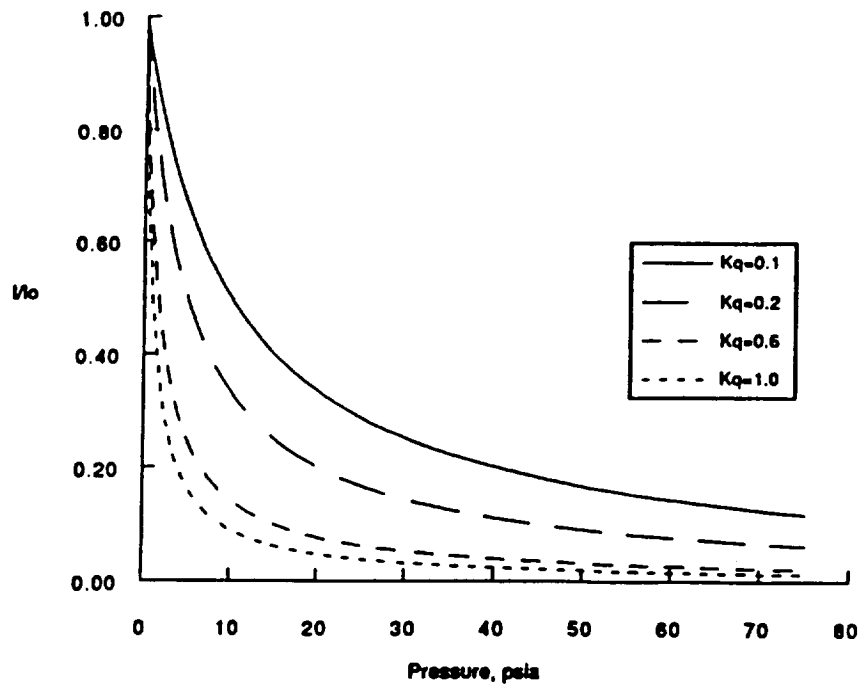


Figure 4.2.14 Sturm-Volmer Relationship for Air (from ref. 15)

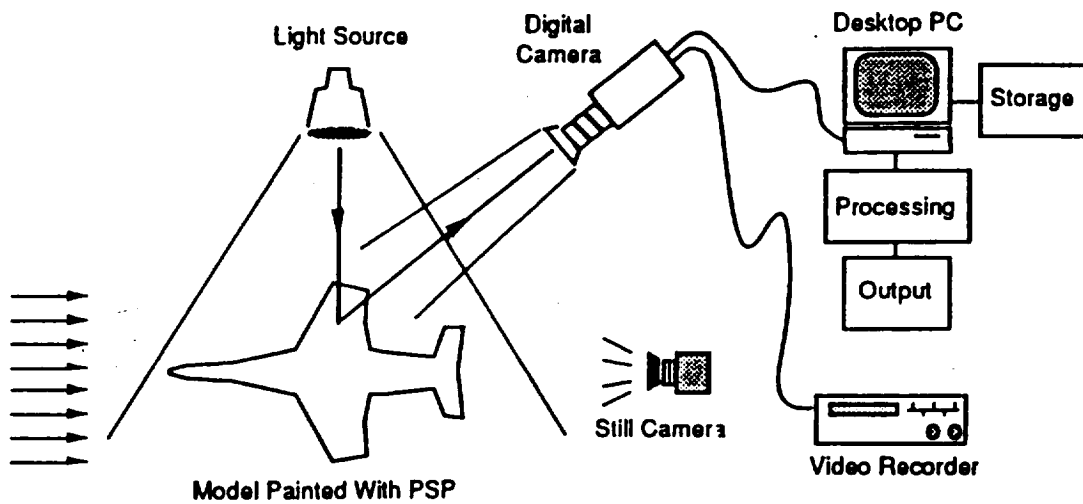
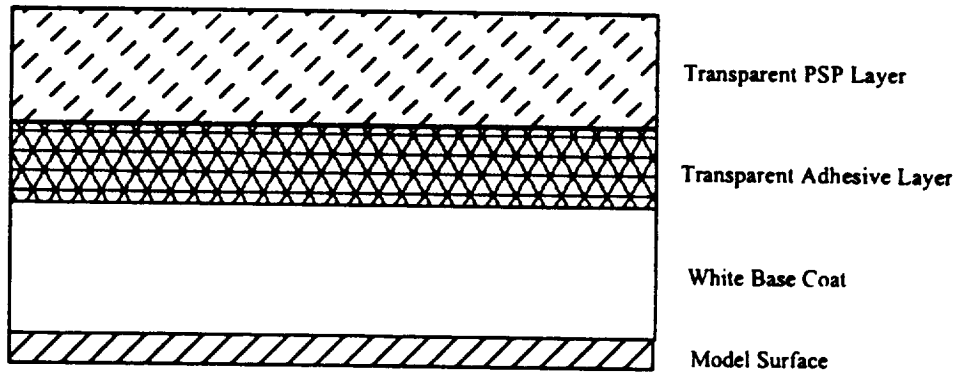
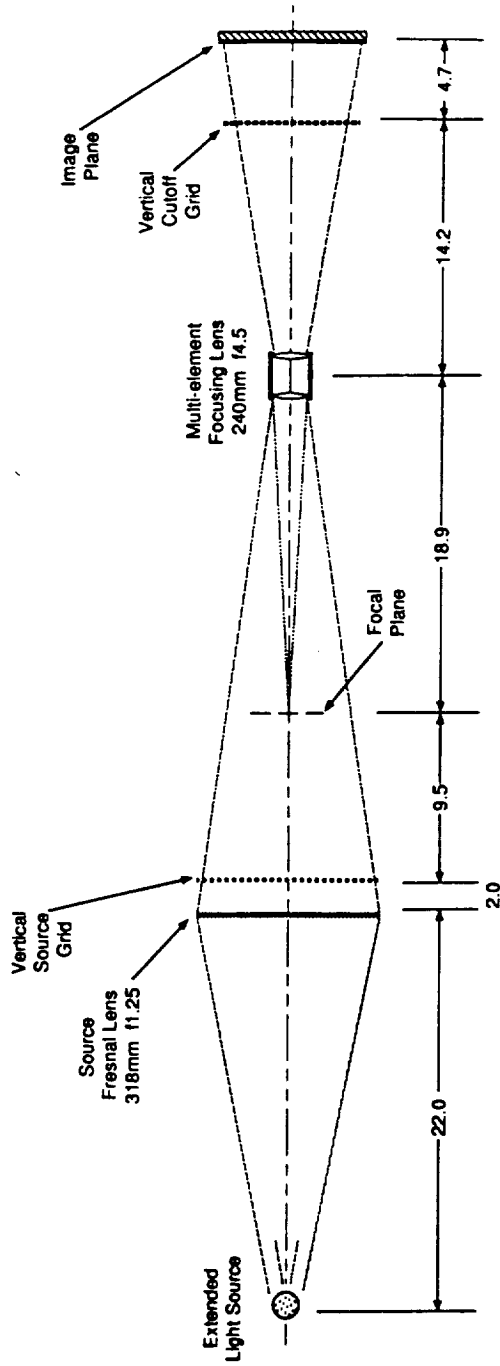


Figure 4.2.15 General PSP Instrumentation System (from ref. 15)



\* No Scale Implied \*

Figure 4.2.16 MDRL Paint Process (from ref. 15)



NOTE: CUTOFF GRID IS OPTICAL NEGATIVE OF SOURCE GRID  
 DIMENSIONS IN INCHES UNLESS OTHERWISE NOTED

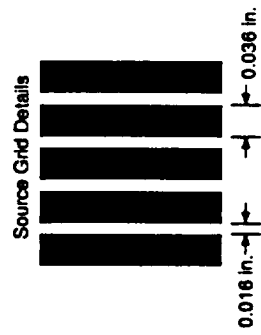


Figure 4.2.17 Optical Description of the Focusing Schlieren System (from ref. 10)

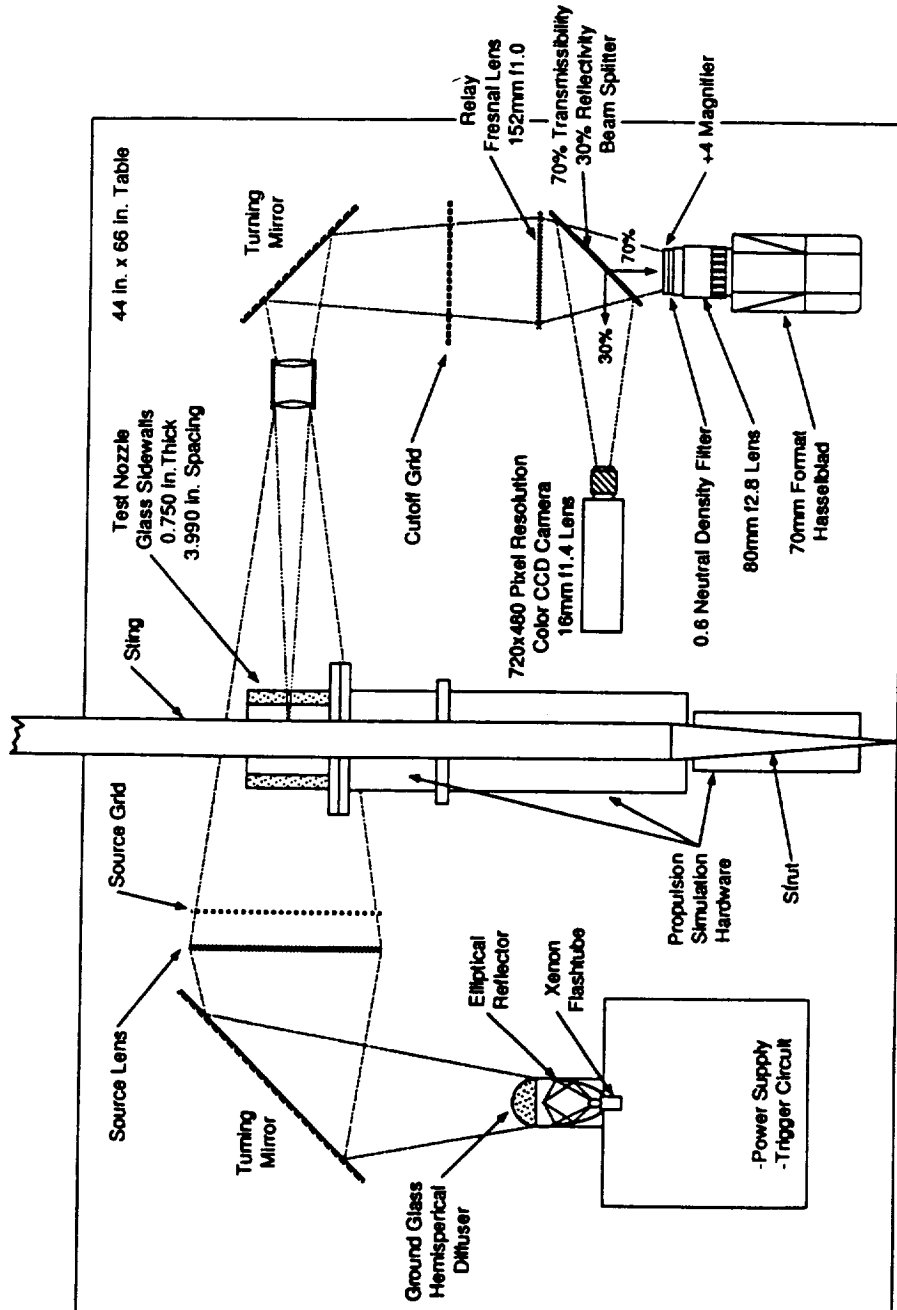


Figure 4.2.18 Layout of the Focusing Schlieren System (from ref. 10)

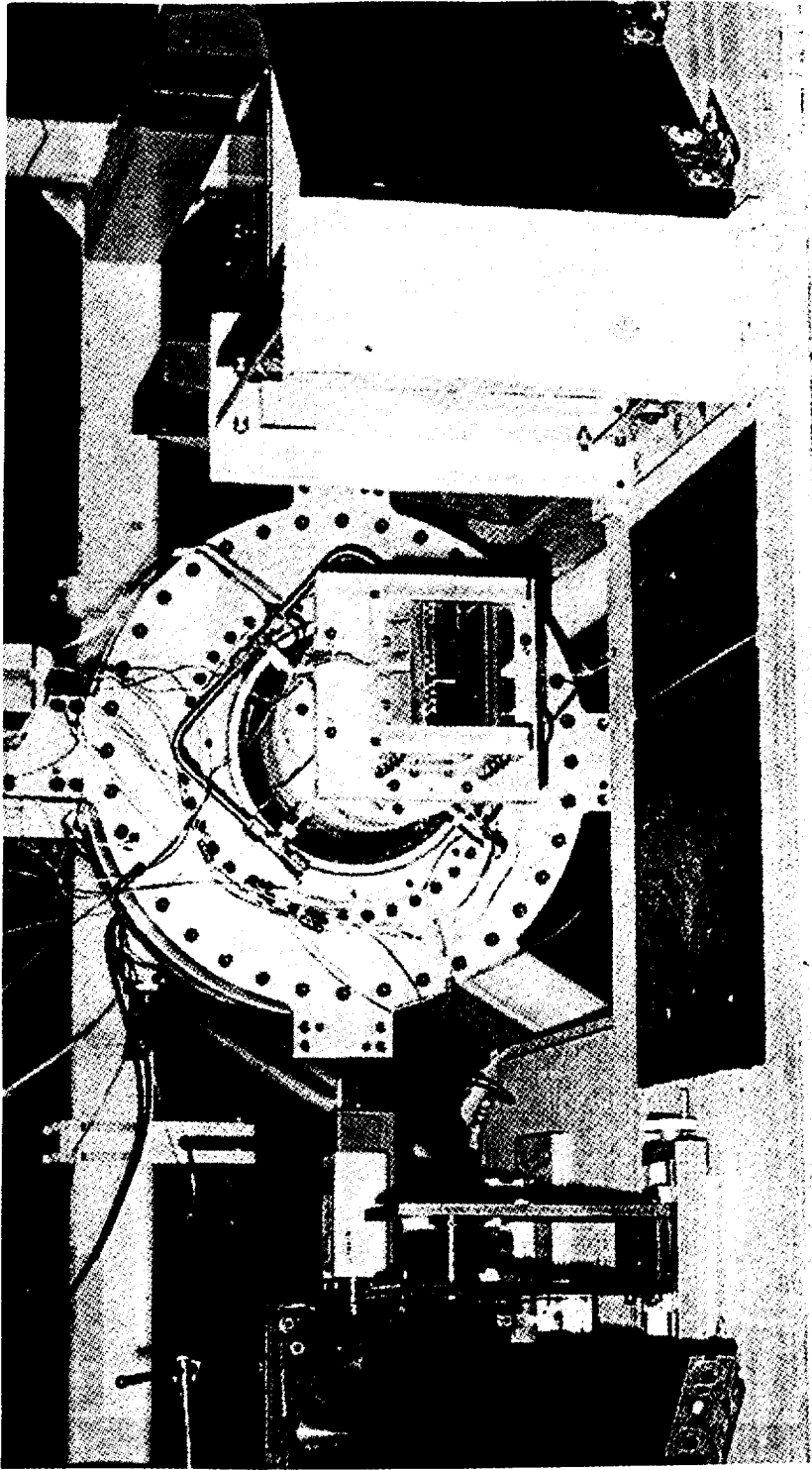


Figure 4.2.19 Photograph of the Focusing Schlieren System

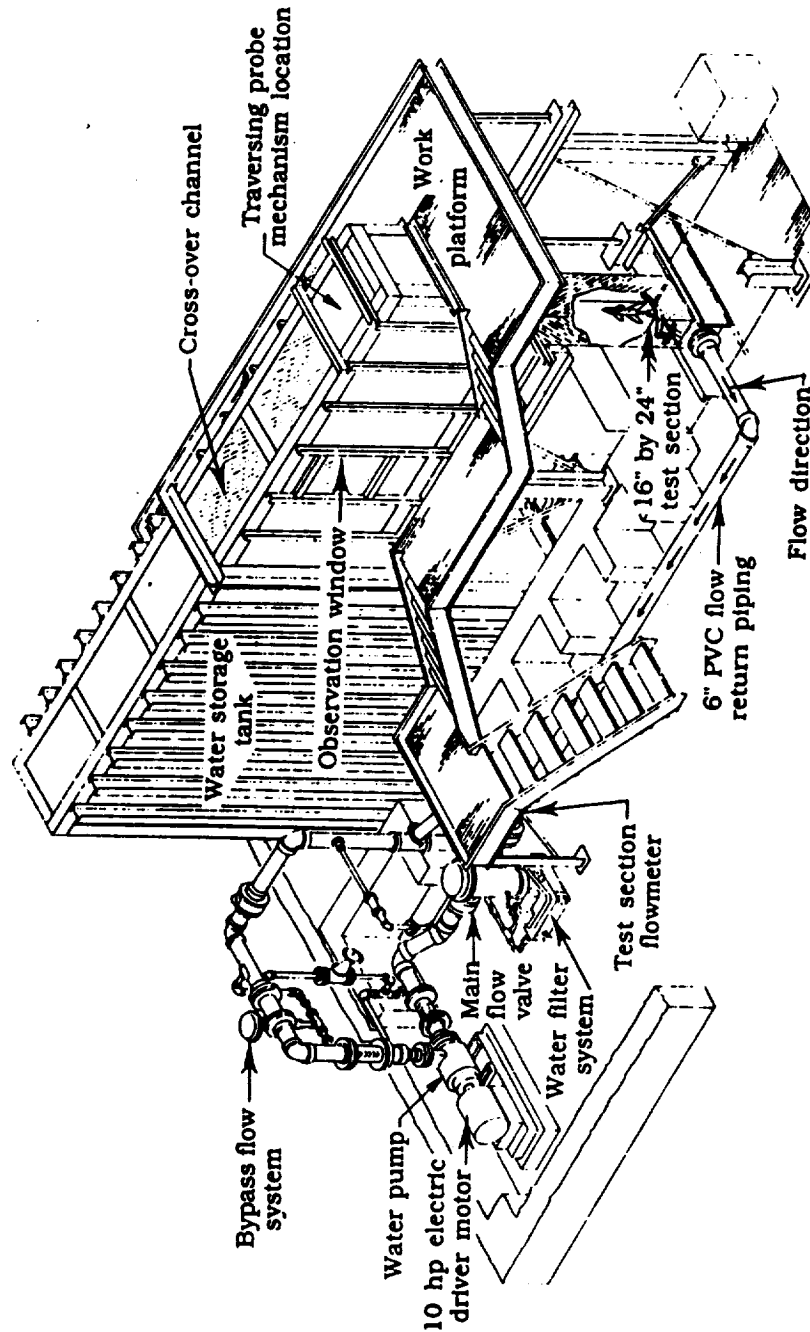


Figure 4.2.20 Isometric View of the Langley 16- by 24- inch Watertunnel

(from ref. 19)



## **5.0 RESULTS AND DISCUSSION**

This section discusses the results of the tests used to investigate the supersonic vortex generator developed at the University of Kansas.

### **5.1 University of Kansas Flow Visualization**

Two different flow visualization techniques were used at the University of Kansas in order to compliment the experiments planned at NASA Langley. Schlieren photography and a relatively new surface flow visualization technique were used to track the vortices.

#### **5.1.1 Schlieren Flow Visualization**

The Schlieren system produced several good pictures which clearly show the generation of streamwise vortices as well as the compression Mach waves produced by the flow dipping into the cavity and then moving up the ramp and the centered expansion fan at the end of the ramp. Figure 5.1.1 shows a typical Schlieren photograph from this test, with no flow. Figure 5.1.2 shows the same VG with a test section Mach number of 2.0. The Schlieren pictures clearly show a vortex forming within the cavity and travelling downstream near the surface of the plate. Figure 5.1.2 shows the vortices as a pale shadow along the edge of the cavity. The core of the vortex is shown to lift off of the surface of the plate slightly and extend downstream past the centered expansion fan at the trailing edge of the ramp. Additionally, the compression Mach waves created by the distributed turning of the flow created by the ramp, show that at least near the surface, the flow is essentially isentropic.

#### **5.1.2 Surface Flow Visualization**

The surface flow visualization system was first used to investigate mixing and flow development within the cavity. Figure 5.1.3 shows a typical surface flow pattern for a ramp

angle of 15 degrees. In the test condition corresponding to figure 5.1.3, dye was injected from three upstream ports to visualize how the airflow mixed through the cavity. Figure 5.1.4 shows the same cavity as in figure 5.1.3 only in this test, dye has been injected from ports inside the cavity. This figure illustrates the mixing of the flow for only one of the streamwise vortices. Figure 5.1.5 shows the cavity with dye injected from three ports inside the cavity.

The surface flow visualization investigation at KU demonstrated several important design considerations that were later employed in the NASA Langley tests. In figure 5.1.3, the presence of the vortex created a region where most of the dye was swept away from the surface. On the upper portion of the same figure, the vortex can be seen as the light band between two darker orange regions of non-vortical flow. The fluid near the vertex is very red, indicating that the majority of the flow in the stagnation region came from the lower portion of the cavity; this may have been caused by asymmetric manufacturing flaws in the construction of the cavity. Ideally, no such asymmetry would be present in the flow. The reason for this large stagnation region will be discussed later.

Flow visualization was also used to investigate the effects of ramp angle,  $\delta$ , on the vortex development. Figure 5.1.5 shows a cavity with a ramp angle of only  $8^\circ$ . Figure 5.1.6 shows the interior of the cavity in detail.

The shallow ramp investigated seems to indicate that the ramp angle can have a significant effect on the flow within the cavity as well as the generation of the vortices. In this configuration, the size of the stagnation region near the vertex was significantly reduced. Additionally, the amount of backflow towards the vertex appears to have been reduced or eliminated; note the yellow color near the vertex as opposed to the reddish color in figure 5.1.3. Unfortunately, this investigation did not determine how the strength of the streamwise vortices was affected by the shallower ramp. Because of this, the NASA Langley investigations included both a deep and a shallow ramp configuration for every wall angle investigated.

The wall angle effects on the flow was also investigated using surface flow visualization. Figure 5.1.7 shows upstream flow patterns in a cavity with straight walls. Figure 5.1.8 details the interior of a straight walled cavity.

In figure 5.1.7, the size of the stagnation area is reduced, although not as much as it was reduced by a shallow ramp angle. Backflow is still clearly present as indicated by the color of

the dye near the vertex in figure 5.1.8. As with the shallow ramp investigation, no determination of the effects on the strength of the vortices was possible.

Finally, the effects of vertex shape on the stagnation region were investigated using surface flow visualization. Figure 5.1.9 shows how upstream flow is affected by a straight vertex. Figure 5.1.10 details the interior of the cavity. Note, no yellow dye could be injected in this configuration since the port near the vertex was covered when the vertex shape was flattened.

The large stagnation region near the flat vertex dramatically demonstrates the need for a sharp vertex shape. By using a flattened vertex, the contoured nature of the cavity was not effective in creating vortices and, in essence, the VG had become a backward-facing step. Therefore, using the results obtained from the tests at KU, the various configurations at NASA Langley could be designed more efficiently. Additionally, the relatively large radius of curvature of the KU configurations when compared to the NASA-Langley models also explains why there are no significant stagnation regions in the NASA photos. Additional photos of each of the various situations investigated are shown in Appendix A.

## **5.2 NASA Langley Flow Visualization and Static Pressure Tests**

Extensive testing of the supersonic vortex generator was performed by the engineers at NASA Langley's Jet Exit Facility. While there were a total of ten single cavity configurations tested, only one will be discussed in detail. Configuration 6 was selected as the sample cavity since this particular configuration seemed to generate the strongest vortices. Configuration 6 had a vertex half-angle of  $30^\circ$  and a ramp angle of  $8^\circ$ . Additionally, six double cavity configurations and two multi-cavity configurations were also tested. Only certain configurations will be discussed here, since many of the configurations provided little additional information.

### 5.2.1 Thrust and Performance Determination

Using the installed capabilities of the Jet Exit Facility, the thrust and weight flow through the nozzle were measured for each configuration tested. In addition, the PSP and pressure tap data were obtained simultaneously. Figure 5.2.1 shows the performance of configuration 6 at various NPRs. The left-most graph shows the gross thrust to ideal thrust ratio, while the central graph shows the net thrust ratio. The right-most graph shows the weight flow ratio for the same nozzle configuration. Figure 5.2.2 shows the effects of two cavities in the flow, in this case configuration 11. Figure 5.2.3 shows the effects of configuration 21 on the performance. Figure 5.2.4 shows configuration 22. Configuration 22 is shown since there are several differences between the thrust ratios of configuration. 21 and 22.

The use of a supersonic vortex generator was expected to produce a reduction in thrust due to the generation of shockwaves. It was hoped that if the generated compression waves were weak, that the loss of thrust would be acceptable when compared to the gains due to vortical flow. At the design NPR of 8.8, the difference between the flat plate and cavity thrust ratios was approximately 0.5%. While a greater loss of thrust was observed at lower NPRs, the loss was 0.5% or less over a surprisingly large NPR range, from 3.5 to 10, with a minimum occurring near NPR=5.0. The largest thrust loss occurred at NPR=2.0 and was approximately 3.5%. The other configurations showed similar results. There was a noticeable reduction of thrust at the lower NPRs, where the nozzle is overexpanded and a shock wave sits inside the divergent portion of the nozzle. This is expected since the cavity would postpone the shock wave and this delay would allow greater expansion of the supersonic flow and a resulting stronger shock.

No trend was identified in the weight flow measurements.

Calculation of the ideal performance parameters was performed by the Data Acquisition system and the equations are given in reference 11. The error in these calculations is approximately 0.25%.

### 5.2.2 Pressure Sensitive Paint and Static Pressure Tap Measurements

The PSP data technique was supplemented by using a matrix of static pressure ports located along one side of the cavities under investigation. These results could then be compared and used to validate each other. The static pressure measurements were also used to calibrate the PSP results. As mentioned previously, the PSP technique had never been used at the pressures that were expected in the nozzle; therefore, the pressure taps were considered a necessity if meaningful pressure data was to be obtained. As it turns out, the PSP technique worked very well for all NPRs and configurations tested.

The ESP modules used to measure the static pressure provided raw data that was used to generate pressure contour plots of the nozzle, with the pressure taps shown as circles. A cubic spline curve fit was used to generate the contour lines shown.

The PSP data was digitized and saved on computer disk. These images were then in situ calibrated using ESP data and printed out using specially designed computer graphics software.

The single cavity configurations were investigated first. Tracking the "footprint" of the vortex was desired. Figure 5.2.5 shows the ESP pressure contour for configuration 6 at NPR=2. The numbers at the end of the pressure contours are the ratio of static pressure to total pressure, the same ratio is used in the PSP data. Figure 5.2.6 shows the same information using PSP.

These figures show the cavity prior to the formation of vortices at NPR=2.0. At this NPR, the nozzle shock wave is situated near the middle of the cavity. It is immediately obvious that the PSP data is far more detailed than the ESP data. The shock wave is clearly defined in the PSP picture, yet barely discernable in the ESP picture. The vortices developed in the supersonic region of the cavity are visible in the PSP data but are not visible in the ESP data.

Figure 5.2.7 shows configuration 6 at the design NPR of 8.8; Figure 5.2.8 shows the same data using PSP. Here, the difference in resolution between the PSP and ESP data is even more apparent. The ESP data failed to capture the true path of the vortex inside and outside of the cavity even with a relatively densely packed array of pressure taps. Additionally, the ESP data did not capture the relatively large high pressure region within the cavity caused by the compression Mach waves of the flow turning up the ramp.

When the multiple cavity configurations were investigated, studying the interaction of the vortices was a priority. While several configurations provided information about the vortex interaction, configuration 13 demonstrated the most dramatic results and those are detailed here. Figure 5.2.9 presents the ESP picture of configuration 13 at the design NPR of 8.8. Figure 5.2.10 shows the PSP results for the same conditions. Again, the ESP data was not able to accurately capture the vortices locations. Additionally, the ESP data does not show how the vortices from the upstream cavity interacted with the downstream cavity. The PSP pictures, on the other hand, clearly show the reenforcement of the left vortex of the upstream cavity as it intersects the lip of the downstream cavity. The central emerging vortex is clearly stronger than either of the outward vortices. The ESP data also failed to show the Mach wave signature visible off of the vertex of both cavities. Again, the PSP data showed the region of high pressure in the cavity that the ESP data only showed in the downstream cavity.

The effect of the ramp angle on the development of the vortices is illustrated in Figure 5.2.11a. This figure shows the PSP data for configuration 5, which has a shallow,  $4^\circ$  ramp. The vortices developed by the shallow ramp are not as strong as the ones generated by the deep ramp. Also, the stagnation region near the vertex is smaller than the region for configuration 6. This test verified the results obtained at KU. However, as shown in the KU investigations, if the ramp is too deep, a large stagnation region can form at the vertex of the cavity, reducing the effectiveness of the vortex generator. Thus, there is a design trade-off necessary to create a cavity shape that will generate strong vortices while minimizing losses due to the stagnation region.

Figure 5.2.11b shows how a supersonic cavity lip can affect the vortex development. When the cavity lip is exposed to supersonic normal flow, the cavity does not generate strong vortices. As can be seen from the figure, only a very weak vortex pair are created by this configuration. When the upstream flow is exposed to a supersonic lip, the cavity acts like a backward-facing step.

One cavity was designed with a cubic spline shaped lip. This configuration is shown in Figure 5.2.11c. The cubic spline shaped lip shows that most of the vortex is developed in the subsonic lip region. Additionally, there is a high pressure region located at the inflection point

of the cavity walls. This high pressure region was caused by the shock wave created when the flow turned into itself inside the cavity.

The effect of the cavity on the shock structure of an overexpanded nozzle was investigated. The shock structure at NPR=3.0 on configuration 6 is shown in Figure 5.2.11d. The same configuration is shown at NPR=3.5 in Figure 5.2.11e. At an NPR of approximately 3.5 the nature of the shock structure at the base of the cavity changed. In figure 5.2.11d, the shock wave caused by the overexpanded nozzle is located near the baseline of the cavity at NPR=3.0. Clearly, the shock is delayed in a region just downstream of the cavity as was expected. The nature of this delay in the shock has changed by NPR=3.5. In figure 5.2.11e, the region where the shock is delayed is associated more with the emerging vortices. At this NPR, the first indications of the flow path of the vortices becomes visible. Additionally, the vortices were strong enough to penetrate the shock wave and continue downstream in the subsonic regime.

Unfortunately, due to the small size of the cavities, pressure information for configurations 21 or 22 was not obtained. For the ESPs, the size of the cavities were the same order of magnitude as the size of the orifices. For the PSP data, the paint filled the small cavities and this technique could not be used. Additional cavity configurations are shown in Appendix B.

### 5.2.3 PSP Error Analysis

Detailed error analysis of the ESP and PSP data was performed and the results published (ref. 20). The following is a brief summary of that analysis. Table 5.2.1 summarizes the percent error in PSP pressure measurement relative to the ESP tap data for configuration 8 at several NPR values. Listed in this table are the NPR, number of ESP taps used to calibrate the PSP, the range of pressure spanned by the ESP taps, mean relative error in PSP measurement, and the uncertainty in PSP measurement at 95% confidence level.

Table 5.2.1. Summary of PSP Analysis Results for Configuration 6 of the C-D Nozzle

NPR	No. ESP	Range of ESP Pressures (psi)	$\epsilon$ Pressures (psi)	$2\sigma$ of ESP-PSP (psi)
2.0	32	7.3 - 15.5	2.13	0.55
3.0	29	6.3 - 14.7	2.11	0.56
3.5	29	7.3 - 17.2	2.13	0.58
4.0	29	7.8 - 19.8	2.29	0.64
5.0	30	9.1 - 24.8	2.58	0.83
6.0	31	10.9 - 29.9	2.61	1.06
7.0	30	12.8 - 35.0	2.38	1.11
8.0	30	14.7 - 40.1	2.39	1.34
8.8	30	16.2 - 44.2	2.58	1.63
10.0	30	18.5 - 50.5	3.33	2.28

Note, this configuration of the nozzle had 34 ESP taps, some of which could not be used for the data obtained in Table 5.2.1. Note also that the modules have 100 psi range and an accuracy of 0.25% of full scale. This 0.25% accuracy translates into 0.25 psi [ 1.7 kPa] uncertainty in pressure measurement.

The increase in mean relative error and pressure measurement uncertainty as NPR increased was attributed to several factors. As mentioned earlier, the PSP emission intensity is related to the inverse of the pressure. Since the light integration time for the camera was fixed during the experiment, the signal to noise ratio of the intensity measurement decreased with increased pressure measurement error. Other contributing factors were the wider pressure span and larger surface temperature variations of the model at higher NPRs.

#### 5.2.4 Focusing Schlieren Flow Visualization

The focusing Schlieren system allowed a detailed analysis of the shock-cavity interactions to be performed at various NPRs for various configurations. Figure 5.2.12 shows a photo taken along the centerline of the cavity for configuration 1 at NPR=2. Figure 5.2.13 shows the same NPR for configuration 6. In both cases a cavity was installed on the lower surface of the nozzle with a flat plate installed on the upper surface. Additional configurations and NPRs can be found in Appendix B.

In both cases, the forward leaning edge of the passage  $\lambda$ -shock structure was significantly reduced. When a larger vertex angled cavity was placed in the same flow, figure 5.2.13, the  $\lambda$ -shock was almost completely eliminated.

The effects of a single cavity installed verses having a cavity installed on the upper and lower surface was also investigated. Figure 5.2.14 shows configuration 6 installed only on the lower surface at design NPR, while Figure 5.2.15 shows a cavity installed on both the upper and the lower surface. Additional configurations are shown in Appendix B.

The weak shock emanating from the lower flap of figure 5.2.14 is due to the concave curvature of the streamlines into the cavity, see figure 3.2.1. Also, the centered expansion fan at the base of the cavity is caused by the flow emerging from the cavity and turning out of itself to travel along the plate. Unfortunately, the focusing Schlieren system was not able to image any of the vortical structures generated by the cavities.

The Schlieren system did not provide additional information when multiple cavity situations were investigated. This was due to the limiting nature of the focusing system. The location of the vortices was not known in advance and the system could not be refocused to locate them. As a result, no additional information was gained.

Configurations 21 and 22 both allowed for an investigation of the effects on the shear layer of the emerging jet. Configuration 22 provided clearer results since the cavities were installed farther away from the lip, allowing the vortices to develop further. Figure 5.2.16 shows configuration 22 at design NPR, the cavities were only installed on the lower surface.

In the figure, there is a definite increase in the mixing rate of the emerging flow. This is due to the vortical nature of the emerging flow into the shear layer. The vortical flow entrains additional stagnant air, thereby reducing the overall mixing length of the nozzle exhaust.

### 5.2.5 Laser Light Sheet Flow Visualization

The laser light sheet was used to visualize the vortices at various selected streamwise locations relative to the cavities. Additionally, sweeps of the nozzle were performed to dramatically demonstrate the entire vortex structure. The laser information was saved onto standard VHS videotape and still pictures were made of the desired frames. The camera was mounted behind the nozzle, so all pictures were taken looking into the nozzle with flow coming out of the page.

Unfortunately, due to buffeting of the camera during nozzle operation, many of the pictures were fuzzy. However, several good views were obtained and Figure 5.2.17 shows the development of the streamwise vortices for configuration 6. The right side vortex development was captured in the figure; however the left side vortex was not as well shown. This technique allowed the location of the vortices to be determined in 3-D space. Previous tests had only been able to determine the "footprint" of the vortex in the X-Y plane; with the laser, the Z location of the vortex was visualized for the first time. As predicted, the vortex remained very close to the lower surface.

Some information about the interaction of the vortices for multiple cavity was obtained. Figure 5.2.18 shows how the four vortices interact for configuration 13. In this case, the two cavities were located such that two of the emerging vortices between them combined into one larger vortex. This can be seen in the figure as a much larger and more defined vortex between two normal sized vortices. Vortex destruction was also possible by placing VGs in locations that would cause the inner vortices to cancel each other out. Several additional configurations are shown in Appendix B.

## 5.2.6 Water Tunnel Flow Visualization

Several configurations were investigated in the NASA Langley water tunnel facility. Both dye injection and laser light sheet photos were taken. The water tunnel tests were used to better understand the generation of the vortices within the cavity itself. Since the Reynold's number of the water flow was orders of magnitude lower than that of the supersonic nozzle, any conclusions drawn from these tests must be guarded. Additionally, since the water flow is viscous dominated, the effects of viscosity on the generation of streamwise vortices is clearly evident since these vortices still formed even without supersonic flow. Figure 5.2.19 shows how a stagnation region forms at the tip and the vortices develop outward from there. The photo also shows the relatively large boundary layer flow that travels along the wall and exits without being entrained into the vortex. The core of the vortex is clearly visible in the upper structure. When this picture is combined with those taken at KU (see figures 5.1.3-6) a better understanding of the nature of the flow within the cavity is obtained.

The laser light sheet used to visualize the water flow produced perhaps the most stunning photos of the entire investigation. Figure 5.2.20 shows both counter-rotating vortices as they emerge from the cavity. The internal structure of the vortices is clearly visible. In this figure, the picture was taken looking into the flow with the laser sheet cutting the flow near the base of the cavity.

The streamwise evolution of the vortex can be seen in Figure 5.2.21. Here, the laser was directed along the lip of the cavity, with flow from right to left. This picture details the nature of the vortex as it gathers strength from the surrounding flow as it progresses up the cavity ramp. Additional photos are in Appendix B.

The use of the water tunnel allowed investigation of a backward facing cavity. In particular, the shear layer interactions could be investigated. While this design would not be practical in supersonic applications, it did provide some useful insight into the nature of shear layer interaction for this type of shaped cavity. Figure 5.2.22 shows configuration 5 backwards in the flow. This photo dramatically revealed the streamwise evolution of Kelvin-Helmholtz instabilities generated by mixing the stagnant water inside the cavity with the moving water of the tunnel.

Figure 5.2.23 shows the same configuration, this time viewed into the flow. The internal cell structure of the instabilities are detailed.

### **5.3 Computational Fluid Dynamics Results**

The evolution of counter-rotating streamwise vortices in supersonic flow was determined using computational fluid dynamics techniques to determine if current CFD codes were adequate in predicting the complex flow created by a supersonic vortex generator. For this purpose, the PAB3D code developed by engineers of the propulsion aerodynamics branch at NASA Langley was used, with the computations being performed on the CRAY Y-MP computer system at NASA Langley. Two flow regimes were investigated in preliminary testing, a flat plate model, and a cavity in the divergent portion of a C-D nozzle. The model used simulated the conditions that a cavity would see under different types of flow. The geometry of the cavities investigated was the same as those used in the NASA Langley experiments. Whenever the configuration geometry was used, the configuration number from the experimental results was utilized.

#### **5.3.1 Flat Plate Modelling**

The initial computational investigation of a shaped cavity in supersonic flow was made using a flat plate model. In this situation, the cavity was placed into a Mach 2.0 flowfield over a flat plate with infinite boundaries.

Figure 5.3.1 shows an intermediate solution for static pressure within the configuration 1 cavity. Figure 5.3.2 shows the solution for configuration 6. In these figures, the locations of the vortices was clearly shown. A relatively large region of high pressure was located at the base of the cavity, this high pressure region was detected in the experimental investigations. The relative strength of the vortices due to the cavity shape can also clearly be seen. In figure 5.3.2, the vortices are much stronger than those in the narrower cavity in figure 5.3.1. Although the solutions obtained for the flat plate model did converge, they are presented here as intermediate solutions due to grid problems discovered later in the investigation. These grid problems will be discussed in detail later in this report.

### **5.3.2 Expanding Flow Modelling**

The grid files were modified following the flat plate investigations to conform with the nozzle inserts used in the experimental investigation. Unfortunately, this is where the grid matching problems first manifested. Due to the improper matching characteristics between the grid blocks, the vortex information was not properly transmitted to the downstream block (block 4). As a result, no converged solutions were obtained. After 156 full-grid iterations, the downstream absolute pressure was calculated to be less than zero, and no further iterations using this grid were possible.

### **5.3.3 Grid Resolution Problems**

The inability of the PAB3D code to converge to a meaningful solution has been traced to the grid generation. The grid generated for the expanding flow model was not smooth enough. The following problems were identified.

Figure 5.3.3 shows the grid viewed from an oblique angle, with the problem areas highlighted. The grid spacing at the end of block 1 and the beginning of block 2 are not identical. Additionally, the grid spacing between the end of block 2 and the beginning of block 4 are also not equal. As a result, the code cannot converge. These problems can be easily solved by adjusting the parameters in the `ssvg.dsg` input file to equally space the adjoining blocks.

Figure 5.3.4 shows a view of the grid from above. In this figure, the problems with the grid spacing are much more pronounced. First, the grid expands much too rapidly away from the walls of the cavity and from the expected vortex path. The solutions to this problem are more complex. A combination of increasing the number of grid points defined outside the boundary layer, increasing the boundary layer thickness definition and increasing the starting interval within the boundary layer are necessary. Since each of these parameters effects the others, an iterative approach must be taken to ensure a smooth grid with a boundary layer dense enough and large enough to capture the large pressure gradients within the streamwise vortices being created by the cavity.

The location of the boundary layers used to capture the vortices in block 4 also caused problems. Due to the large pressure gradients within the vortices, the exact location of the vortex must be known to ensure that the boundary layer grids capture the entire flow. The location of the boundary layer grids must be adjusted by modifying the `ssvg.in` file parameters. This process proved long and tedious, especially since the exact location of the vortex was not originally known. Once the experimental data determined the exact location and flowpath of the vortices for a given configuration, the boundary layer grid could be modified to ensure capture of the emerging vortex. However, the experimental data showed that the location and path of the vortices were configuration dependent. As a result of this finding, the boundary layer definitions must be modified for each configuration. The use of an adaptive grid generation scheme in this situation might provide greater flexibility in designing the grid for vortex capture. The PAB3D code could be modified to allow the use of an adaptive grid generator.

In addition to the grid spacing problems, a problem with the quality of the inflow was discovered. To solve this problem, additional inflow blocks must be included in any future grids. The inflow area should include a region of constant area followed by the convergent portion of the nozzle and the throat, then the divergent portion already defined should be used. Figure 5.3.5 shows a sample of the necessary block and grid definitions.

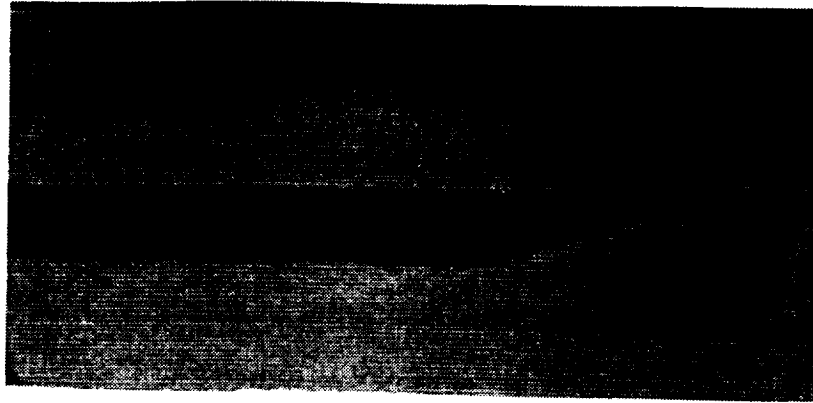


Figure 5.1.1 Schlieren Photograph of Configuration A, No Flow ( $\theta = 20^\circ$ ,  $\delta = 15^\circ$ )

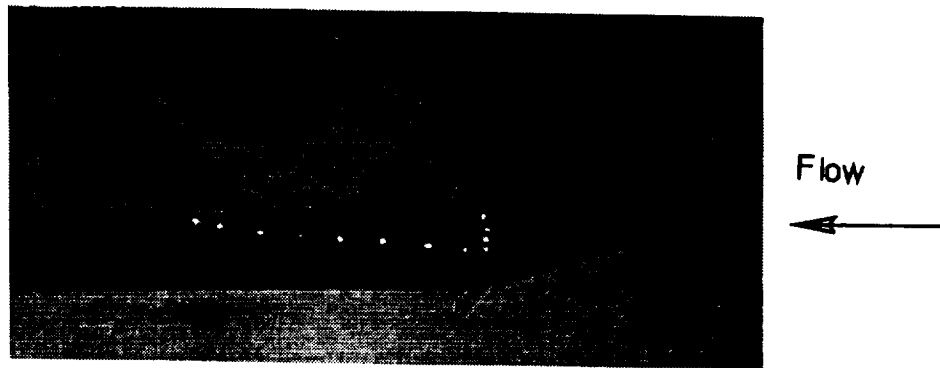


Figure 5.1.2 Schlieren Photograph of Configuration A, Mach = 2.0 ( $\theta = 20^\circ$ ,  $\delta = 15^\circ$ )

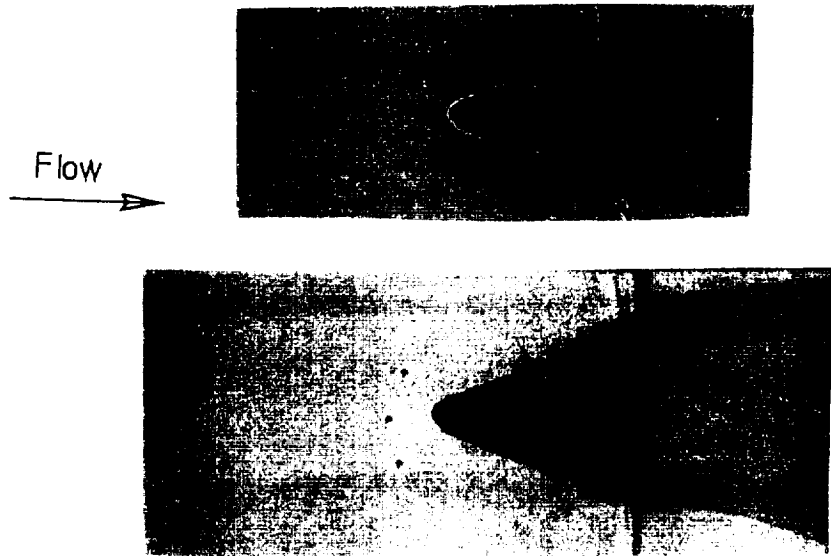


Figure 5.1.3 Surface Flow Pattern with Dye Injected for Surface Flow Visualization, Configuration B, Indented Walls ( $\theta= 20^\circ$ ,  $\delta= 15^\circ$ )

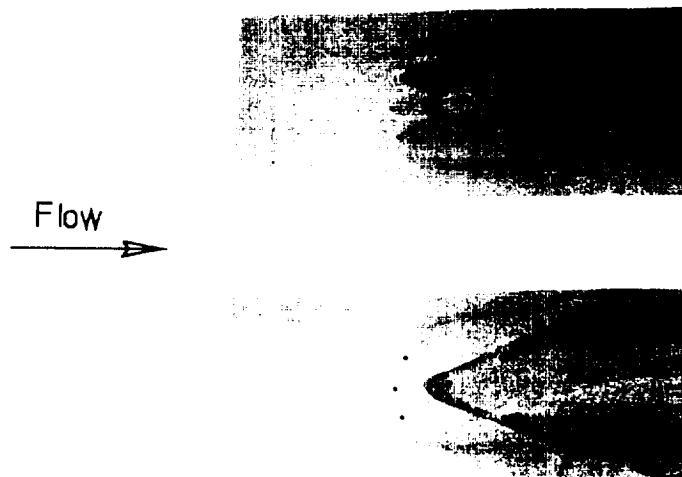


Figure 5.1.4 Surface Flow Pattern with Dye Injected for Surface Flow Visualization, Configuration C, Straight Walls ( $\theta= 20^\circ$ ,  $\delta= 15^\circ$ )

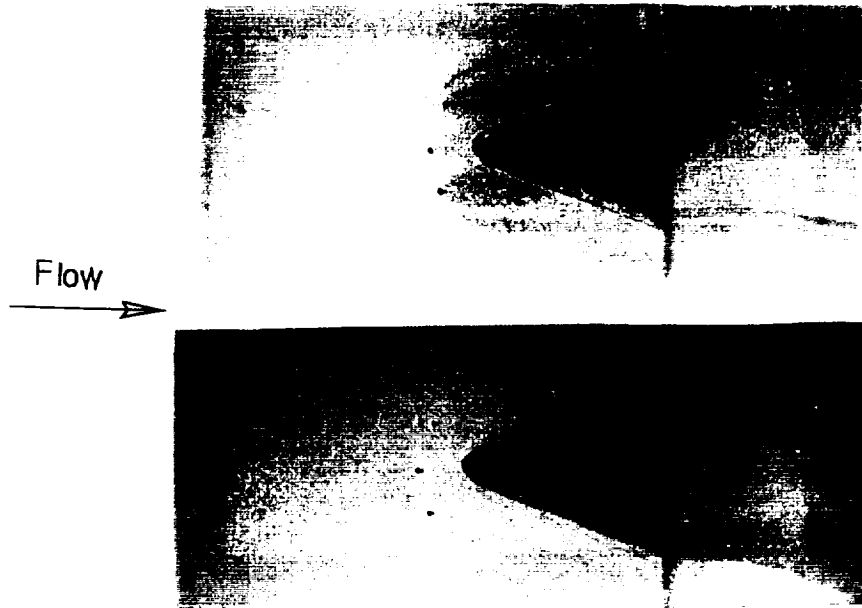


Figure 5.1.5 Surface Flow Pattern with Dye Injected for Surface Flow Visualization, Configuration D, Shallow Ramp ( $\theta = 20^\circ$ ,  $\delta = 15^\circ$ )

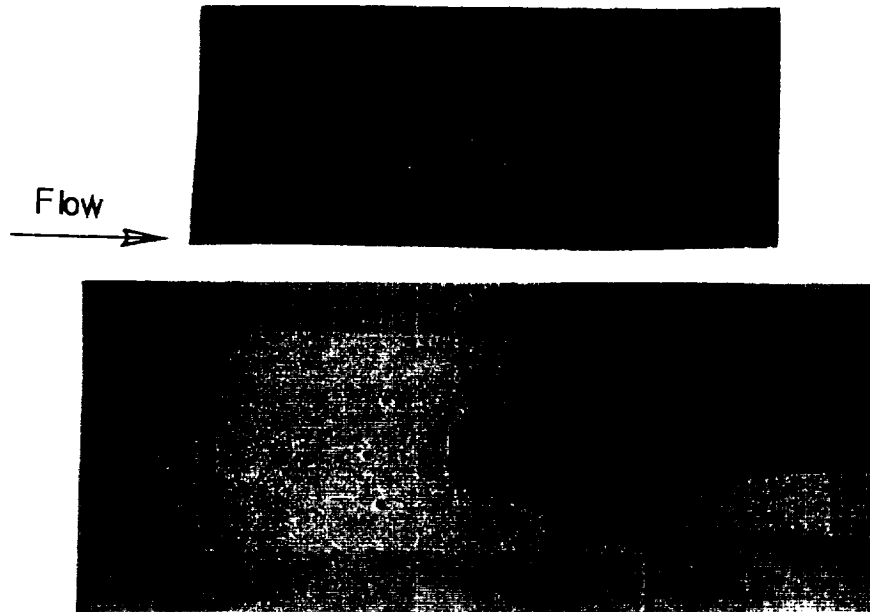


Figure 5.1.6 Surface Flow Pattern with Dye Injected for Surface Flow Visualization, Configuration E, Straight Vertex ( $\theta = 20^\circ$ ,  $\delta = 15^\circ$ )

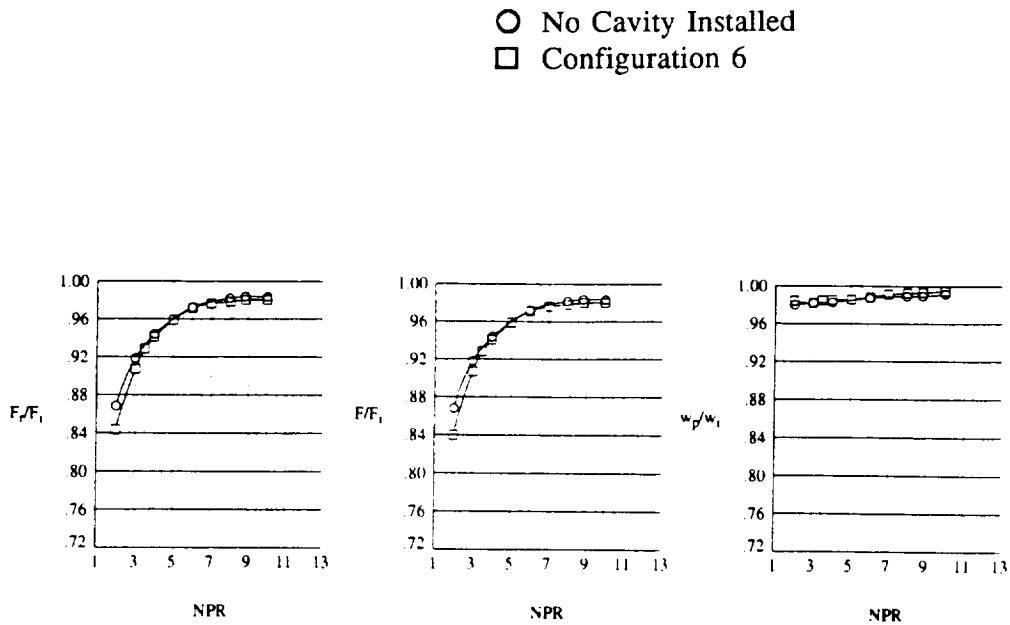


Figure 5.2.1 Performance Data for Configuration 6 ( $\theta=30^\circ$ ,  $\delta=8^\circ$ )

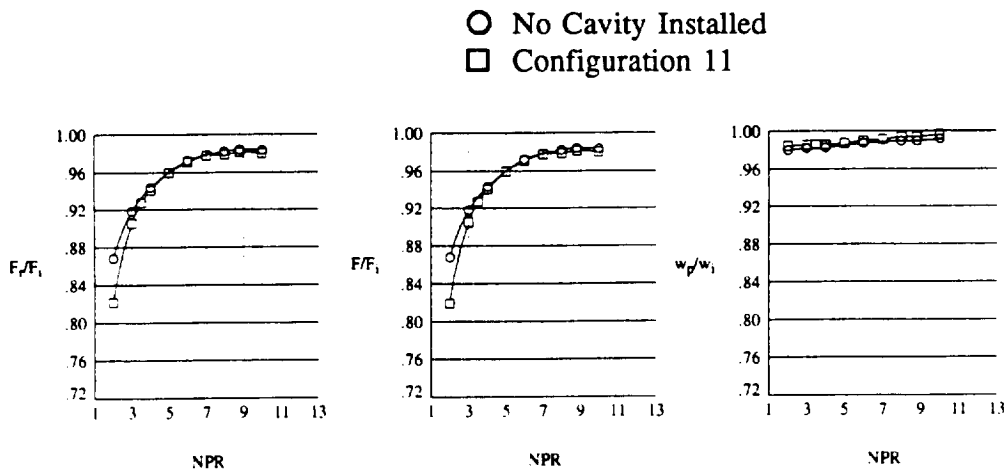


Figure 5.2.2 Performance Data for Configuration 11 (2 cavities,  $\theta=20^\circ$ ,  $\delta=8^\circ$ )

○ No Cavity Installed  
 □ Configuration 21

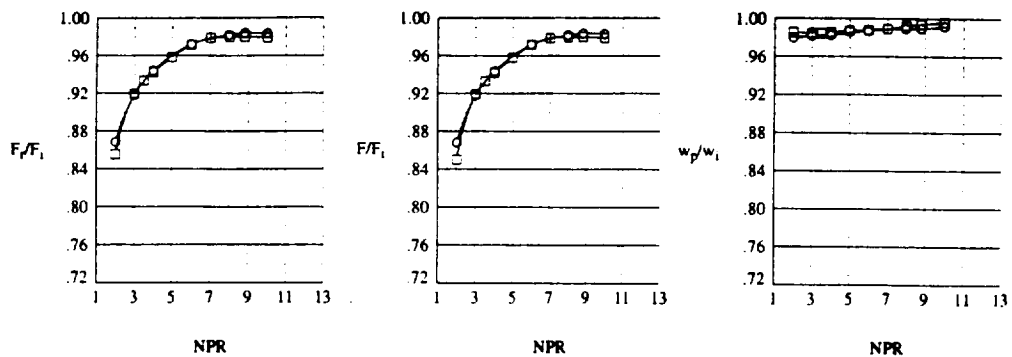


Figure 5.2.3 Performance Data for Configuration 21 (16 cavities,  $\theta=20^\circ$ ,  $\delta=8^\circ$ )

○ No Cavity Installed  
 □ Configuration 22

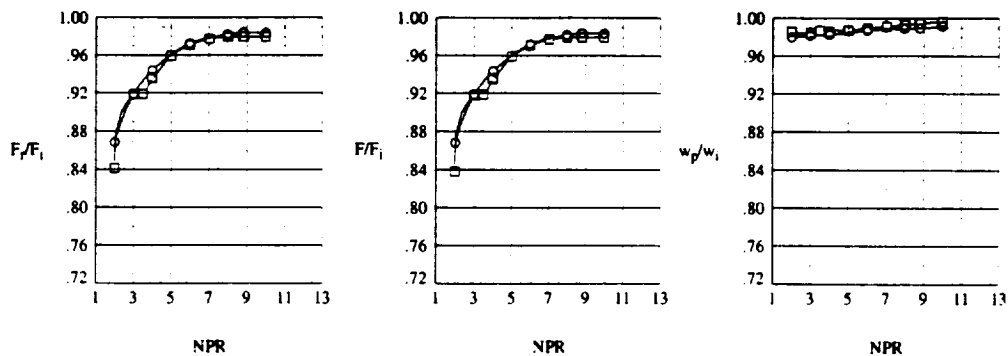


Figure 5.2.4 Performance Data for Configuration 22 (31 cavities,  $\theta=20^\circ$ ,  $\delta=8^\circ$ )

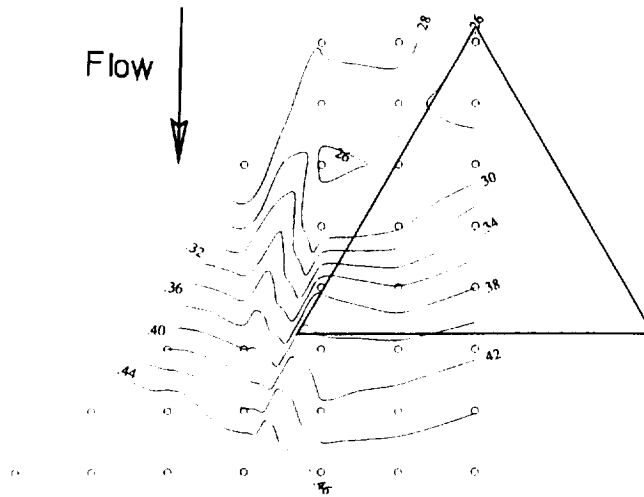


Figure 5.2.5 ESP Pressure Contour for NPR=2.0, Configuration 6 ( $\theta=30^\circ$ ,  $\delta=8^\circ$ )

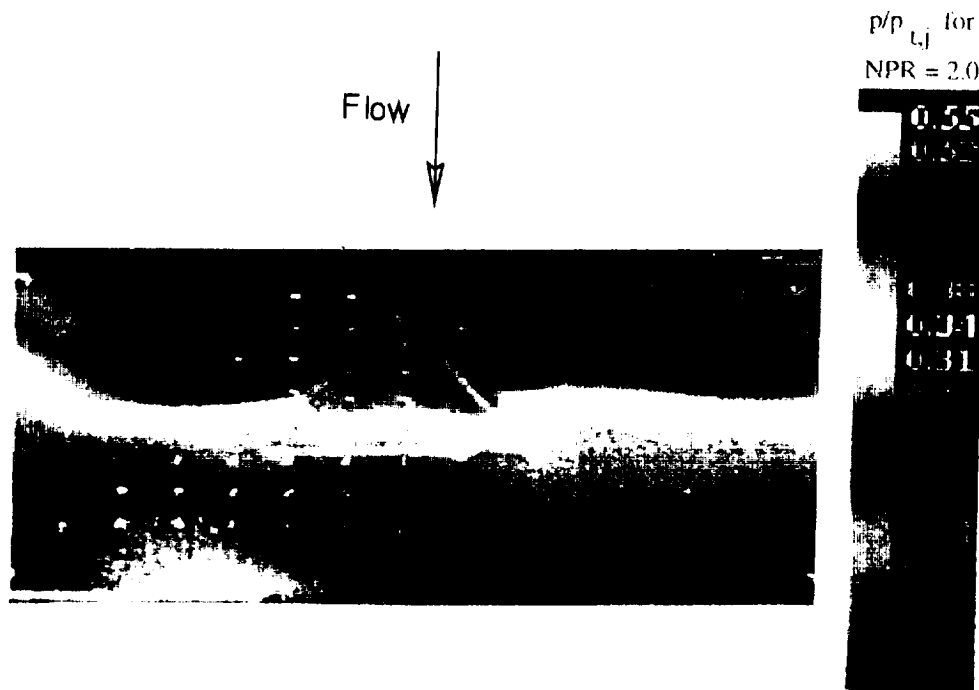


Figure 5.2.6 PSP Pressure Contour for NPR=2.0, Configuration 6 ( $\theta=30^\circ$ ,  $\delta=8^\circ$ )

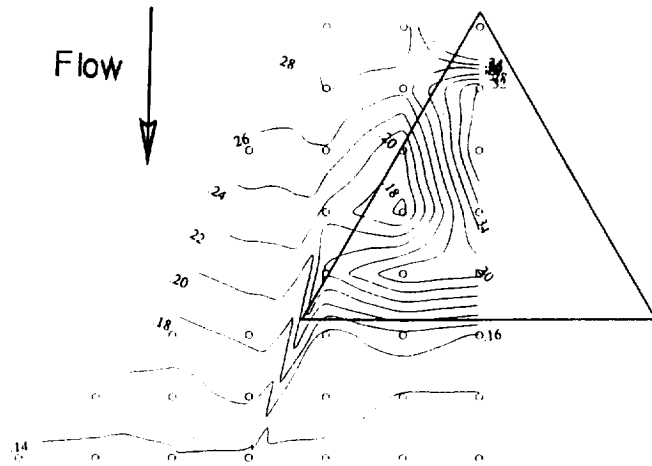


Figure 5.2.7 ESP Pressure Contour for NPR=8.8, Configuration 6 ( $\theta=30^\circ$ ,  $\delta=8^\circ$ )

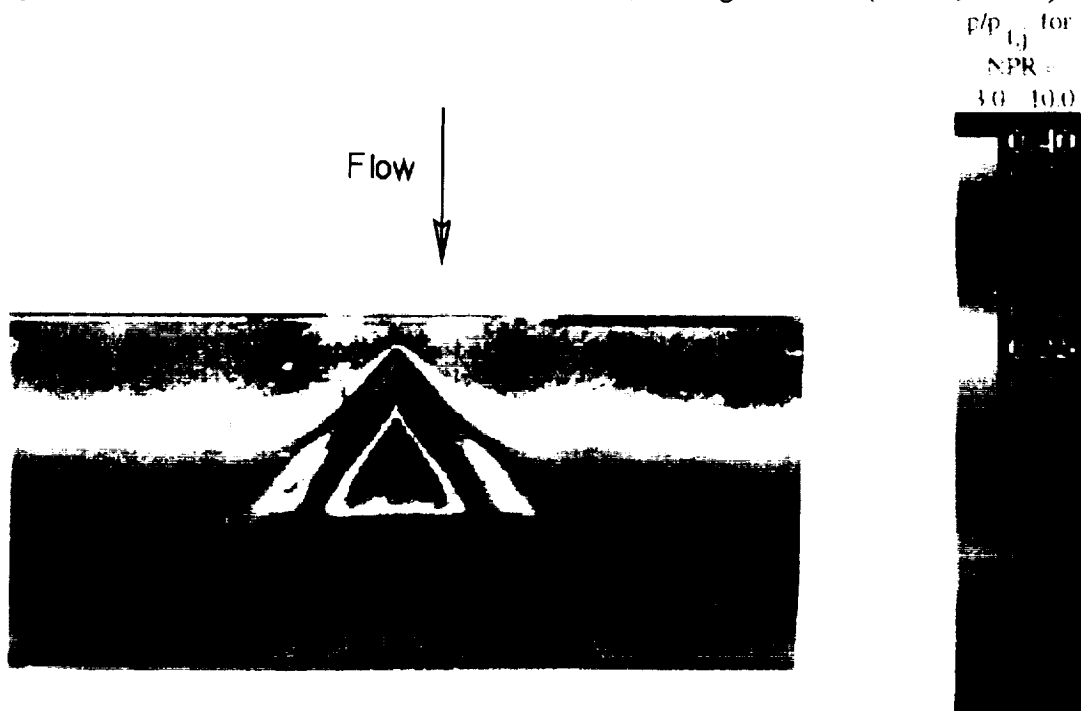


Figure 5.2.8 PSP Pressure Contour for NPR=8.8, Configuration 6 ( $\theta=30^\circ$ ,  $\delta=8^\circ$ )

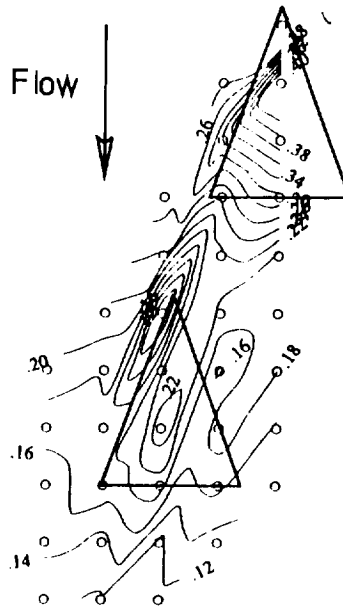


Figure 5.2.9 ESP Pressure Contour for NPR=8.8, Configuration 13  
(2 cavities,  $\theta=20^\circ$ ,  $\delta=8^\circ$ )

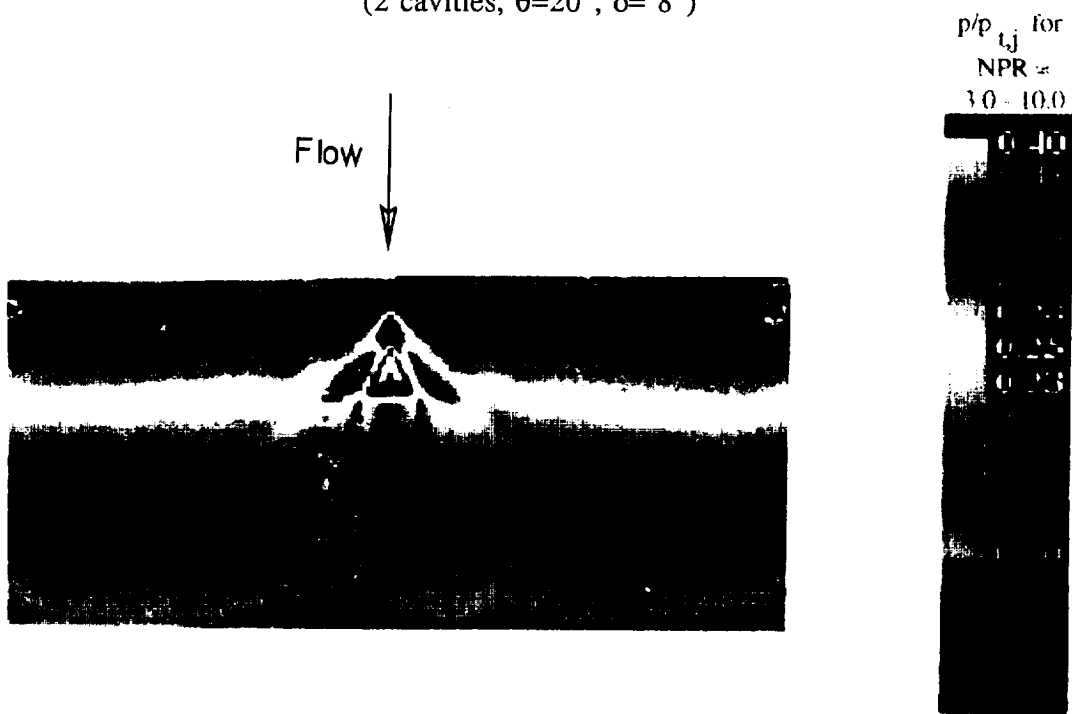


Figure 5.2.10 PSP Pressure Contour for NPR=8.8, Configuration 13  
(2 cavities,  $\theta=20^\circ$ ,  $\delta=8^\circ$ )

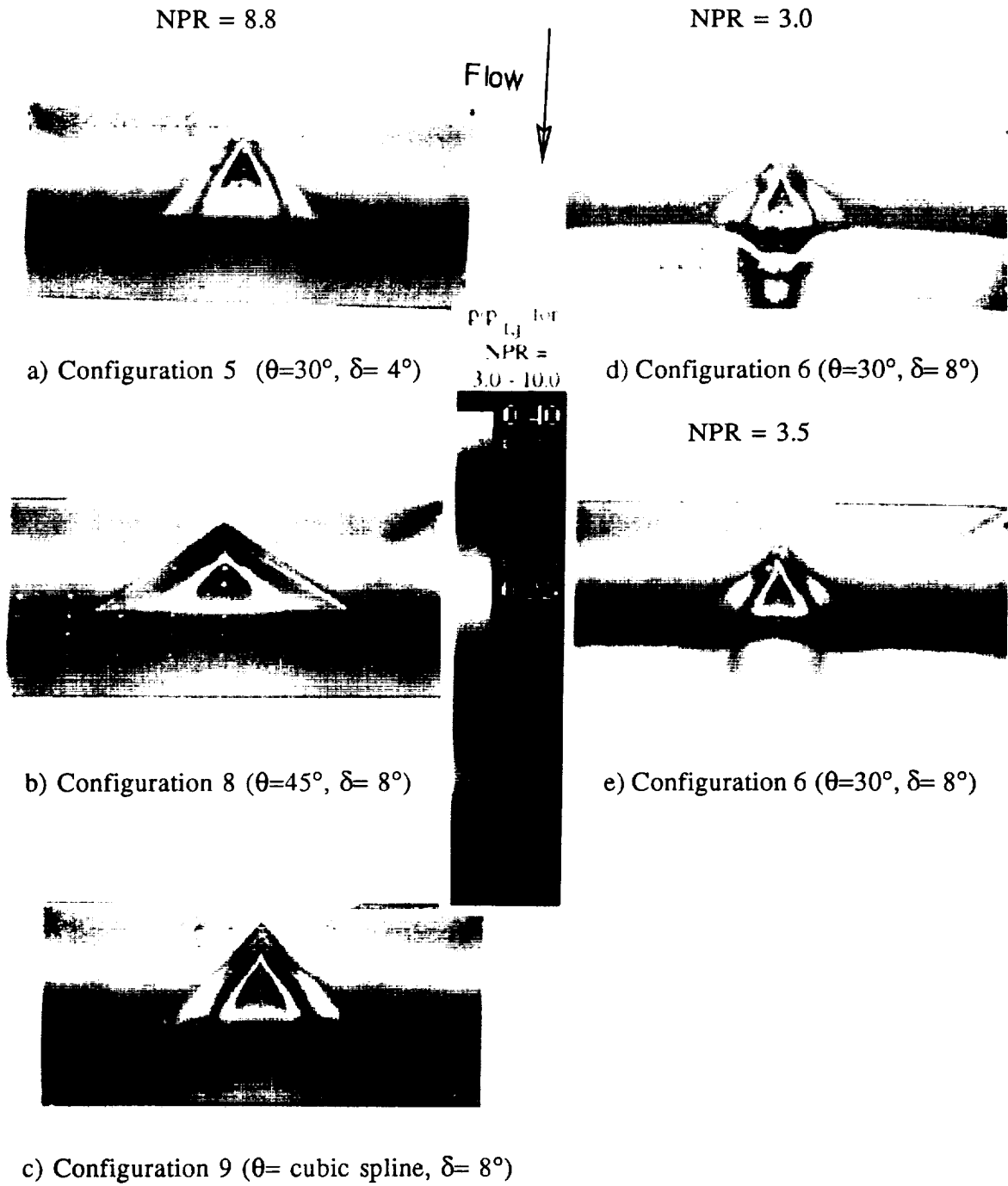


Figure 5.2.11 PSP Pressure Contour for Various NPRs and Configurations

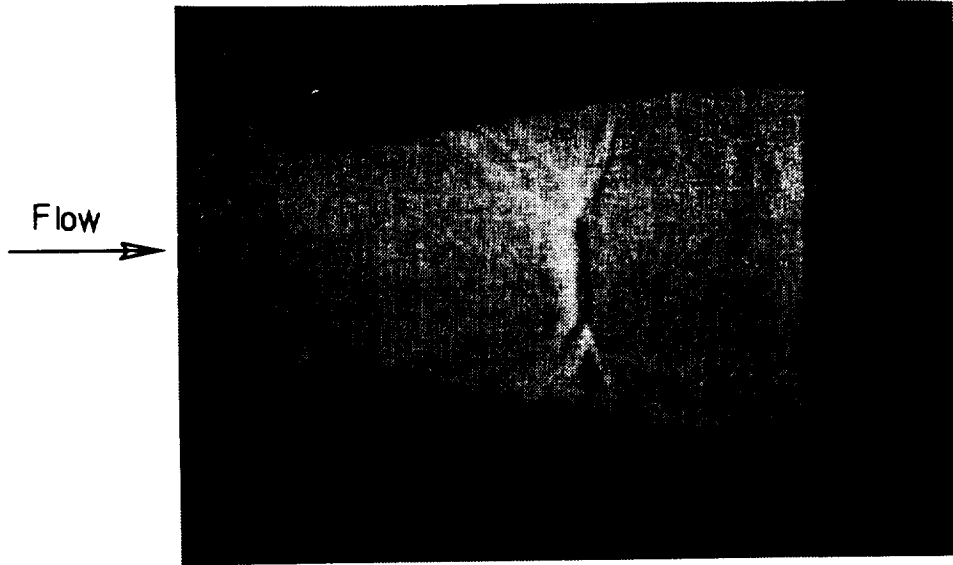


Figure 5.2.12 Focusing Schlieren of Configuration 1 Installed on Lower Ramp,  
NPR = 2.0 ( $\theta = 15^\circ$ ,  $\delta = 4^\circ$ )

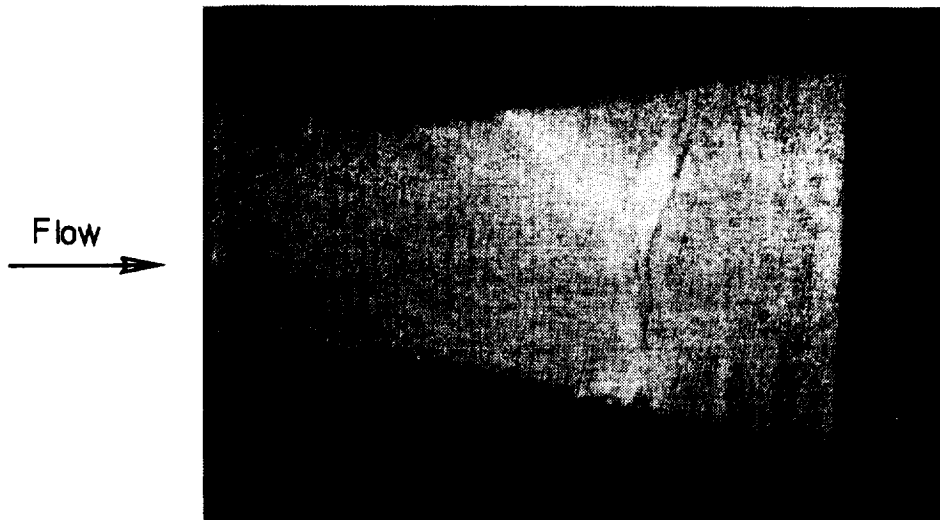


Figure 5.2.13 Focusing Schlieren of Configuration 6 Installed on Lower Ramp,  
NPR = 2.0 ( $\theta = 30^\circ$ ,  $\delta = 8^\circ$ )

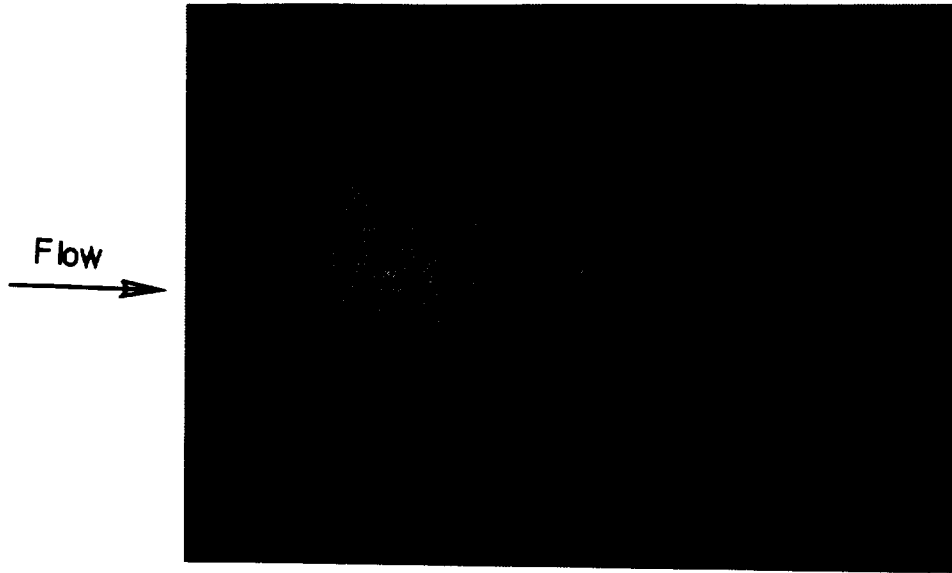


Figure 5.2.14 Focusing Schlieren of Configuration 6 Installed on Lower Ramp, NPR = 8.8 ( $\theta = 20^\circ$ ,  $\delta = 8^\circ$ )

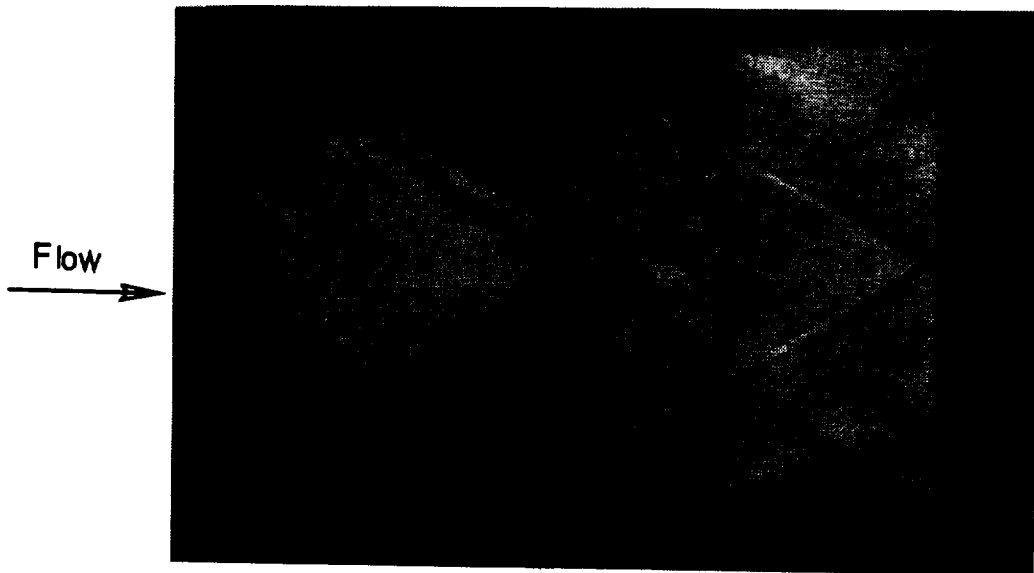


Figure 5.2.15 Focusing Schlieren of Configuration 6 Installed on Both the Upper and Lower Surfaces, NPR = 8.8 ( $\theta = 20^\circ$ ,  $\delta = 8^\circ$ )

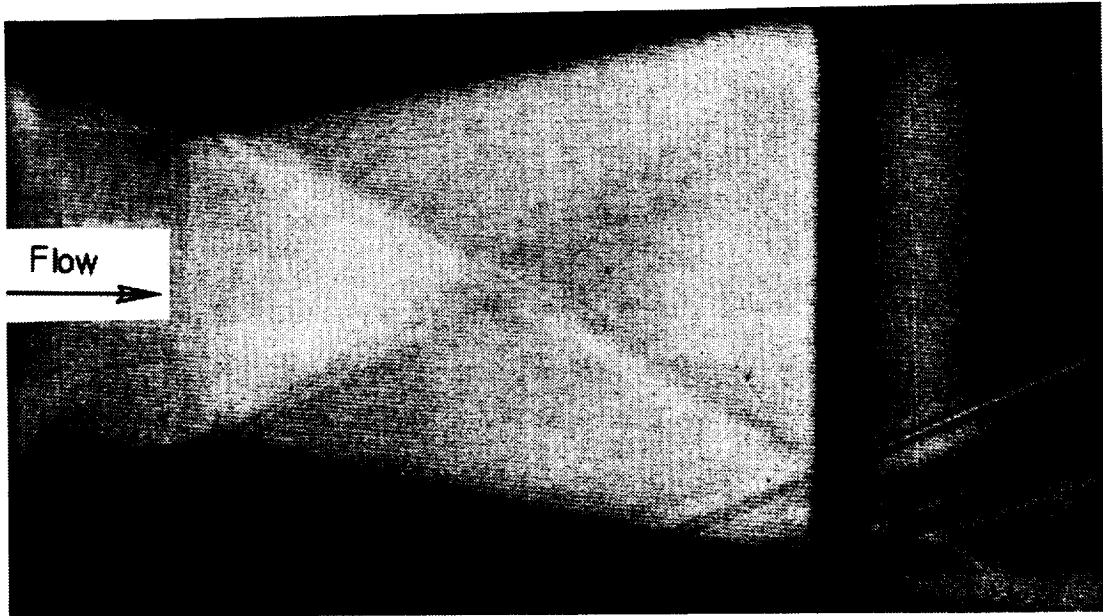


Figure 5.2.16 Focusing Schlieren of Configuration 22 Installed on Lower Surface,  
NPR = 8.8 (31 cavities,  $\theta = 20^\circ$ ,  $\delta = 8^\circ$ )

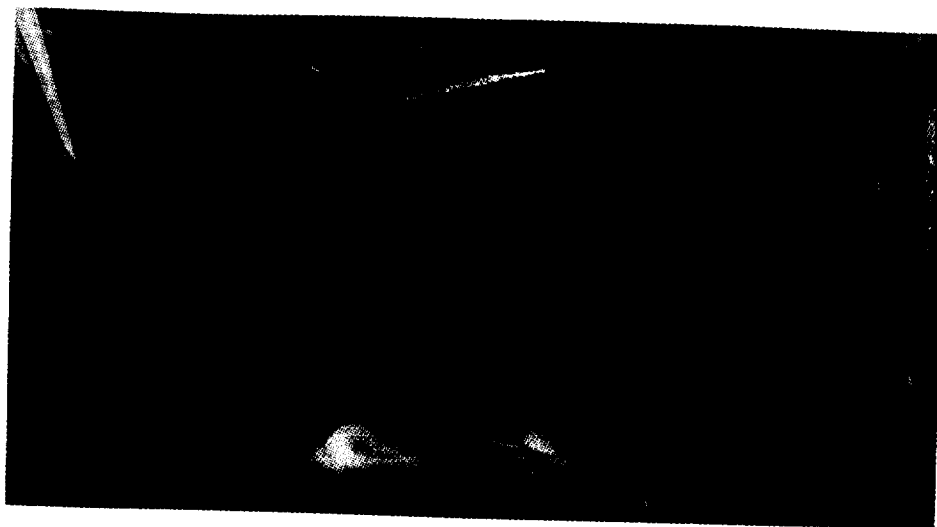


Figure 5.2.17 Laser Light Sheet Picture Showing the Development of Streamwise Vortices for Configuration 6, NPR = 8.8 ( $\theta = 30^\circ$ ,  $\delta = 8^\circ$ )

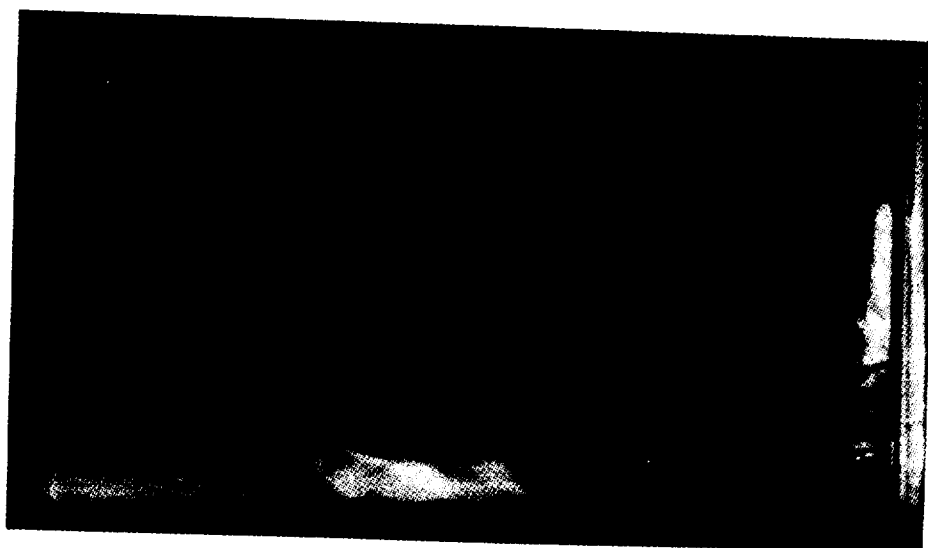


Figure 5.2.18 Laser Light Sheet Picture Showing the Interaction of Four Vortices for Configuration 13, NPR = 8.8 (2 cavities,  $\theta = 20^\circ$ ,  $\delta = 8^\circ$ )



Figure 5.2.19 Water Tunnel Dye Injection Showing the Development of Vortices for Configuration 5 ( $\theta=30^\circ$ ,  $\delta=4^\circ$ )



Figure 5.2.20 Laser Light Sheet Visualization of Vortices Developed in Water Tunnel, Configuration 5 ( $\theta = 20^\circ$ ,  $\delta = 8^\circ$ )

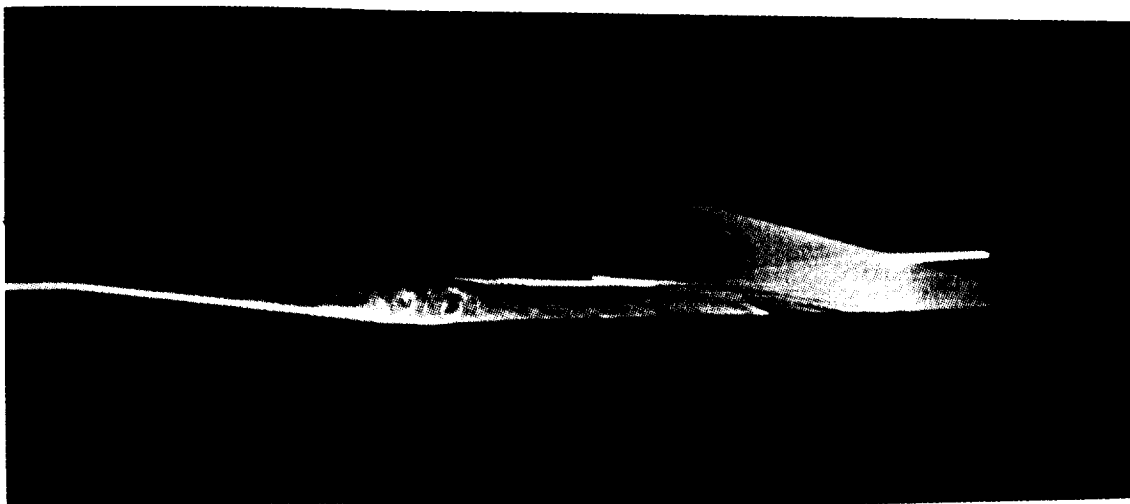


Figure 5.2.21 Laser Light Sheet Picture of the Streamwise Development of Vortex for Configuration 5 in the Water Tunnel ( $\theta = 30^\circ$ ,  $\delta = 4^\circ$ )

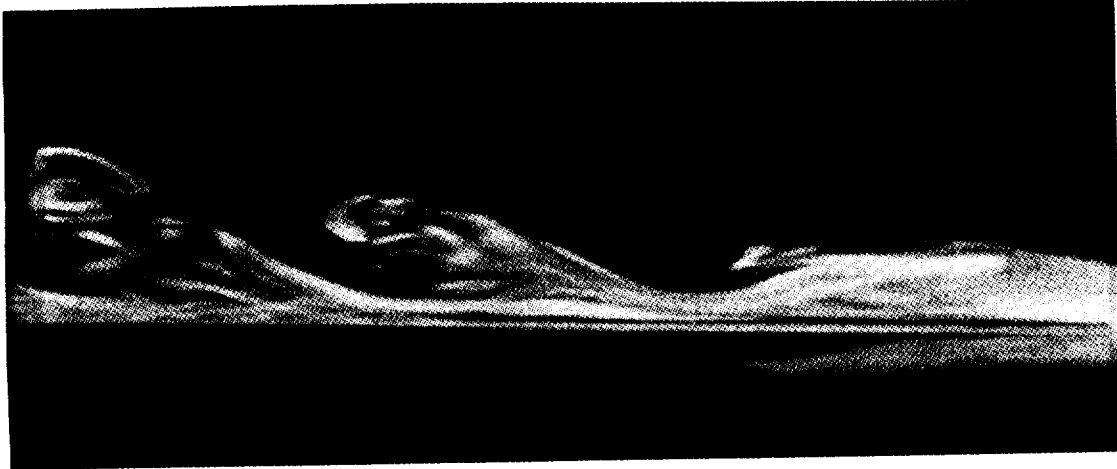


Figure 5.2.22 Laser Light Sheet of Streamwise Development of the Shear Layer Produced by Installing the Cavity Backwards in Water Tunnel Flow

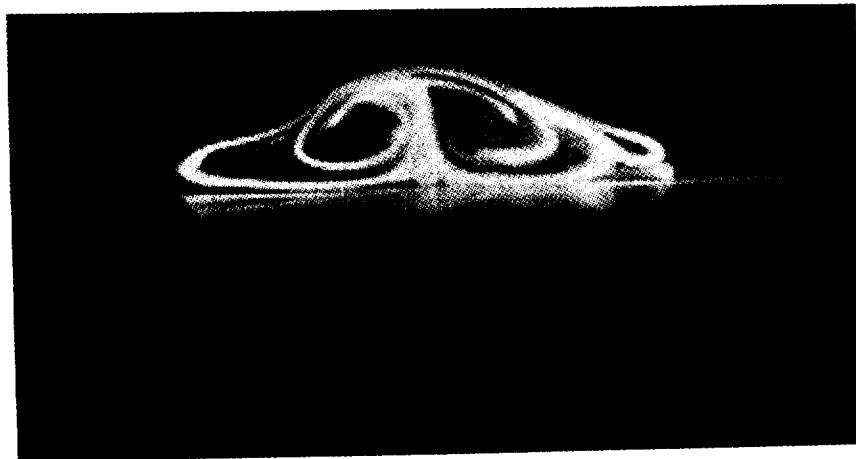


Figure 5.2.23 Laser Light Sheet of Crossflow Development of the Shear Layer Produced by Installing the Cavity Backwards in Water Tunnel Flow



**Figure 5.3.1** Static Pressure Within the Cavity, Flat Plate Flow Conditions, Mach 2.0, Configuration 1 ( $\theta=10^\circ$ ,  $\delta=4^\circ$ )

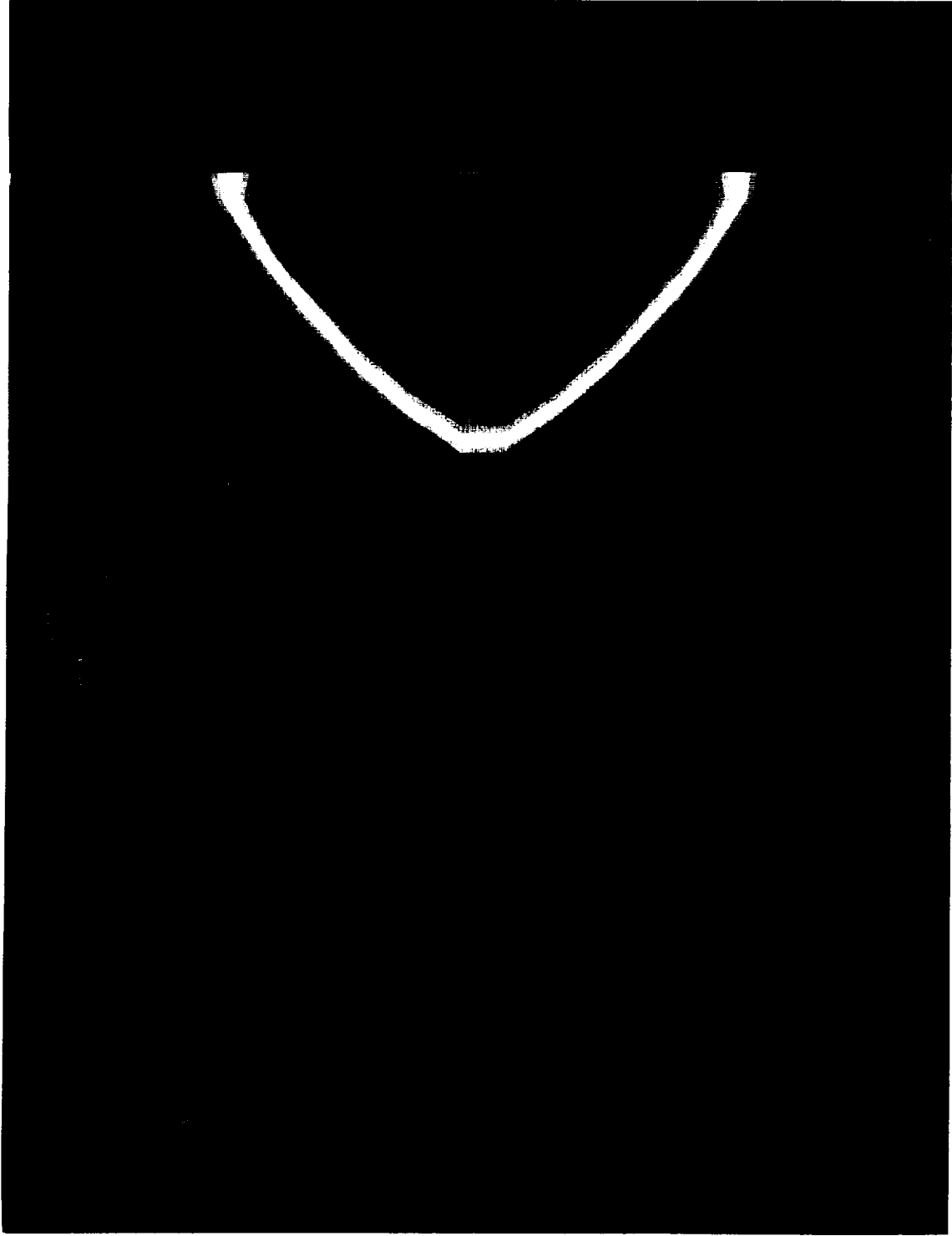


Figure 5.3.2 Static Pressure Within the Cavity, Flat Plate Conditions, Mach 2.0, Configuration 6 ( $\theta=30^\circ$ ,  $\delta=8^\circ$ )

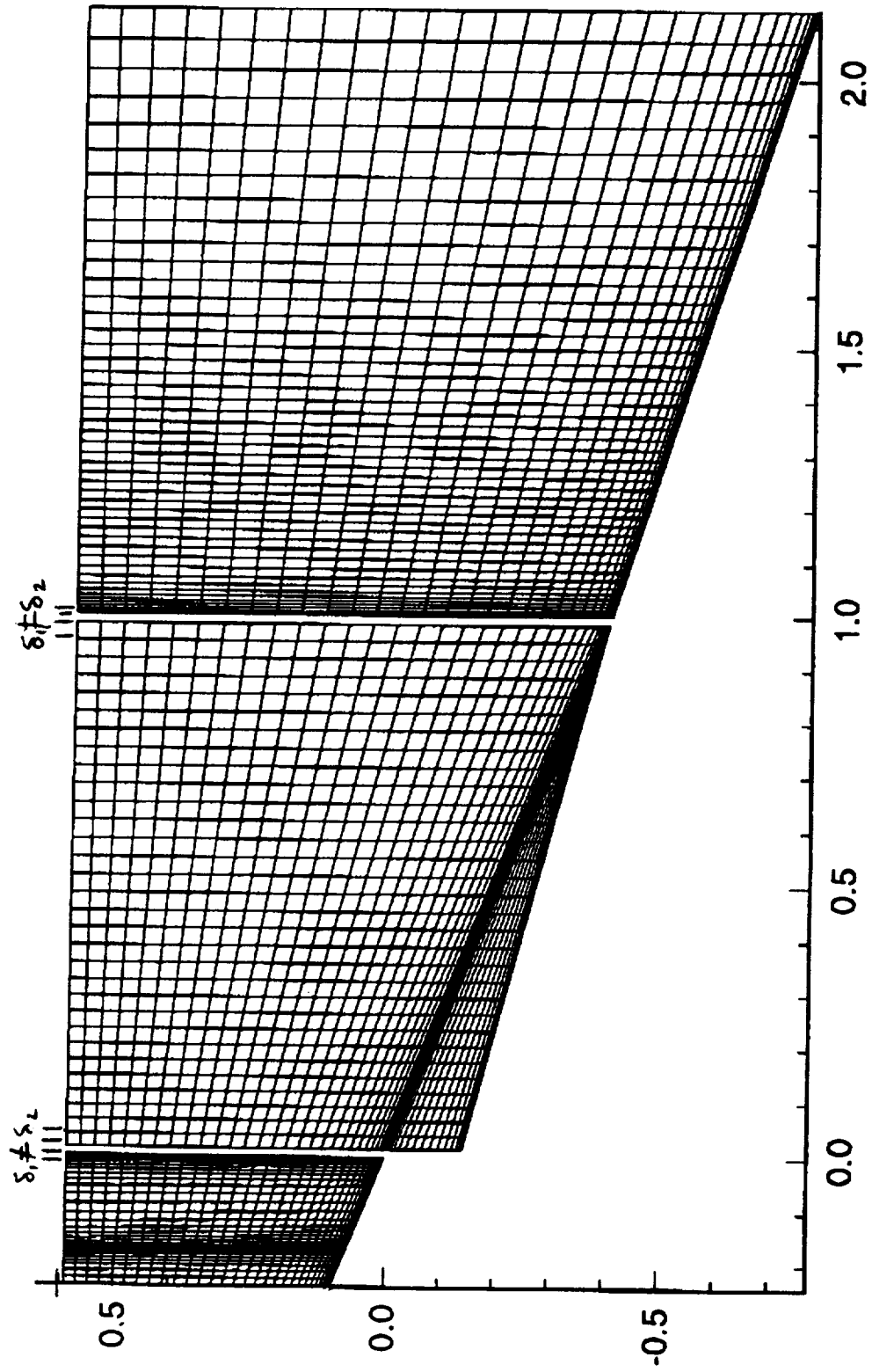


Figure 5.3.3 Oblique View of Nozzle Grid with Matching Problems Highlighted



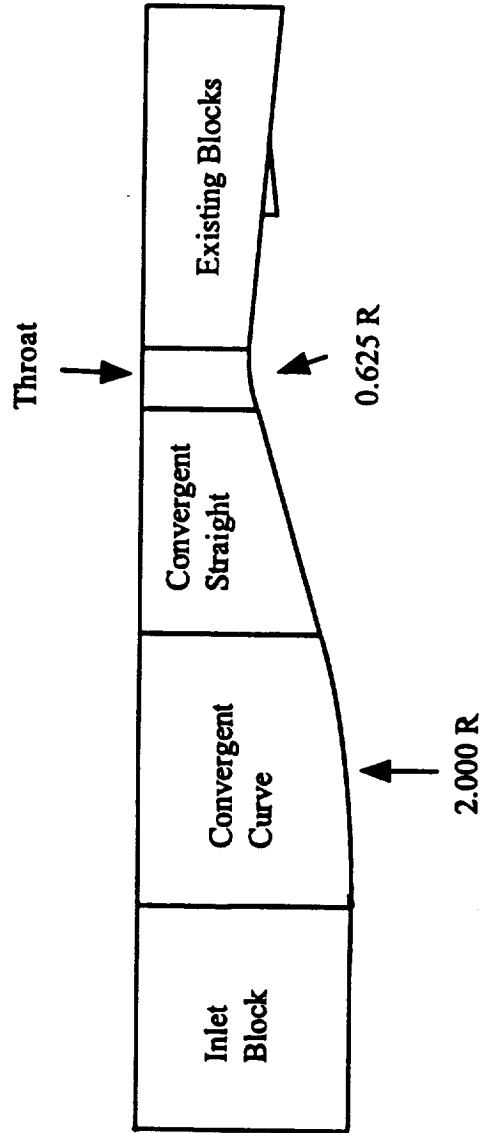


Figure 5.3.5 Schematic of Suggested Grid/Block Definitions for Nozzle Flow Solver

## **6.0 CONCLUSIONS AND RECOMMENDATIONS**

Extensive testing was performed on a supersonic vortex generator at the University of Kansas and at NASA Langley Research Center. The shaped cavity generated a pair of counter-rotating streamwise vortices with little additional losses.

### **6.1 Conclusions**

The results from experiments at the University of Kansas clearly showed that the shaped cavity placed in supersonic flow would generate streamwise vortices. Additional tests at NASA Langley proved that these vortices can be produced with little additional loss.

Based on the performance data, the losses associated with the use of this type of shaped cavity at design NPR were small, within the accuracy of the instrumentation used. This would seem to indicate that the vortices were being generated with weak compression and expansion Mach waves. At lower NPR, the losses are greater, due in part to the vortices delaying separation, thereby allowing for greater expansion of the supersonic flow.

Pressure sensitive paint experiments verified the path of the vortex and allowed for some investigation of vortex interactions. The PSP results also showed the effects of the cavity on the shock structure of an underexpanded nozzle. With the presence of the VG, the flow is allowed to expand further downstream, to pressures further below atmospheric. This expansion delays the shock induced separation. This in turn causes a decrease in the performance because the pressure is reduced on the forward-facing step. However, there are instances where separation control is advantageous, for example on a wing that is about to stall at supersonic conditions or in C-D nozzles for thrust vectoring applications.

The use of pressure sensitive paint in a relatively high pressure environment has been validated. When the PSP pressures were compared to ESP data, the results agreed within, approximately, 3.5% for all NPRs. Since the PSP data provided a much clearer picture of the overall flow field than did the pressure taps.

The flat plate CFD results listed above were originally believed to be accurate, converged representations of the physical flow, however, after the inability of the expanding flow solver to

converge to a physical solution, the results obtained for the flat plate are thrown into doubt. The following conclusions can be made about the attempts to obtain a numerical solution to the supersonic flow through a shaped cavity.

- \* The use of the AXB grid generator, while originally considered acceptable, may not be adequate for providing a grid that can accurately capture the path of the vortices.
- \* The PAB3D code provided great flexibility in solution methods. This code has been used to solve similar nozzle problems in the past and, with the support of NASA Langley engineers, should be able to solve the SSVG problem.
- \* The flat plate solutions did converge. However, due to errors in the nozzle solution, these results are not considered valid without verification using a code and grid generator that can accurately solve the expanding flow problem.

## **6.2 Recommendations**

While the experiments documented in this report represent a considerable amount of information, there are several areas that require further investigation.

Detailed flow field analysis of the cavity should be performed. Computational fluid dynamics techniques should be used to verify the experimental data. When adequate CFD validation has been performed, greater design flexibility will be possible. Since the CFD results can be validated using the experimental data detailed here, the CFD code could then be used as a design tool, tailoring cavity shapes to specific flow fields without the need for extensive experimental testing.

The design and testing of a smart version of the vortex generator is another area of future research. While the investigation performed here indicates that flow separation can be delayed by the presence of a cavity in the flow, the ability to reattach separated flow should be investigated. In order to perform this type of testing a nozzle with variable geometry and a smart version of the VG must be developed.

Since the primary focus of this investigation was on nozzle flow, additional investigations in other types of flow fields such as SCRAMjet flow, turbomachinery blading and exterior supersonic flow.

The use of the AXB grid generator and the PAB3D flow solver were used to attempt to solve the complex flow patterns created by a cavity vortex generator in supersonic flow. Unfortunately, the grid was not adequate for providing converged solutions. The following recommendations are suggested for correcting the problems discovered.

- \* The grid matching between the existing blocks must be smoothed out further. The means to do this are provided in reference 4 and involve changing parameters in the `ssvg.dsg` file, a copy of which may be found in appendix C.
- \* The boundary layer expansion for the boundary layers at the cavity edge and the boundary layers used to capture the vortex must be modified. In all cases, the grid expands too fast. A combination of additional grid points, more grid points located within the boundary layer and a thicker boundary layer must be employed.
- \* The location of the boundary layers used to capture the vortex path must be revised to ensure that the true vortex path, determined from experiments, is captured in the boundary layers.
- \* Consider the use of other grid generating schemes. Specifically, the use of adaptive grids. The use of adaptive grids might provide an easier method of vortex capture. The PAB3D code could be modified to allow the use of such a grid generator.
- \* Modify the inflow grid blocks. The original grid design did not allow adequate time for the upstream flow to develop fully. The suggested block modifications are shown in figure 5.3.5.

## **7.0 REFERENCES**

1. Farokhi, S.; Taghavi, R., "Supersonic Vortex Generator", Patent Pending, Applied Dec 15, 1994; Application Number 08/356,646.
2. Wheeler, G., "Means of Maintaining Attached Flow of a Flowing Medium", US Patent No. 4,455,045. Filed Oct 26, 1981, Issued Jun 19, 1984.
3. Crocco, L., "Eine neue Stromfunktion fur die Erforschung der Bewegung der Gase mit Rotation", Math. Mech. v 17, New York, 1937.
4. Pao, S., Axisymmetric and Rectangular Grid Generation Package "AXB", Propulsion Aerodynamics Branch, NASA Langley, Hampton, VA, 1992.
5. Hamid, K.; Carlson, J.; Pao, S., "Computational Analysis of Vented Supersonic Exhaust Nozzles Using a Multiblock/Multizone Strategy", AIAA 81-0125, Conference Proceedings, 29th Aerospace Sciences Meeting, Reno, NV, Jan 7-10, 1991.
6. Carlson, J., "Prediction of Internal Performance for Two-Dimensional Convergent-Divergent Nozzles", AIAA 91-2369, Conference Proceedings, AIAA/SAE/ASME/ASEE 27th Joint Propulsion Conference, Sacramento, CA, June 24-27, 1991.
7. Hamid, K., and Others, "Commercial Turbofan Engine Exhaust Nozzle Flow Analysis Using PAB3D", AIAA 92-2701, Conference Proceedings, 10th Applied Aerodynamics Conference, Palo Alto, CA, June 22-24, 1992.
8. DiMicco, R.; Disimile, P., "A New Look at Surface Flow Visualization to Provide Insight into Complex Fluid Dynamic Behavior," Conference Proceedings, International Congress on Instrumentation in Aerospace Simulation Facilities, Published by IEEE, pp 43-48.
9. Staff of the Propulsion Aerodynamics Branch, A User's Guide to the Langley 16-Foot Transonic Tunnel Complex, Rev. 1, NASA Technical Memorandum, NASA-TM-102750, NASA Langley Research Center, Hampton VA, 1990.
10. Hunter, C., An Experimental Analysis of Passive Shock-Boundary Layer Interaction Control for Improving the Off-Design Performanced of Jet Exhaust Nozzles, M.S. Thesis, George Washington University, 1993.

11. Mercer, C.; Berrier, B.; Capone, F.; Grayston, A., Data Reduction Formulas for the 16-Foot Transonic Tunnel NASA Langley Research Center, NASA Technical Memorandum, NASA-TM-107646, NASA Langley Research Center, Hampton VA, 1992.
12. Blumenthal, P.; Helland, S., "Improved Pressure Measured System for Calibration of the NASA LeRC 10 x 10 Supersonic Wind Tunnel", Conference Proceedings of the International Symposium, Instrument Society of America, pp 647-660, 1994.
13. Peterson, J.; Fitzgerald, V., "New Technique of Surface Flow Visualization Based on Oxygen Quenching of Fluorescence", Review of Scientific Instruments v 51 n 5, pp 670-671, 1980.
14. Morris, M.; Donovan, J.; Kegelman, J.; Schwab, S.; Levy, R.; Crites, R., "Aerodynamic Applications of Pressure Sensitive Paint", Conference Proceedings of the 30th Aerospace Sciences Meeting and Exhibit, AIAA 92-0264, Jan 1992.
15. Hunter, C., An Overview of the Concepts and Aerodynamic Applications of Pressure Sensitive Paint, JIAFS Report, NASA Langley Research Center, Hampton VA, Apr 1992.
16. Morris, M.; Benne, M.; Crites, R.; Donovan, J., "Aerodynamic Measurements based on Photoluminescence", AIAA Paper 93-0175, Jan 1993.
17. Sajban, M., "Uncertainty Estimates for Pressure Sensitive Paint Measurements", AIAA Journal v 31 n 11, pp 2105-2110, Nov 1993.
18. Weinstein, L., "An Improved Large-Field Focusing Schlieren System", AIAA Publication, AIAA 91-0567, 1991.
19. Pendergraft, O.; Neuhart, D.; Kariya, T., A User's Guide to the Langley 16- by 24-Inch Water Tunnel, NASA Technical Memorandum, NASA-TM-104200, NASA Langley Research Center, Hampton VA, 1992.
20. Jagharghi, A.; Cler, D.; Erickson, G.; Mitchell, M.; Lamb, M.; Gibson, L.; Farokhi, S.; Taghavi, R.; Hazlewood, R., "Application of Pressure Sensitive Paint to Measurement of Global Surface Pressure for a Convergent-Divergent Nozzle and an Isolated Double Delta Wing at Transonic Speeds", Conference Proceedings 33rd AIAA Aerospace Sciences Meeting, AIAA 95-0639, Jan 1995.



**APPENDIX A      University of Kansas Flow Visualization Pictures**

**This Appendix tabulates additional flow visualization pictures taken at the University of Kansas as a proof-of-concept investigation of the effects of a shaped cavity in supersonic flow.**

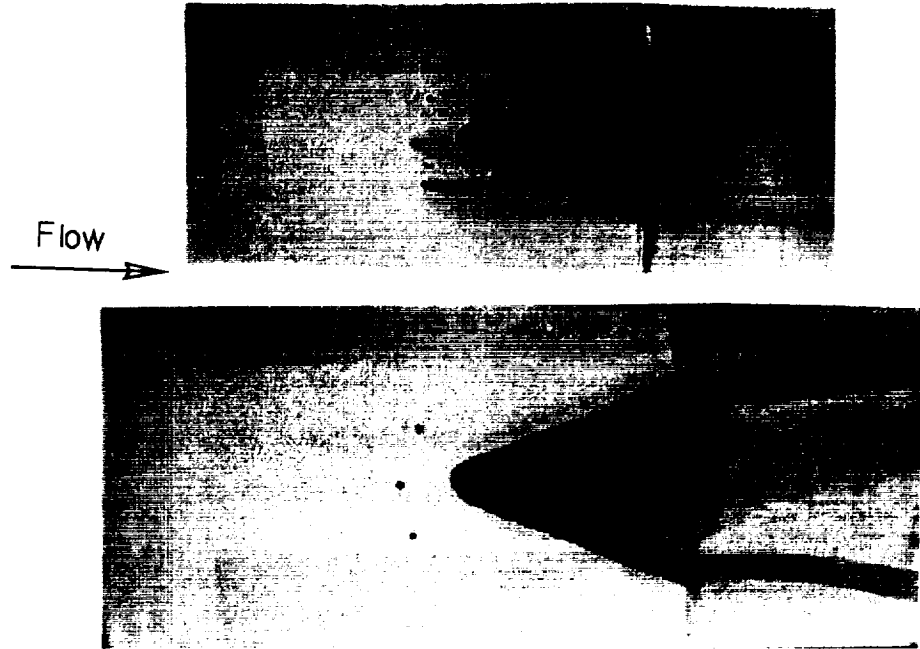


Figure A.1 Surface Flow Visualization Using Dye Injection, Configuration B, Indented Walls ( $\theta= 20^\circ$ ,  $\delta= 15^\circ$ )

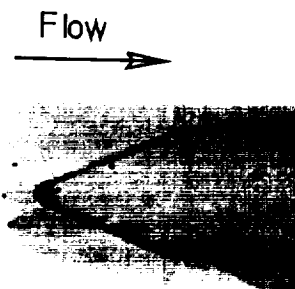


Figure A.2 Surface Flow Visualization with Dye Injection, Configuration C, Straight Walls ( $\theta= 20^\circ$ ,  $\delta= 15^\circ$ )

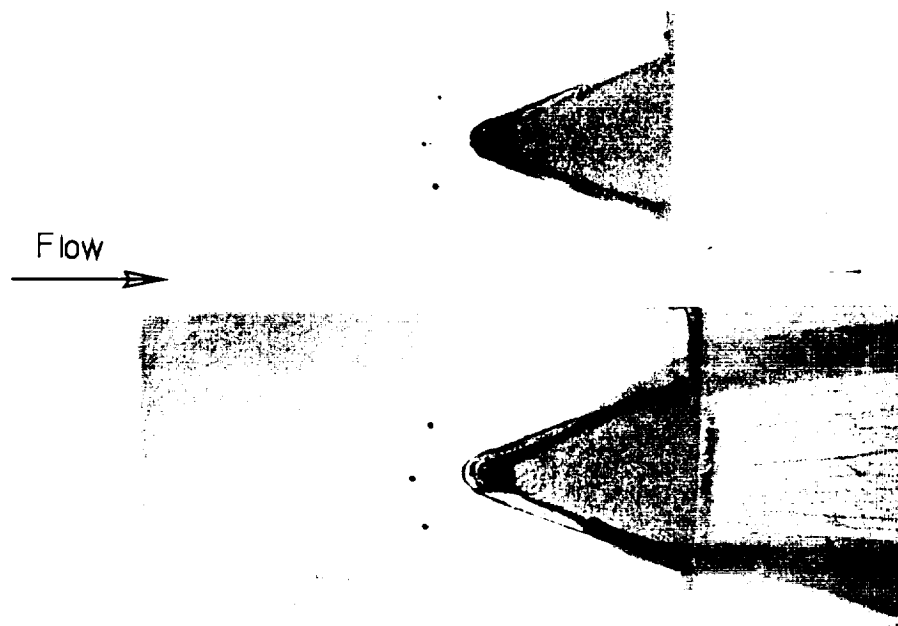


Figure A.3 Surface Flow Visualization with Dye Injected from Lower Ports, Configuration D, Shallow Ramp ( $\theta= 20^\circ$ ,  $\delta= 8^\circ$ )

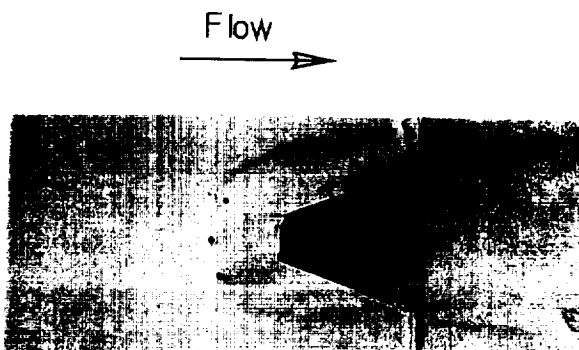


Figure A.4 Surface Flow Visualization with Dye Injected from Lower Ports, Configuration E, Flat Vertex ( $\theta= 20^\circ$ ,  $\delta= 15^\circ$ )



## **APPENDIX B      NASA Langley Experimental Results**

**This Appendix tabulates additional configuration photographs and experimental pictures used in the investigation of the effects of a supersonic vortex generator on divergent nozzle flow.**

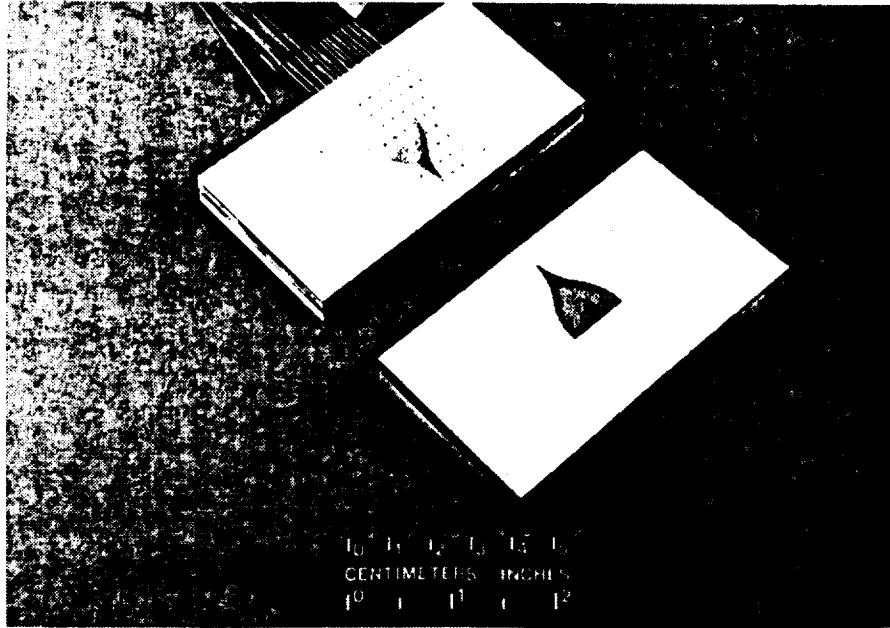


Figure B.1 Photograph of Configuration 9 ( $\theta = \text{cubic spline}$ ,  $\delta = 8^\circ$ )

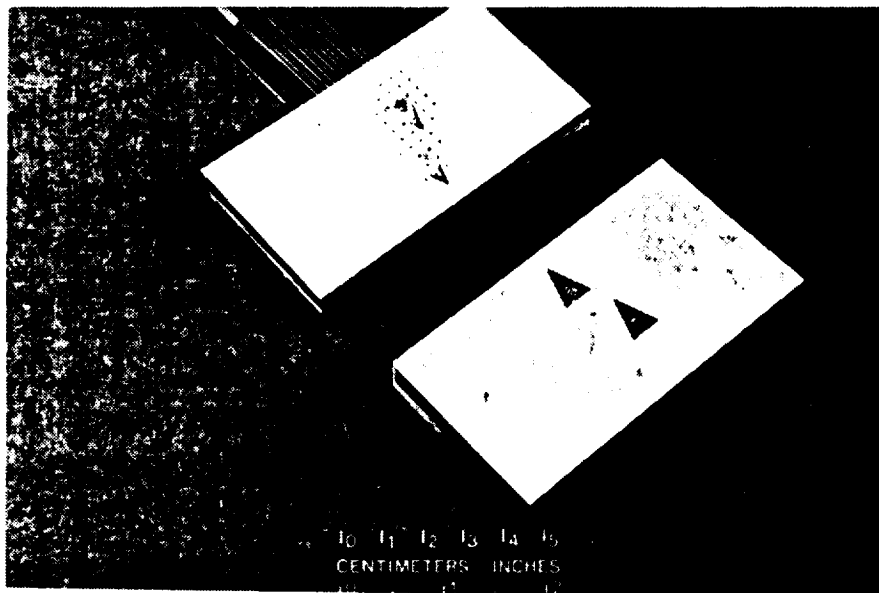
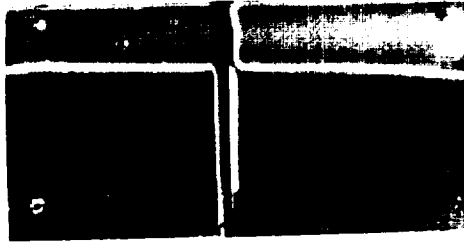


Figure B.2 Photograph of Configuration 13 (2 cavities,  $\theta = 20^\circ$ ,  $\delta = 8^\circ$ )

NPR = 2.0



No Cavity Installed

$p/p_{t,j}$  for  
NPR = 2.0

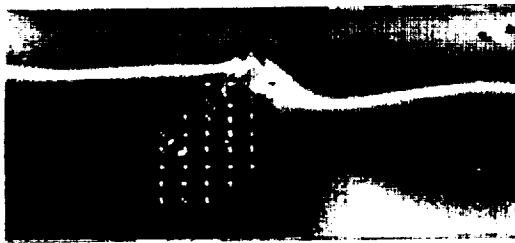


Flow  
↓

NPR = 8.8

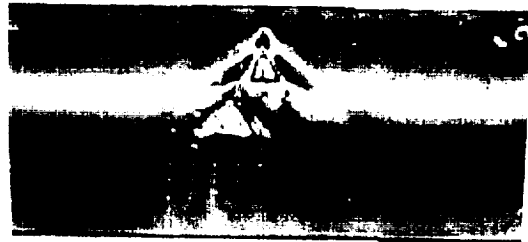


No Cavity Installed



Configuration 12

$p/p_{t,j}$  for  
NPR =  
3.0 - 10.0



Configuration 12



Configuration 13



Configuration 13

Figure B.3 PSP Pictures for Various NPRs and Configurations

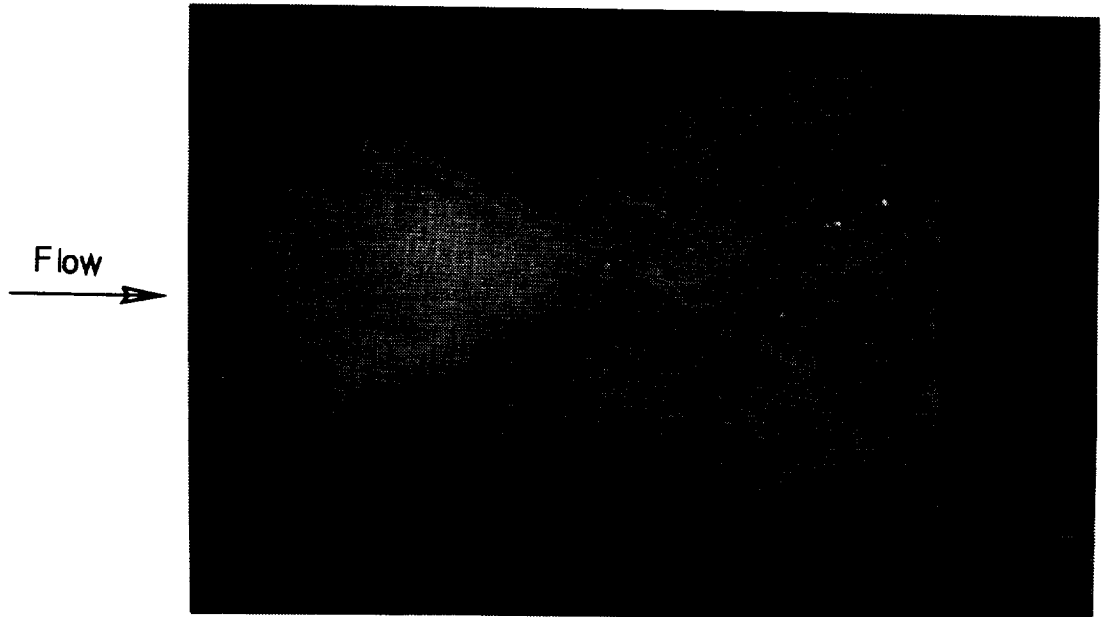


Figure B.4 Focusing Schlieren Photograph of a Shallow Ramp Configuration, Configuration 5, NPR = 8.8 ( $\theta = 30^\circ$ ,  $\delta = 4^\circ$ )

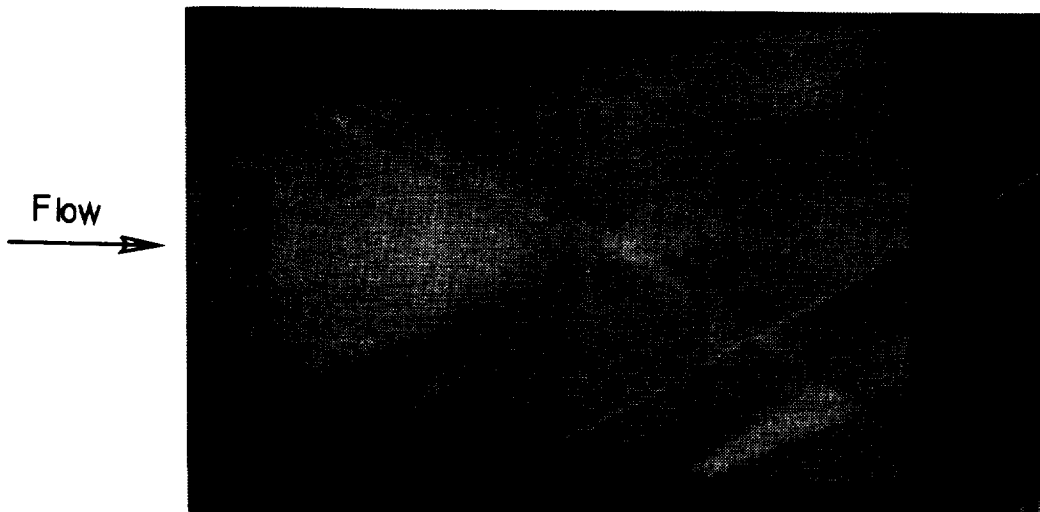


Figure B.5 Focusing Schlieren Photograph of a Supersonic Cavity Lip, Configuration 8, NPR = 8.8 ( $\theta = 45^\circ$ ,  $\delta = 8^\circ$ )

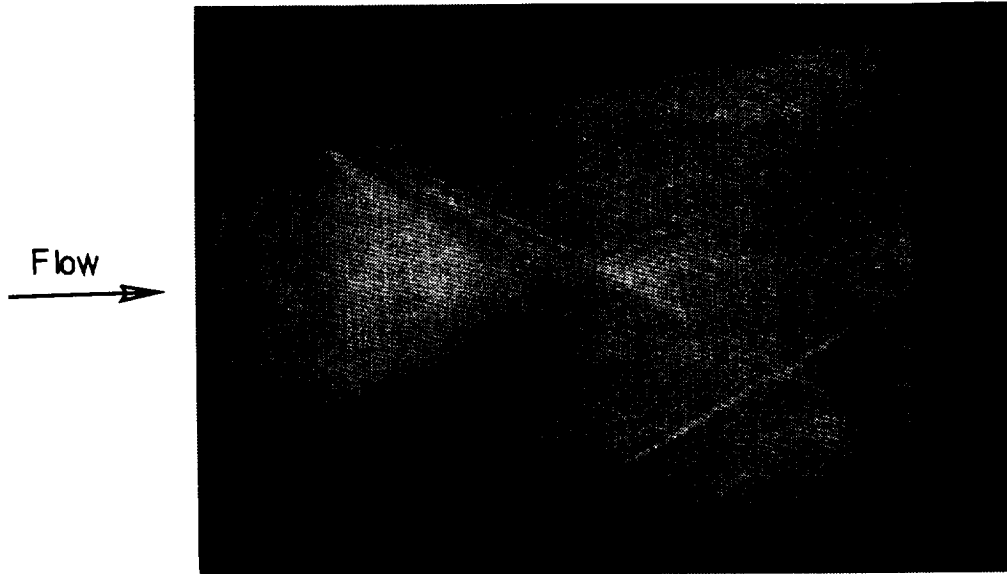


Figure B.6 Focusing Schlieren Photograph of a Cubic Spline Cavity Shape, Configuration 9, NPR = 8.8 ( $\theta = \text{cubic spline}$ ,  $\delta = 8^\circ$ )

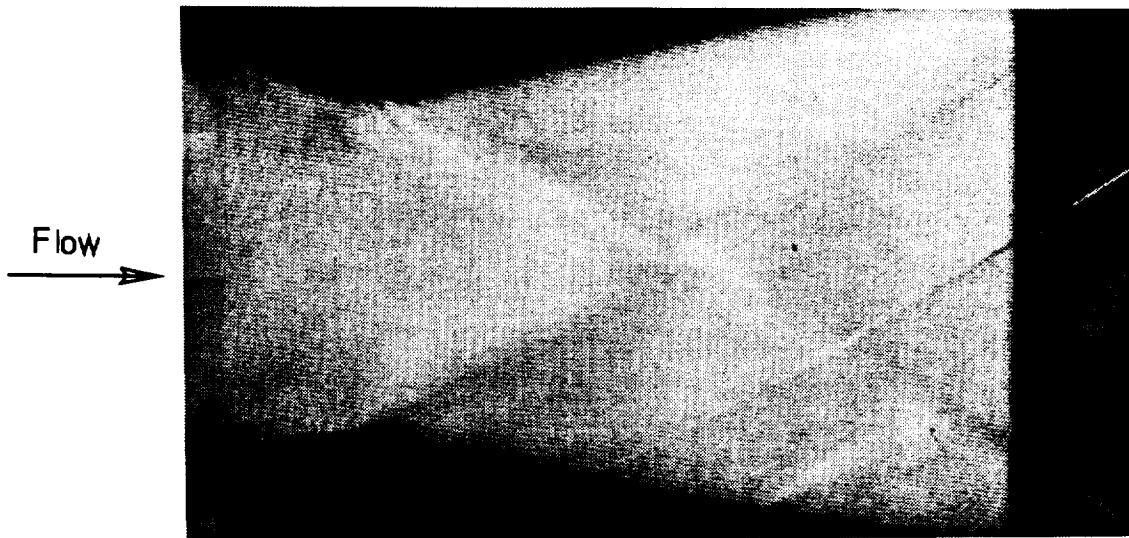


Figure B.7 Focusing Schlieren Photograph of an Underexpanded Nozzle, Configuration 6, NPR = 10.0 ( $\theta = 30^\circ$ ,  $\delta = 8^\circ$ )



Figure B.8 Laser Sheet Flow Visualization of a Cubic Spline Shaped Cavity, Configuration 9, NPR = 8.8 ( $\theta$  = cubic spline,  $\delta = 8^\circ$ )

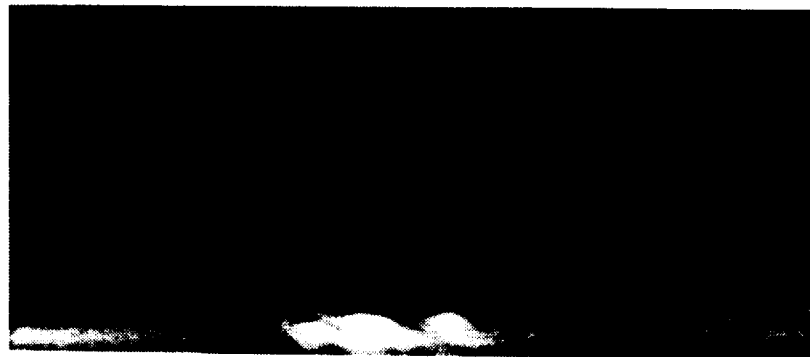


Figure B.9 Laser Sheet Flow Visualization of Vortex Interaction, Configuration 13, NPR = 8.8 (2 cavities,  $\theta = 20^\circ$ ,  $\delta = 8^\circ$ )

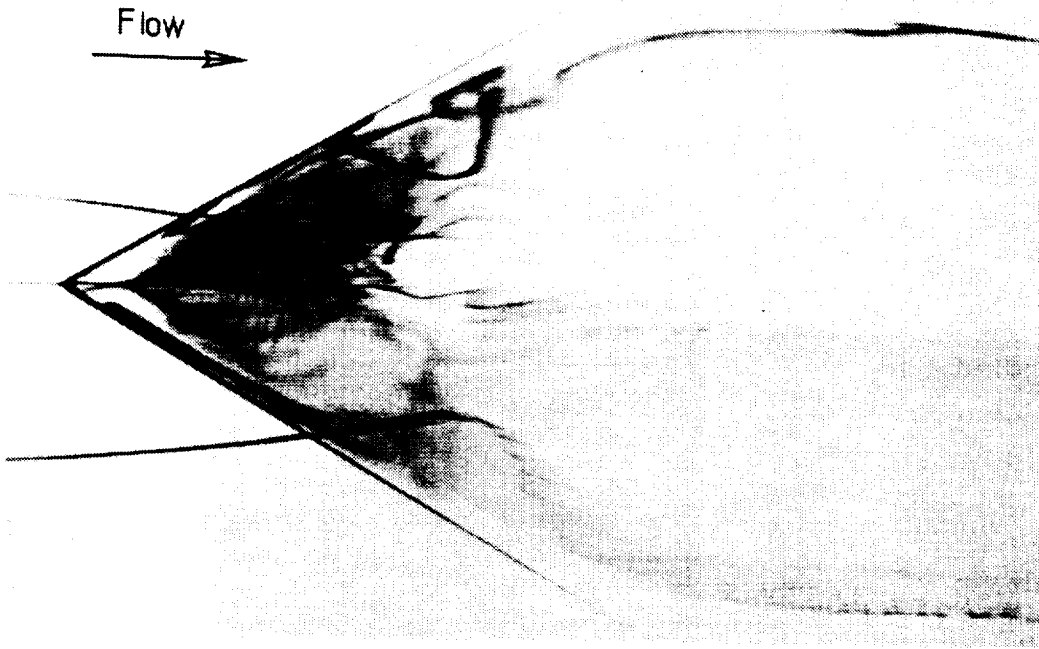


Figure B.10 Water Tunnel Flow Visualization Showing Cavity Interior and Vortex Core, Configuration 5 ( $\theta=30^\circ$ ,  $\delta=4^\circ$ )



Figure B.11 Water Tunnel Laser Sheet Showing Vortex Development 2 Inches Upstream of the Cavity Base, Configuration 6 ( $\theta=30^\circ$ ,  $\delta=8^\circ$ )



## APPENDIX C.      Sample input files for AXB

This appendix tabulates the input files used in the AXB grid generation program used to investigate vortex flow in a supersonic cavity.

SSVG.IN:

\*> main input file for "axmesh" package: patches= mb1, (i,j,k)

4

33 1 49    33 1 49    33 1 41    49 1 49

\*> file names: given edges coords; make-edge instructions:

ssvg.dat

ssvg.dsg

\*> key dimensions: kset (k, bdlr(k), yplus(k), thk(k), k=1, kset)

4

20 .01 0.0001

12 .005 0.00005

12 .10 0.00250

16 .005 0.00005

\*> g2mrdn normal control factor and smoothing cycle: fcto,ismg2

.60 36

\*> (k,i)-patch instructions: k,ityp,irul,ibvz:

1 1 1 0

2 1 1 0

3 1 1 0

4 1 1 0

\*> start of 3-dim grid and control file: scheme

time dependent

\*> zone/block indices

1

4

\*> make volume blocks: number of blocks and dimensions

4

33 73 49

33 121 49

33 49 41

49 121 49

\*> grid type flag: igr =1: axisymmetric; igr =2: rectangular

2

\*> fac 5,6 j-distr rules: kset,(k,nt,nb1,nb2,bg,end,s1,s2,ds1,ds2)

18

1	37	1	1	-2.0	0.0	0.04	0.01	0.04	0.01
2	37	1	1	0.0	2.0	0.01	0.04	0.01	0.04
3	37	1	20	-2.0	0.0	0.04	0.05	0.04	0.0005
4	37	20	1	0.0	2.0	0.05	0.04	0.0005	0.04
5	49	1	1	-0.002	0.002	0.	0.	0.	0.
6	37	1	20	-2.0	-0.577	0.04	0.02	0.04	0.0002
7	49	16	16	-0.577	0.577	0.04	0.04	0.0004	0.0004
8	37	20	1	0.577	2.0	0.02	0.04	0.0002	0.04
9	37	1	20	-2.0	-0.577	0.04	0.02	0.04	0.0002
10	49	12	12	-0.577	0.577	0.04	0.04	0.0005	0.0005
11	37	20	1	0.577	2.0	0.02	0.04	0.0005	0.04
12	49	1	1	-0.1	0.1	0.	0.	0.	0.
13	37	1	20	-2.0	-0.002	0.04	0.05	0.04	0.0005
14	37	20	1	0.002	2.0	0.05	0.04	0.0005	0.04
15	37	1	20	-2.0	-0.1	0.04	0.05	0.04	0.0005
16	37	20	1	0.1	2.0	0.05	0.04	0.0005	0.04
17	37	1	20	-2.0	0.0	0.04	0.10	0.04	0.005
18	37	20	1	0.0	2.0	0.10	0.04	0.005	0.04

\*> make volume blocks: face 1,2; four 5,6 edges; destination addr.

9

```
1 1 1 1 1 3 17 0 0 0 0 0 0 1 1 33 1 37 0 0
2 1 1 2 2 4 18 0 0 0 0 0 0 1 1 33 37 73 0 0
3 2 2 13 15 6 6 0 0 0 0 0 0 2 1 33 1 37 0 0
4 2 2 14 16 8 8 0 0 0 0 0 0 2 1 33 85 121 0 0
5 4 4 6 6 9 9 0 0 0 0 0 0 4 1 49 1 37 0 0
6 4 4 8 8 11 11 0 0 0 0 0 0 4 1 49 85 121 0 0
7 3 3 5 5 7 7 0 0 0 0 0 0 3 1 33 0 0 0 0
8 2 2 5 12 7 7 0 0 0 0 0 0 2 1 33 37 85 0 0
9 4 4 7 7 10 10 0 0 0 0 0 0 4 1 49 37 85 0 0
```

\*> boundary conditions for all blocks (ijswap status: 5,6,1,2,3,4)

4

```
-1 2 -1 -1 0 -1
1 4 -1 -1 0 -1
0 -6 0 0 0 2
2 -6 -1 -1 0 -1
```

## SSVG.DSG

\*> box specifications for Supersonic Vortex Generator (8 deg)

\*> control points: nctrlp =

10

\*> no.,type,rule,tag1,cntmp(1),cntmp(2),cntmp(3):

1	0	0	0	0.0	0.0	-0.25
2	0	0	0	0.0	0.5	-0.25
3	0	0	0	0.0	-0.14	0.0
4	0	0	0	0.0	0.0	0.0
5	0	0	0	0.0	0.602	0.0
6	0	0	0	0.0	-1.e-4	1.0
7	0	0	0	0.0	0.0	1.0
8	0	0	0	0.0	1.010	1.0
9	0	0	0	0.0	0.0	2.16
10	0	0	0	0.0	1.3815	2.16

\*> edge specifications for each box: number of boxes

4

\*> inflow [1]

1 1 1 1

\*> segment specifications: nc1,nc2,type,tag,rule(4),dstrb(4)

1	2	2	-7	0	0	-1	1	0.0	-1.2	0.0	0.0
4	5	2	-7	0	0	-1	1	0.0	-1.2	0.0	0.0
1	4	2	-7	0	0	1	-3	-2.0	0.0	0.0	0.0
2	5	2	-7	0	0	1	-3	-2.0	0.0	0.0	0.0

\*> wedge side [2]

1 1 1 1

```

*> segment specifications: nc1,nc2,type,tag,rule(4),dstrb(4)
  4  5  -1 -7   0  0 -1  1   0.0 -1.2  0.0  0.0
  7  8   2 -7   0  0 -1  1   0.0 -1.2  0.0  0.0
  4  7   2 -7   0  0  1  1  -0.8 -1.05  0.0  0.0
  5  8   2 -7   0  0  1  1  -0.8 -1.05  0.0  0.0
*> depression [3]
  1  1  1  1
*> segment specifications: nc1,nc2,type,tag,rule(4),dstrb(4)
  3  4   2 -7   0  0 -4 -2   0.0  0.0  0.0  0.0
  6  7   2 -7   0  0  1  1   0.0  0.0  0.0  0.0
  3  6   2 -7   0  0  1  1  -0.8 -1.05  0.0  0.0
  4  7  -1 -7   0  0  1  1  -0.8 -1.05  0.0  0.0
*> downstream [4]
  1  1  1  1
*> segment specifications: nc1,nc2,type,tag,rule(4),dstrb(4)
  7  8  -1 -7   0  0 -1  1   0.0 -1.2  0.0  0.0
  9 10   2 -7   0  0 -1  1   0.0 -1.2  0.0  0.0
  7  9   2 -7   0  0 -3  1   0.0 -2.0  0.0  0.0
  8 10   2 -7   0  0 -3  1   0.0 -2.0  0.0  0.0

```

SSVG.DAT

\*> given centerline, nozzle interior, nozzle exterior

0



**APPENDIX D.      Sample control files for PAB3D.V12**

This appendix tabulates the input and control files used by the PAB3D.V12 flow solver program used to simulate vortex flow in a supersonic cavity.

SURF.CONT

icut	iface	iprt	ib	izn	u	v	w	Pres.	Temp.
1	3	1	10	1	0.0	0.0	0.0	10.	294.4

## KE.CONT

ipt	ib	izn	ilhg	iord	rku	vmax	dtf	itk	icomp	comp	kelimt	ikn
1	2	1	-4	1	.01	200000.	2.	1	5	1. 1.e-4	10.	0 0
1	2	1	-4	1	.01	200000.	2.	1	5	1. 1.e-4	10.	0 0
1	3	1	-4	1	.01	200000.	2.	1	5	1. 1.e-4	10.	0 0
1	4	1	-4	1	.01	200000.	2.	1	5	1. 1.e-4	10.	0 0

SSVG8.CONT

--grid file name-- < time dep new Axb version>  
fgrid.dat  
--restart file name--  
restart.d  
--init file name--  
init8.d                    perf.cont                    ke.cont  
nte  
0 0  
nzone                                    Total number of volume grid = 670516  
1            4    2  
ngit  
10  
nit  
10\*10  
nitz        \*\*\*\*\* zone 1 \*\*\*\*\*  
1 1 1 1 1 1 1 1 1 1 1 1 1 1  
idim iblock (jdm,kdm), ... ... idm(m) ...  
49 4 73 49 121 49 49 41 121 49 33 33 33 49  
nitb        ..... block 1.1 .....        block count= 1  
10\*1  
nseq  
10\*444  
ibs    ibf  
1 32 1 32 1 32 1 32 1 32 1 32 1 32 1 32 1 32 1 32  
ivfluxj ivfluxr irstrt ivisc    iorth  
1 3 2 3 0  
I-SC LIMIT    J-SC LIMIT    K-SC LIMIT    IBIAS  
3 2 3 2 3 2 0

D4

```

Ncutpz(1,5) Ncutpz(1,6)
      1      1
ibci  j1  j2  k1  k2      (faces 5,6)
-1    1  72   1  48
10025  1  72   1  48
Npart(1) kturb(1,1) kturb(1,2) ... ipt(1,1) ... igrd ike
      2  -1  6  1  9  1  0

```

```

Ncutpb(1) Ncutpb(2) Ncutpb(3) Ncutpb(4)
      1      1      1      1
ibcjk  from  to   i1   i2      (faces 1,2,3,4)
      0    1   48    1   32
     -6    1   48    1   32
      0    1   72    1   32
     -17   1   72    1   32

```

```

nitb      ..... block 1.2 .....      block count= 2
1 1 1 1 1 1 1 1 1 1 1 1 1 1 1

```

```

nseq
10*444
ibs  ibf
1 32 1 32 1 32 1 32 1 32 1 32 1 32 1 32 1 32 1 32 1 32

```

```

ivfluxj ivfluxr irstrt ivisc  iorth
1 3 2 3 0

```

```

I-SC LIMIT  J-SC LIMIT  K-SC LIMIT  IBIAS
3 2 3 2 3 2 0

```

```

Ncutpz(1,5) Ncutpz(1,6)
      1      1
ibci  j1  j2  k1  k2      (faces 5,6)
10016  1  120   1  48
      4    1  120   1  48

```

Npart(1) kturb(1,1) kturb(1,2) ... ipt(1,1) ... igrd ike

1 6 1 1 0

Ncutpb(1) Ncutpb(2) Ncutpb(3) Ncutpb(4)

1 1 3 1

ibcjk from to il i2 (faces 1,2,3,4)

-6 1 48 1 32

0 1 48 1 32

0 1 36 1 32

3 37 84 1 32

0 85 120 1 32

-17 1 120 1 32

nitb ..... block 1.3 ..... block count= 3

1 1 1 1 1 1 1 1 1 1 1 1 1 1

nseq

10\*444

ibs ibf

1 32 1 32 1 32 1 32 1 32 1 32 1 32 1 32 1 32 1 32

ivfluxj ivfluxr irstrt ivisc iorth

1 3 2 3 0

I-SC LIMIT J-SC LIMIT K-SC LIMIT IBIAS

3 2 3 2 3 2 0

Ncutpz(1,5) Ncutpz(1,6)

1 1

ibci j1 j2 k1 k2 (faces 5,6)

0 1 48 1 40

-6 1 48 1 40

Npart(1) kturb(1,1) kturb(1,2) ... ipt(1,1) ... igrd ike

1 6 1 1 0

Ncutpb(1) Ncutpb(2) Ncutpb(3) Ncutpb(4)

1 1 1 1

D6

```

ibcjk  from  to  i1  i2      (faces 1,2,3,4)
  0    1   40   1   32
  0    1   40   1   32
  0    1   48   1   32
  2    1   48   1   32

```

```

nitb      ..... block 1.4 .....      block count= 4

```

```

1 1 1 1 1 1 1 1 1 1 1 1 1 1

```

```

nseq

```

```

10*444

```

```

ibs  ibf

```

```

1 48 1 48 1 48 1 48 1 48 1 48 1 48 1 48 1 48 1 48

```

```

ivfluxj ivfluxr irstrt ivisc  iorth

```

```

1 3 2 3 0

```

```

I-SC LIMIT  J-SC LIMIT  K-SC LIMIT  IBIAS

```

```

3 2 3 2 3 2 0

```

```

Ncutpz(1,5) Ncutpz(1,6)

```

```

1      1

```

```

ibci  j1  j2  k1  k2      (faces 5,6)

```

```

2    1  120    1  48

```

```

-6    1  120    1  48

```

```

Npart(1) kturb(1,1) kturb(1,2) ... ipt(1,1) ...  igrid ike

```

```

1  6  1  1  0

```

```

Ncutpb(1) Ncutpb(2) Ncutpb(3) Ncutpb(4)

```

```

1      1      1      1

```

```

ibcjk  from  to  i1  i2      (faces 1,2,3,4)

```

```

0    1   48   1   48

```

```

0    1   48   1   48

```

```

0    1  120   1   48

```

```

-17   1  120   1   48

```

3-D SUPERSONIC UNDEREXPANDED JET FLOW

RJ DT NIT NITFO IFLAGTS FMAX NITGBL ISYM  
0.0254 -0.5 1 0 -4 10.0 1 1

IGRID IRISIO INORM KG1 KG2 KG3 IPERF1 ISWEEP IMPVIS  
4 -1 0 1 5 2 0 0 1

IPMF0 IPMAX IRSTRT ISTEP NISTP IVAR IBC I2D ITRP  
1 80 2 51 1 2 0 0 0

ITURB ISEL ICOMP IVORT ISTAT SIGL SIGU Gamma Ireg Regt  
80 1 1 3 0 0.1 4.0 1.4 0 1

nprfile

0

INITIAL.DAT  
(Initial Conditions file)

iunit nblock iswp

0 4 0

ncut jstart

1

1,73,1,49,1

1

1,121,1,49,1

1

1,49,1,41,1

1

1,121,1,49,1

nset iinit

1 1

pr temp mach alpha Beta gam iin

129.36 580.00 1.0 0. 0. 1.4 0

# REPORT DOCUMENTATION PAGE

*Form Approved*  
*OMB No. 0704-0188*

Public reporting burden for this collection of information is estimated to average 1 hour per response, including the time for reviewing instructions, searching existing data sources, gathering and maintaining the data needed, and completing and reviewing the collection of information. Send comments regarding this burden estimate or any other aspect of this collection of information, including suggestions for reducing this burden, to Washington Headquarters Services, Directorate for Information Operations and Reports, 1215 Jefferson Davis Highway, Suite 1204, Arlington, VA 22202-4302, and to the Office of Management and Budget, Paperwork Reduction Project (0704-0188), Washington, DC 20503.

<b>1. AGENCY USE ONLY (Leave blank)</b>		<b>2. REPORT DATE</b> February 1996	<b>3. REPORT TYPE AND DATES COVERED</b> Contractor Report	
<b>4. TITLE AND SUBTITLE</b> An Investigation of Cavity Vortex Generators in Supersonic Flow			<b>5. FUNDING NUMBERS</b> NCC1-172 WU 307-50-14-03	
<b>6. AUTHOR(S)</b> Richard Hazlewood				
<b>7. PERFORMING ORGANIZATION NAME(S) AND ADDRESS(ES)</b> University of Kansas Center for Research, Inc. 2291 Irving Hill Drive-Campus West Lawrence, KS 66045			<b>8. PERFORMING ORGANIZATION REPORT NUMBER</b>	
<b>9. SPONSORING / MONITORING AGENCY NAME(S) AND ADDRESS(ES)</b> National Aeronautics and Space Administration Langley Research Center Hampton, VA 23681-0001			<b>10. SPONSORING / MONITORING AGENCY REPORT NUMBER</b> NASA CR-198202	
<b>11. SUPPLEMENTARY NOTES</b> Langley Technical Monitor: Daniel L. Cler				
<b>12a. DISTRIBUTION / AVAILABILITY STATEMENT</b> Unclassified-Unlimited Subject Category 02			<b>12b. DISTRIBUTION CODE</b>	
<b>13. ABSTRACT (Maximum 200 words)</b> The purpose of this report is to document the results of experiments performed at the University of Kansas and at the NASA Langley Research Center (LaRC) into the use of shaped cavities to generate vortices in supersonic flow, as well as the progress made in simulating the observed flow using the PAB3D flow solver. The investigation was performed on 18 different cavity configurations installed in a convergent-divergent nozzle at the Jet Exit Facility at the LaRC. Pressure sensitive paint, static-pressure ports, focusing Schliern, and water tunnel flow visualization techniques were used to study the nature of the flow created by these cavities. The results of these investigations revealed that a shaped cavity can generate a pair of counter-rotating streamwise vortices in supersonic flow by creating weak, compression Mach waves and weak shocks. The PAB3D computer program, developed at the LaRC, was used to attempt to reproduce the experimental results. Unfortunately, due to problems with matching the grid blocks, no converged results were obtained. However, intermediate results, as well as a complete definition of the grid matching problems and suggested courses of actions are presented.				
<b>14. SUBJECT TERMS</b> Plug nozzle, spherical-convergent-flap, internal nozzle performance, thrust vectoring, multifunction nozzle, yaw vectoring, gimbaled nozzle, convertible plug, and clamshell plug			<b>15. NUMBER OF PAGES</b> 127	
			<b>16. PRICE CODE</b> A07	
<b>17. SECURITY CLASSIFICATION OF REPORT</b> Unclassified	<b>18. SECURITY CLASSIFICATION OF THIS PAGE</b> Unclassified	<b>19. SECURITY CLASSIFICATION OF ABSTRACT</b> Unclassified	<b>20. LIMITATION OF ABSTRACT</b> Unlimited	



